The Thesis Committee for Priya Ravi Ganesh
Certifies that this is the approved version of the following thesis:

Geologic drivers affecting buoyant plume migration patterns in small-scale heterogeneous media: Characterizing capillary channels of sequestered CO_2

APPROVED BY
SUPERVISING COMMITTEE:

Supervisor:

Steven L Bryant

Co-supervisor:

Timothy A Meckel

Geologic drivers affecting buoyant plume migration patterns in small-scale heterogeneous media: Characterizing capillary channels of sequestered CO_2

by

Priya Ravi Ganesh, B.E

Thesis

Presented to the Faculty of the Graduate School of

The University of Texas at Austin

in Partial Fulfillment

of the Requirements

for the Degree of

Master of Science in Engineering

The University of Texas at Austin

December 2012

Acknowledgements

I would like to take this opportunity to thank my advisors Dr. Steve Bryant and Dr. Tip Meckel at UT Austin. Their support, advice and patience has been invaluable on both an academic and a personal level, for which I am extremely grateful. Our stimulating discussions to figure out 'what is going on' will be dearly missed. Very few people put in their heart and soul in their work and I consider it my privilege to have been associated with two such wonderful teachers albeit for a short period of time.

Funding contributing to this research was provided through the Department of Energy National Energy Technology Laboratory Project #DE-FE0001941. I am extremely thankful to everyone at the Gulf Coast Carbon Center at the Bureau of Economic Geology, the University of Texas at Austin for generously providing both facilities and support for the execution of this work. Peel topographic data were obtained with Tim Dooley of BEG's Applied Geodynamics Laboratory and the high-resolution 3D optical microscopy was obtained with BEG's Dr. Greg Frebourg.

I am grateful to Joanna Castillo and Roger Terzian for their timely-IT related help and to Sophia Ortiz for helping me with administrative matters at the Department of Petroleum and Geosystems Engineering. I sincerely appreciate the support extended to me by all my colleagues at the Department of Petroleum and Geosystems Engineering and the Bureau of Economic Geology.

I would like to express my heartfelt gratitude to my parents and brother, and to all my friends for their unconditional love and unwavering support. This would not have been possible without all of you.

Abstract

Geologic drivers affecting buoyant plume migration patterns in small-scale heterogeneous media: Characterizing capillary channels of sequestered CO_2

Priya Ravi Ganesh, M.S.E

The University of Texas at Austin, 2012

Supervisors: Timothy A Meckel and Steven L Bryant

CO_2 sequestration aims for the most efficient utilization of reservoir pore volume and for maximizing security of storage. For typical field conditions and injection rates, buoyancy and capillary forces grow dominant over viscous forces within hundreds of meters of the injection wells as the pressure gradient from injection becomes less influential on flow processes. Flow regimes ranging from compact flow to capillary channel flow or secondary accumulation beneath a seal are possible through time as the CO_2 plume travels through the storage reservoir. Here we model the range of possible migration behavior in the capillary channel regime in small-scale domains whose heterogeneity has been resolved at depositional (sub-millimeter) scale.

Two types of model domains have been studied in this work: domains with depositional fabric from real, naturally-occurring geologic samples and geostatistically generated synthetic model fabrics. The real domains come from quasi-2D physical geologic samples (peel # 1: ~1 m × 0.5 m sample and peel # 2: ~0.4 m × 0.6 m sample) that are vertically oriented relief peels of fluvial sediment extracted from the Brazos River, Texas.

Peel # 1 is oriented perpendicular to dominant depositional flow while peel # 2 is a flow-parallel specimen. The various depositional fabrics represent definite correlation lengths of threshold pressures in the horizontal and vertical directions which can be extracted. High-resolution (~2 million element model) laser scanning of the samples provided detailed topography which is the result of nearly linear corresponding changes in measured grain size (normal distribution) and sorting.

We model the basic physics of buoyant migration in heterogeneous domain using commercial software which applies the principle of invasion percolation (IP). The criterion for governing drainage at the pore scale is that the capillary pressure of the fluid needs to be greater than or equal to the threshold pressure of the pore throat it is trying to enter for the interface to advance into the pore. Here we employ the extension of this concept to flows at larger scales, which replaces the pore throat with a volume of rock with a characteristic value of capillary entry pressure. The fluid capillary pressure is proportional to the height of continuous column of the buoyant phase. The effects of (i) threshold pressure range, i.e. difference between the maximum and minimum threshold pressures in the domain; and (ii) the density difference between CO_2 and connate water on capillary channels of CO_2 were studied on the various sedimentologic fabrics.

As the rock and fluid properties varied for different model domains, CO_2 migration patterns varied between predominantly fingering and predominantly back-filling structures. Sufficiently heterogeneous media (threshold pressures varying by a factor of 10 or more) and media with depositional fabrics having high ratios of horizontal and vertical correlation lengths of capillary entry pressures in the domain yield back-filling pattern, resulting in a significantly large storage capacity. Invasion percolation simulation models give qualitatively similar CO_2 migration patterns compared to full-physics simulators in small-scale but high resolution domains which are sufficiently heterogeneous. On the other hand, we find the invasion percolation simulations predicting disperse capillary fingering pattern in relatively homogeneous media (threshold pressures varying by less than a factor of 10) while the full-physics

simulations reveal a very compact CO_2 front in the same media. This stark difference needs to be investigated to understand the governing flow physics in these domains. Fingering flow pattern in the capillary channel regime would clearly result in the estimated storage capacity being much less than the nominal value (the pore volume of the rock) as the rock-fluid contact is minimal.

The importance of this work lies in the verification that a relatively simple model (invasion percolation), which runs in a very small fraction of the time required by full-physics simulators, can be used to study buoyant migration in rocks at the micro-scale. Understanding migration behavior at the small-scale can help us approach the problem of upscaling better and hence define the complex plume dynamics at the reservoir scale more realistically. Knowledge of the correlation structure of the sedimentologic fabric (ratio of correlation lengths of threshold pressures in horizontal and vertical directions) and the threshold pressure distribution (permeability distribution) for any given reservoir rock could help evaluate amount of CO_2 that can be stored per unit volume of rock (storage potential) for a reservoir in the migration phase of sequestration. The possibility of predictive ability for expected capillary channel flow patterns kindles the prospect of enabling an engineered storage strategy that drives the behavior toward the desired flow patterns in the subsurface.

Contents

LIST OF TABLES:

LIST OF FIGURES:

1) INTRODUCTION

1.1 Background: The "Carbon problem"

Carbon emissions contribute to various pressing problems from global warming, climate change to ocean acidification. Scientists at the National Oceanic and Atmospheric Administration (NOAA) discovered during the spring of 2012 that we passed a critically unfortunate marker of climate change: atmospheric concentrations of CO_2 in the Arctic hit 400 parts per million (ppm). The rest of the world is expected to follow suit and reach this mark within a few years. The carbon problem can be stated relatively simply:

More than six billion people around the world burn organic fuel to power their day-to-day activities and our energy requirements are expected to only increase further. Carbon dioxide is a combustion product formed as a result of burning organic fuel. In 2010 we released about 33.5 gigatonnes of carbon dioxide from anthropogenic sources (G.P. Peters et al. Global carbon budget 2010 summary, Tyndall Centre for Climate Change Research). Carbon dioxide concentration in the atmosphere has seen a 35% increase over pre-industrial age values (Office of Science, US Department of Energy). Since carbon dioxide is a greenhouse gas, such a jump in its atmospheric concentration affects solar radiation balance contributing to 'global warming' and climate change.

1.1.1 CO_2 emissions and trends in the United States

CO_2 is already present in the atmosphere naturally due to the earth's carbon cycle. The carbon cycle describes the continuous exchange of carbon dioxide between the atmosphere, ocean, and land surfaces. The input and output of CO_2 by the natural processes comprising the carbon cycle tend to balance out causing no net accumulation of CO_2 in the biosphere. Since the Industrial Revolution, however, anthropogenic emissions are rapidly adding onto this amount and causing a severe imbalance by altering the carbon cycle. Figure 1-1 describes the earth's carbon cycle. The figures in red arrows

show the additional carbon flux due to human influence while the blue arrows give the natural carbon flux values.

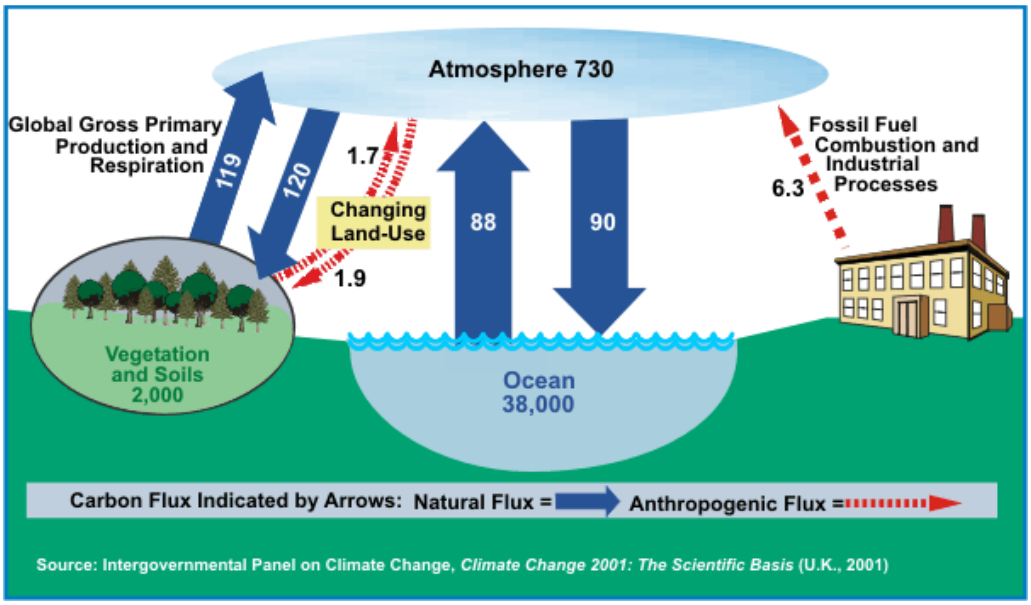

Figure 1-1: Carbon cycle describing the carbon flux (in billions of tons of carbon per year) as CO_2 is being exchanged between land, atmosphere and oceans. Carbon fluxes indicated by red arrows are human contributions while the blue arrows indicate natural flux values. (Figure from Intergovernmental panel on climate change (IPCC), Climate Change 2001: The Scientific Basis, U.K., 2001)

Human activities are the main cause of the substantial increase in atmospheric CO_2 concentrations. More than 90% of the CO_2 emissions are due to fossil-fuel combustion i.e. anthropogenic sources. CO_2 emissions vary around the globe depending on the population density and the extent of economic and industrial development in various countries. The population growth, economic growth, changing energy prices and new technologies all drive the amount of greenhouse gas emissions. With mushrooming population figures, our demand for energy is only expected to increase further. Figure 1-2 gives the global CO_2 emission trends in the last century.

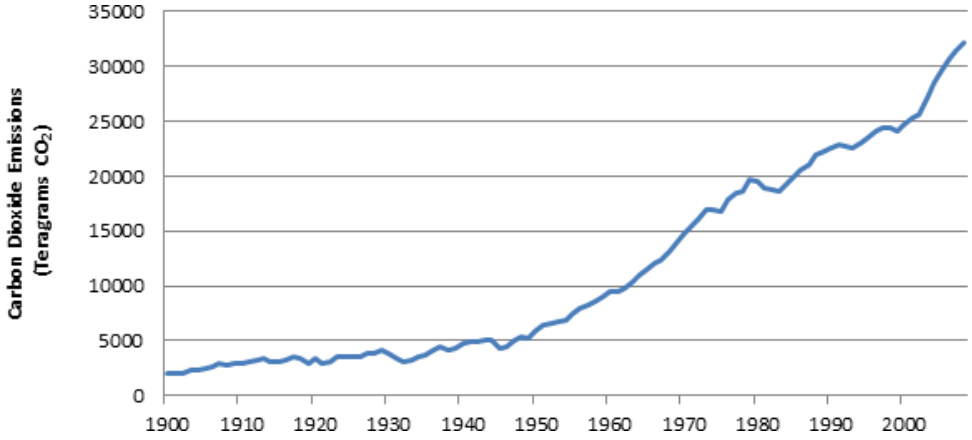

Figure 1-2: Global CO_2 annual emission trends in the last century (Boden *et al.*, 2010)

To put this emission data into context, scientific models show that CO_2 concentrations today are greater than at any time during the last 800,000 years (NOAA). The major countries responsible for greenhouse gas emissions due to anthropogenic activities are given in Figure 1-3.

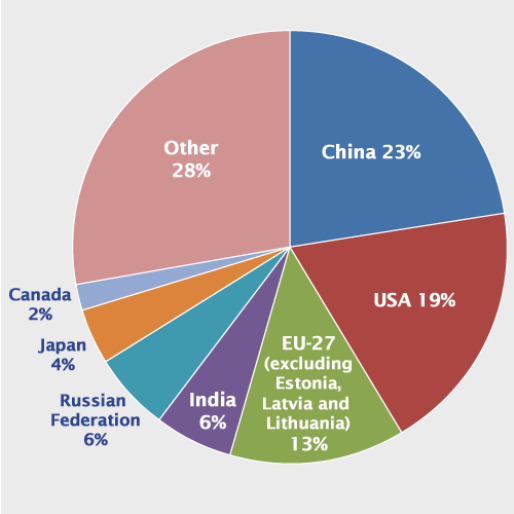

Figure 1-3: Emissions by country from fossil fuel combustion (Figure from National CO_2 emissions from fossil-fuel burning, cement manufacture, and gas flaring: 1751-2008)

The United States of America leads the developed world in CO_2 emissions. In 2010, EPA figures for greenhouse gas emissions in the United States totaled 6822 million tonnes of

CO_2 equivalent. It is helpful to identify the various anthropogenic sources of CO_2 to deal with the problem of emission regulation. The main sources of CO_2 emissions in the United States are given in Figure 1-4.

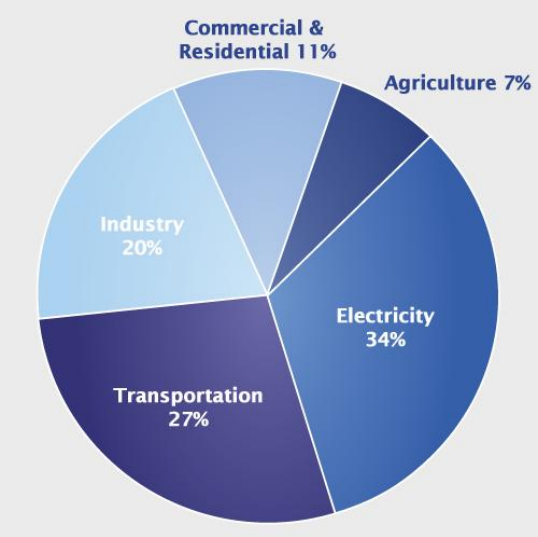

Figure 1-4: US CO_2 emissions by source in 2010. Total emissions in 2010 = 6822 million tonnes CO_2 equivalent. Electricity production is the dominant economic sector responsible for greenhouse gas emissions followed by transportation. (Figure from Inventory of U.S. Greenhouse Gases and Sinks, United States Environmental Protection Agency, EPA)

The two major sources of greenhouse gas emissions in the United States are electricity and transportation. Electricity generation accounts for roughly 1/3 of the total US CO_2 production. The United States emits about 1.9 billion tonnes of carbon dioxide annually from coal-fired power plants. 95% of the energy used to transport people and goods across the world comes from the burning of fossil fuels.

1.1.2 Carbon footprint and climate change

John Tyndall, in 1861, first attributed climatic temperature changes to variations in the amount of carbon dioxide in the atmosphere. Carbon dioxide and other greenhouse gases

control temperature by absorbing energy in the infrared region at various characteristic frequencies and trap heat. Greenhouse effect causes global warming by thus decreasing the amount of radiation that escapes back to space. The harmful effects of climate change are well-known and have been discussed for many years at various forums across the globe. The severity of the problem depends not only on the magnitude of change but the potential for reversibility. Though the oceans would ultimately take up all this CO_2, it is the much slower rate at which this would happen that is the cause for our concern. In less than 1000 years, if our consumption continues to increase at the current rate, we would have exhausted all known reserves of coal and oil. And by that time we would have added 18 times the present amount of CO_2 into the atmosphere. The earth's temperature is then expected to be 10.5 degrees above its present average after equilibrating with the oceans (Scientific American).

Carbon footprints endeavor to measure the emission data of greenhouse gases as they cause climate change. The main influences on carbon footprints are the population, economic output and energy intensity of the economy. Mitigating carbon footprints by decreasing the dependence on fossil fuels or by decreasing the energy consumption itself is done by 'carbon offsetting'. The Kyoto Protocol, for instance, defines legally binding emission regulation targets through this process for countries that ratified the protocol.

1.1.3 Solving the carbon problem

Energy consumption patterns are not uniform throughout the world and there are still countries that are energy impoverished. Solutions for the carbon problem tackle different aspects of the carbon problem and aim at different scales of impact. We need to radically change the energy systems that have shaped our lives for over a hundred years. There are three possible options, none being "the solution" by itself, to deal with the clean energy crisis we are facing:

a) Focus on energy efficiency and energy conservation

We need to invest in energy efficient technologies. Starting from our homes, our focus must be on responsible and judicious utilization of energy. We need to adopt energy-consumption practices that are globally sustainable.

b) Fuel switching:

   i. Switch from coal to gas

      We must focus on reducing emissions from the use of coal (the dirtiest energy source) and switch to more efficient and cleaner natural gas to generate power. To head towards a clean energy economy, we need definite and enforceable emission targets.

   ii. Switch from fossil fuels to sustainable green energy

      Renewables like biofuels, solar, wind and hydro power are the options in a nuclear-free clean energy future. Germany, for example, plans to derive 35% of its power supply from renewable energy sources by 2020 and 80% by 2050. The challenges presented by renewables are dependability and scale-up technologies which will take years of research before full-scale implementation.

c) CCUS (Carbon Capture Utilization and Storage)

   CCUS is the only viable solution that tackles the scale of the carbon problem currently. Successful research in this area would help overcome the technical and economic challenges of cost-effective technologies for capture, transportation and injection into underground structures, safe storage and monitoring.

1.2 CCUS: A possible large-scale mitigation strategy

Storage of CO_2 is envisaged mainly in deep geologic formations as deep ocean storage has raised concerns of ocean acidification. The National Energy Technology Laboratory (NETL) has reported that the storage capacity in North America is sufficient to handle more than 900 years of current carbon dioxide production rates. Carbon Capture and Storage refers to the technology to prevent anthropogenic CO_2 release into the atmosphere and securely storing this CO_2 underground. The concept of CCS involves the

following three stages: capture, transportation and sequestration into geologic structures. The utilization aspect involves using this CO_2 for enhanced oil recovery operations. We focus on the CCS aspect here without delving into the utilization of CO_2 for enhanced oil recovery operations.

Capture of CO_2: This phase consists of capturing CO_2 from the various sources and processing to achieve injection specifications. Carbon dioxide capture focuses on efficient technologies that capture CO_2 from emissions of major single point sources like power plants. CO_2 can be separated and collected from the waste gas stream in traditional power plants or pre-combustion capture technologies in IGCC (integrated gasification combined cycle) power plants ensures pure CO_2 emission stream for direct capture. Almost 80-90% of the total cost involved in CCS is associated with the capture stage.

Transport of CO_2: Since all CO_2 sources are not close to injection/ storage sites, transportation through pipelines is an essential aspect of any CCS project.

Geological sequestration of CO_2: Almost all sequestration considers strategies to inject CO_2 deep into the earth so that temperature and pressure in the subsurface exceed the critical point of CO_2. Supercritical CO_2 is denser than gaseous CO_2 and hence the storage space is used more efficiently. The CO_2 stream is injected into the underground geologic structure in the injection phase and this CO_2 migrates through the reservoir.

A brief summary of some large-scale integrated CCS projects currently in operation as of mid 2011 are given below.

In Salah gas field in Algeria: In Salah, an industrial-scale CCS project in Algeria has been operating since 2004 with more than 3 million tonnes of CO_2 injected in a deep saline formation. CO_2 from natural gas production is captured and stored by project operators BP, Sonatrach and Statoil. This project is supported by the US Department of Energy and the European Union.

Sleipner CO_2 Injection in Norway: Sleipner is a fully operational offshore gas field with CO_2 injection. CO_2 is separated from produced gas and reinjected into the Utsira sand, a saline aquifer above the hydrocarbon reservoir zones. Statoil is injecting approximately one million tons per year of recovered CO_2 into this formation. Around 11.4 million tons of CO_2 have been injected into the reservoir unit at 800-1100 m depth.

Snøhvit CO_2 Injection in Norway: Snøhvit is a fully operational offshore gas field with CO_2 injection. The LNG plant is located onshore. CO_2 is separated from produced gas and injected in a saline aquifer below the H/C reservoir zones offshore. This liquefied natural gas (LNG) plant captures 0.7 Mt/a of CO_2 and injects it into the Tubåen sandstone formation 2,600 m under the seabed for storage.

Extensive research has been taking place regarding optimal storage conditions for CO_2 in the subsurface. We focus on relevant buoyant fluid flow dynamics to shed light on some aspects determining storage capacity of the rock.

1.3 The subsurface challenge: Research motivation

The subsurface system is very complex with various simultaneous geochemical reactions, geomechanics, multiphase fluid flow and energy transport taking place. The underlying physics of fluid flow must be rightly considered to investigate the subsurface system with as much accuracy and detail as possible at the scale of the problem. There are essentially three sets of forces acting on the fluids system: gravity, capillary and viscous forces. Once CO_2 is injected into the formation, the buoyant fluid redistributes itself in the pore spaces of the rock. Viscous forces grow negligible while gravity (buoyancy) and capillary forces start dominating over time into the reservoir. Buoyancy-driven flow regime thus dominates flow through most part of the sequestration process. The relevance of this flow regime is applicable in the following stages of sequestration.

1.3.1 During CO_2 injection phase

For CO_2-H_2O system, the buoyancy forces are given by $\Delta\rho g$ = 0.13 psi/ft (2.94 kPa/m) for a density difference of 300 kg/m^3 between CO_2 and native brine. If the pressure gradient is much higher than the buoyancy forces then fluid flow occurs in the viscous flow regime. Buoyancy-driven flow regime kicks in once the pressure gradient drops to values comparable to the buoyancy gradient.

For radial injection wells, pressure profiles can be analytically determined. As an example scenario, we present a set of analytical pressure profile calculations performed in Oruganti (2010). Consider an infinite reservoir 50 ft (15.24 m) thick and 10000 ft (3048 m) deep, with radial injection of CO_2 at the rate of 10000 Rbbl/day (1145 metric tons per day). The permeability of this 50ft (15.24 m) thick section is 100 mD. Figure 1-5 gives the model parameters and the overpressure profile for this scenario.

(a)

Aquifer Boundary Condition	Constant Pressure Boundary
Constant rate of injection (q_{in})	10,000 Rbbl/day = 1145 metric tons/day for ρ_{CO2}=45 lbm/ft^3
Relative permeability curve	Viking sandstone (Bennion and Bachu, 2005)
Aquifer thickness (h)	50 ft
Storage aquifer permeability (k)	100 mD
Bounding aquifer permeability (k_{aq})	10^7 mD
Brine compressibility in bounding aquifer (c_w)	4×10^{-6} psi^{-1}
Rock compressibility of bounding aquifer (c_r)	3×10^{-6} psi^{-1}
Porosity (φ)	0.25
Depth of aquifer	10,000 ft
Wellbore radius (r_w)	0.5 ft
Storage aquifer drainage radius (r_e)	33,056 ft

(b)

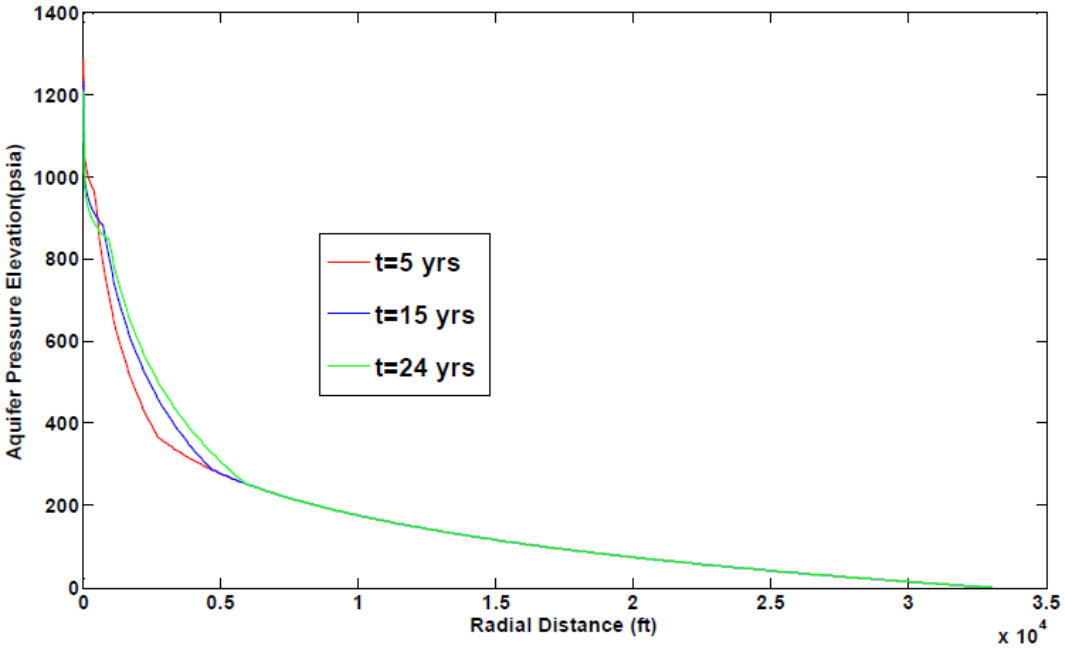

Figure 1-5: Overpressure profile for radial injection well in an infinite reservoir (from Oruganti, 2011). The radial distance gives the distance in the reservoir from the vertical

injection well. The aquifer pressure elevation is calculated as the pressure elevation in the aquifer above hydrostatic pressure. Panel (a) gives the analytical model parameters for a storage aquifer case. Panel (b) shows the pressure buildup profile in the storage aquifer as a function of time for this case.

A subsequent analysis is performed with this data to study transition of flow regimes for reservoirs with different thicknesses and permeabilities. The storage scenario from the previous example with the storage aquifer permeability as 100 mD while its thickness is varied as 50 ft and 100 ft. Constant injection rate of 10000 Rbbl/day is maintained for both cases. For these cases the bottomhole pressure in the injection well exceeds the initial pore pressure by 1000 psi to 2500 psi, a range safely below the fracture initiation pressure. The pressure gradient with radial distance into the reservoir is calculated and plotted (Figure 1-6) for these different storage aquifer permeability and thickness values.

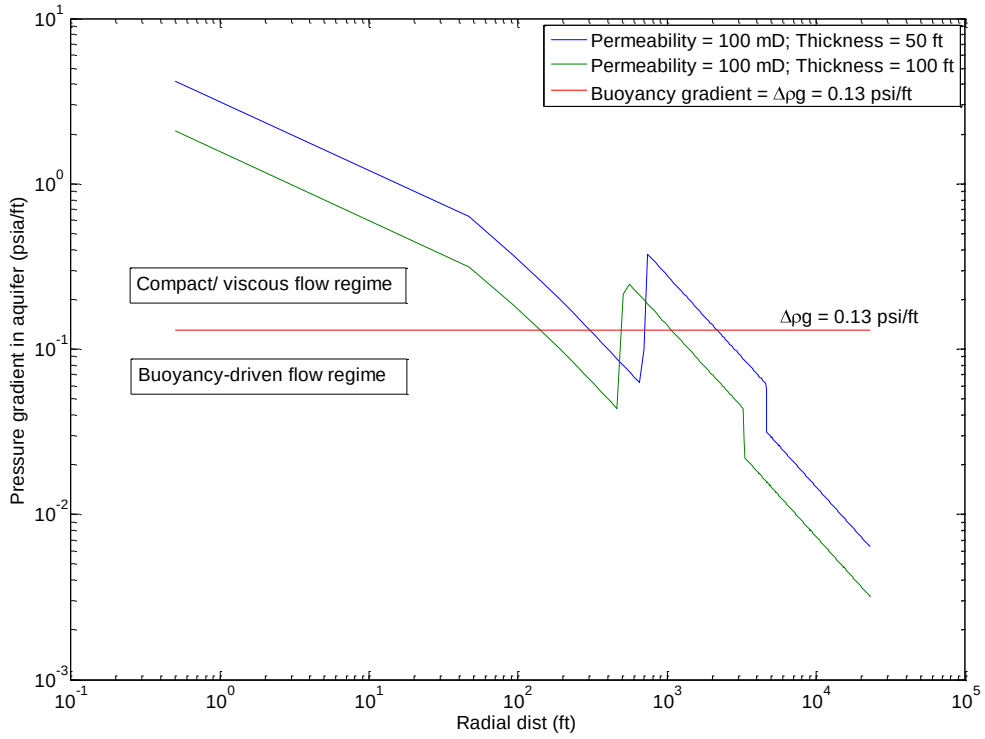

Figure 1-6: Pressure gradient profile for radial injection well in an infinite reservoir (from Oruganti, 2011). The radial distance gives the distance in the reservoir from the vertical

injection well. The pressure gradients are assessed (t = 15 years) for different storage aquifer thicknesses and constant CO_2 injection rate case. The 'kink' at 700 to 1000 ft is the transition from the dry region (only CO_2 present) to the two-phase flow region.

The pressure gradient drops below the buoyancy gradient (0.13 psi/ft) within 700 feet (213 m) as seen for the 100 mD reservoir cases in Figure 1-6. Buoyancy forces are seen to dominate flow regime over most part of the reservoir here. For the less thick formation we see that buoyancy forces take over farther into the reservoir for the same injection flow rate compared to the higher permeability rocks.

Recent research (Jain, 2011; Szulczewski and Juanes, 2012) proposes a line-drive array of CO_2 injection wells in the reservoir. Many CO_2 EOR project designs also utilize this injection configuration. The overpressure that can be maintained in a field has fracture pressure limitations. The buoyancy forces would matter only if their values are comparable to the pressure gradient. For buoyancy forces of $\Delta\rho g$ = 0.13 psi/ft, this would mean, say for the 10000 ft (3048 m) long reservoir in the above example, we would need to maintain an overpressure of at least 1300 psi (8963 kPa) for viscous forces to dominate the system. This could be unrealistic considering the fracture conditions of typical reservoirs.

1.3.2 Post CO_2 injection phase

The post-injection phase involves the redistribution of CO_2 in the reservoir. Once injection stops, the pressure gradient drops drastically and buoyancy forces dominate in the post-injection phase as the reservoir experiences a zero external pressure gradient. This point of transition to the buoyancy-driven flow regime now occurs much closer to the injection point than during the injection phase.

If buoyancy and capillary forces are comparable, then the migration of a CO_2 plume will be heavily dependent upon the capillary properties of the storage formation. Capillary

barriers confine CO_2 to specific flow paths in some regions even though the absolute permeability would allow significant flow. Immobilized, considerable above-residual saturations of CO_2 are identified in 'local capillary traps' discussed in Saadatpoor (2009). Recognizing the significance of geological influences on the migration patterns, it is clear that it is important to resolve the porous medium at depositional scale in our simulation models. This work utilizes a new technique to generate well-quantified digital representations of real geologic media. These high resolution digital representations of real porous media bring out interesting physics that control the amount of pore space contacted by the CO_2 and invasion patterns once buoyancy forces take over the massive bulk of buoyant sequestered CO_2. We endeavor to understand the migration behavior of sequestered CO_2 in small-scale (meter scale) porous media and understand the driving forces influencing flow patterns at this scale. We attempt to explore the following issues in this work:

1. What are the primary geologic controls affecting fluid accumulation size?

2. What does the geologic system (petrophysical and depositional properties of the medium) reveal about the long-term fluid migration characteristics?

3. How does the capillary channel flow regime influence effective rock-fluid contact and thus affect storage capacity?

4. How does small-scale migration behavior tie with reservoir-scale plume dynamics?

1.4 Review of chapters

Chapter 2 gives a literature review of the work done related to capillary heterogeneity trapping in heterogeneous formations and aspects related to this work. Chapter 3 defines the concepts and geologic setting applicable to this work. Chapter 4 introduces the simulators used in this work and the development techniques for the models we investigate in this study. We perform sensitivity analyses on 2D domains and proceed to

corroborate our observations on real geologic domains. We also tie the results from the invasion percolation models to the full physics simulators and validate their relevance. Chapter 5 discusses these results. Chapter 6 gives a glimpse of the comparison between full physics simulators and invasion percolation simulation models in 3D. Chapters 7 and 8 are the summary of our work with recommendations for future work.

2) LITERATURE SURVEY

2.1 Geological storage of CO_2

Under typical CO_2 storage conditions at the end of the injection phase, the injected CO_2 will continue to migrate upwards driven only by buoyancy and it will leave behind a residual phase trapped by capillary forces. Bryant *et al.* (2008) investigate CO_2 storage in deep saline aquifers using the strategy of the 'inject low and let rise' (Kumar *et al.*, 2005; Ozah *et al.*, 2005) to reduce the amount of potentially mobile CO_2 and correspondingly reduce the risk of leakage over the long term. Their simulation results suggest that the first order influence on buoyancy-driven CO_2 displacement is heterogeneity, not the instability of the interface. They conclude that accounting for capillarity in the aquifer models is important to assess the vertical distance that CO_2 could travel in that storage aquifer. The threshold pressure distribution is the governing parameter affecting buoyant fluid migration according to Carruthers (1998).

CO_2 can be stored/ trapped in an aquifer in four modes: as a bulk phase within a structural trap (above residual saturation), as a residual phase trapped by capillary forces, by dissolution in brine, and mineral precipitation. CO_2 held in a structural trap at large saturations will remain trapped only as long as the seal remains intact while the other three forms of storage are more permanent in nature. Luo *et al.* (2004) and Zhang *et al.* (2003) have demonstrated by physical experiments how mobile hydrocarbon continues to migrate in a porous medium even after the source is cut off but the migration pathways that have been formed start shrinking and residual hydrocarbon saturations vary depending on the pathway morphology. Ozah *et al.* (2005) conclude that the phenomenon of capillary trapping is by far the most significant mechanism for permanent storage. Their simulations report that the amount of CO_2 sequestered as minerals is small relative to gas trapping and dissolution in brine. Saadatpoor *et al.* (2009) report significant immobilization of CO_2 as a trapped phase beneath capillary barriers in brine-saturated rock at saturations much larger than would be possible as isolated ganglia. Ozah *et al.* (2005) suggest scaling the capillary pressure for each individual grid block to have a

more physically accurate model and results. Kumar (2004), Ozah (2005) and Saadatpoor (2009) all show extensive results of CO_2 migration incorporating this variability in capillary heterogeneity in their simulation models. Saadatpoor *et al.* (2009) show how spatially varying capillary entry pressures can cause qualitatively different plume behavior. Heterogeneity intrinsic to sedimentary rocks gives rise to a category of trapping that Saadatpoor (2010) defines as local capillary trapping. Local capillary trapping differs from residual trapping in that the accumulated buoyant fluid saturation could be much larger than the residual saturation for that rock. Krevor *et al.* (2011) experimentally demonstrated the phenomenon of capillary heterogeneity trapping of CO_2 in Mt Simon sandstone core samples at reservoir conditions.

England *et al.* (1987) explain that all fluid movement in the subsurface is due to the presence of fluid potential gradients. They elucidate that "Petroleum will only migrate as far (and as fast) as the volume of petroleum expelled from the source rock can spread out whilst remaining fully interconnected." By choosing the volume injected, one can, in principle, prevent the rising CO_2 (buoyant invading fluid phase) from reaching the top of the aquifer. The vertical distance that CO_2 rises depends on the uniformity of the displacement front and the CO_2 saturation behind the front. The intention of sequestration is to fully utilize the available pore space of the rock and store as much CO_2 as possible.

The dynamics of capillary channel flow cannot be captured by standard continuum simulators with large (meter scale) grid elements to which a single “average” capillary pressure curve and set of relative permeability curves must be assigned. CO_2 observed to migrate vertically through shaly horizons in the Utsira formation is an interesting case of flow through what are usually considered to be barriers (Hermanrud *et al.*, 2010). In Utsira, CO_2 accumulations are found to grow laterally beneath each shale layer and also penetrate vertically through them which cannot be predicted by conventional simulation models. Modeling the dominant flow physics at the appropriate scale is thus important to get valid estimates of fluid migration through formations and effective storage capacity. Buoyancy-driven flow has been studied using pore network models, invasion percolation

models and micromodel experiments. Invasion percolation models are found sufficient to model the flow structure obtained under slow drainage conditions (negligible viscous forces).

2.2 Invasion percolation models for buoyancy-driven flow

In their well-known paper, England *et al.* (1987) extensively studied secondary oil migration and made a number of substantial conclusions. Secondary oil migration is the movement of hydrocarbons from the source bed through the more coarse-grained and permeable carrier beds. These hydrocarbons would migrate until they are trapped below a flow barrier to form an accumulation or seep through the surface of the earth. England et al. (1987) state that "Experiments with oil-water mixtures in rocks have shown that at capillary numbers greater than 10^{-4}, viscous forces become important. However, at geological flow rates the capillary number is never greater than 10^{-10}; capillary forces therefore dominate at all times." Wilkinson and Willemsen (1983) coined the phrase 'invasion percolation'. It applies to the problem of fluid-fluid immiscible displacement in a porous medium under the action of capillary forces with the dynamic rule of "advancing the interface at the point of least resistance as opposed to advancing all interfaces up to some chosen threshold resistance".

IP (Invasion Percolation) has been shown to reasonably conform to the invasion by a nonwetting fluid of a porous medium. Percolation theory deals with states of networks or bonds in lattices representing heterogeneous systems. Invasion percolation is applied to percolation models where the displacing fluid occupies the accessible site with the smallest capillary threshold pressure at each timestep. Percolation theory has been successfully applied to simulate capillary-dominated invasion of non-wetting fluids like oil and gas into water-wet porous geologic media by Carruthers and Ringrose (1998) and Glass and Yarrington (2003).

Carruthers (1998) introduced a technique to model secondary oil migration while honoring the geology and fluid physics at the scales controlling this phenomenon i.e. for low flowrate, "capillary creep" flow regimes where phase density contrasts and capillary entry pressures overwhelmingly control the trajectories of the advancing front and saturation profiles. He applies this new technique for modeling secondary oil migration such that it:

1. "Honors the scale of the migration pathways formed.
2. Uses capillary entry pressures and critical oil saturations to control when and where migration occurs.
3. Recognizes that discontinuities in the oil phase will occur and that the magnitude of the buoyancy force should only be calculated where an accumulation exists."

Permedia® is a result of the commercial development of this technique. Singh et al. (2010) compares CO_2 flow behavior models at Sleipner using traditional reservoir simulations (Eclipse 100 and Eclipse 300) and using invasion percolation simulations (Permedia) to actual seismic monitoring data. the authors found that "the invasion percolation simulation gave the best initial match to observed data, leading us to reassess the input assumptions for the black oil and compositional simulations". They propose a technique that combines invasion percolation simulations with traditional reservoir simulations to provide an upper and lower bound to expected plume behavior. Cavanaugh and Ringrose (2011) similarly use an invasion percolation modelling approach (application of Permedia) to simulate CO_2 migration in high resolution model (56 million cells with dimensions $10 \times 10 \times 2$ meters) of the In Salah storage site. The authors find that the simulated results are reasonably consistent with the inferred CO_2 distribution after 5 years of injection and that the CO_2 saturation distribution is primarily constrained by the fracture network.

2.3 Characterization of different regimes and the transition between the regimes: phase diagrams of fluid-fluid displacement

The fluid-fluid interface for immiscible fluid-fluid displacement in such conditions exhibits fractal structure at all scales down to the pore-scale (Lenormand and Zarcone, 1985). Wilkinson and Willemsen (1983) characterized immiscible displacement of fluids in simple 2-D Monte Carlo simulation models and defined local correlation lengths of the clusters formed for displacements at different Bond number. These models however, considered only the hydrostatic case where the system is assumed to be in a state of capillary equilibrium at any instant.

Lenormand *et al.* (1987) characterized immiscible fluid displacement in porous media using dimensionless numbers, viscosity ratio (M) and capillary number (C) by network models and supporting micromodel experiments. They established that depending on the nature of dominating force, viscous or capillary, displacement patterns can be one among three basic displacement types: viscous fingering, capillary fingering or stable displacement. They developed the famous 'phase-diagram' for drainage used as a basis for characterizing fluid displacements in porous media into different domains governed by different flow physics.

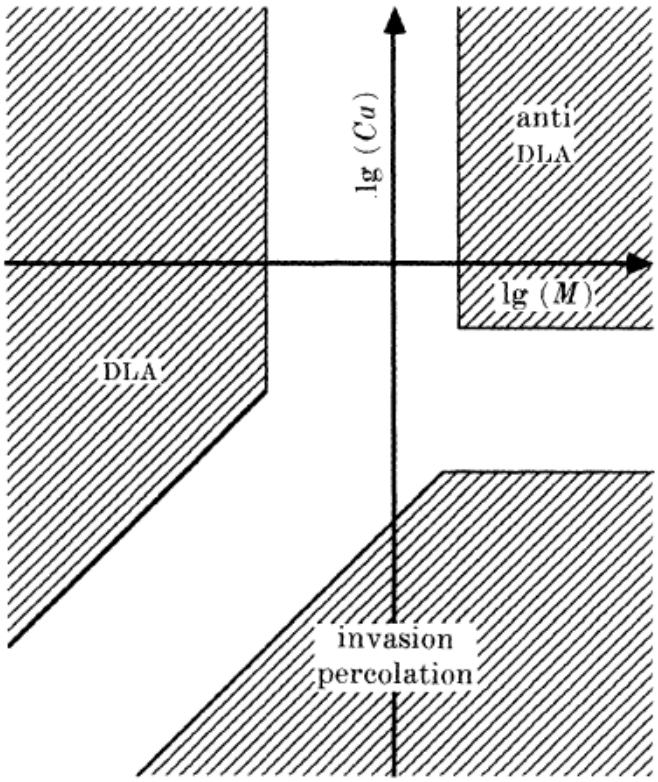

Figure 2-1: Phase diagram for 2-D immiscible displacements from Lenormand *et al.* (1988)

Lenormand *et al.* (1988) performed numerical experiments for immiscible displacements in porous media. The authors defined ranges of M (mobility ratio) and Ca (Capillary number) applicable for different flow regimes/ domains: viscous fingering, capillary fingering and stable displacement (Figure 2-1). Each of these three domains is governed by one of three different statistical models. In this work, we are concerned with capillary fingering which is governed by invasion percolation model.

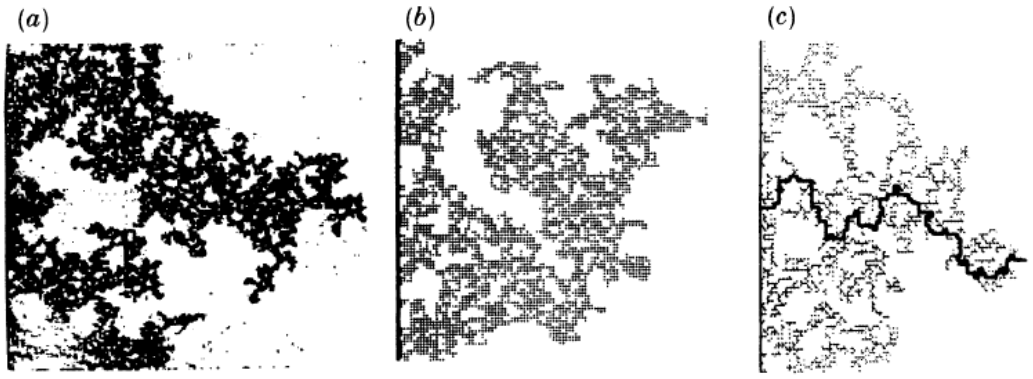

Figure 2-2: Comparison between capillary fingering patterns produced by a) micromodel experiment, b) computer network simulation and c) invasion percolation model (Lenormand, 1989). The case of non-wetting fluid injection into a 2-D porous medium made of interconnected capillaries is presented here. Micromodel experiments are performed in transparent etched networks. The computer simulations are the results of network simulator model "based on the physical rules of displacement at the pore scale" (Lenormand *et al.*, 1988). The statistical invasion percolation model that defines capillary fingering displacement gives the pattern in panel c)

Hou *et al.* (2003) performed diphasic pulsing experiments to study oil migration patterns in porous medium. They adopted Lenormand's phase diagram classification to recognize three domains governing migration patterns at various capillary numbers and modified bond numbers. In a related study, Cottin *et al.* (2010) report experimental results of two-phase flow in 2-D micromodels for capillary numbers between 10^{-7} and 10^{-2}. They propose a similar model to capture the scaling properties of capillary fingering observed experimentally. Similarly, Zhang *et al.* (2011) studied displacement stability and fluid saturation distributions in homogeneous water-wet pore network micromodel. Their study covered a wide range of viscosity ratios and capillary numbers and their results confirmed the numerical results by Lenormand *et al.* (1988). Ferer *et al.* (2004) used micromodel experiments and simulations of standard pore-level models to predict cross-

over behavior from capillary fingering to viscous fingering for immiscible, two-phase flow in porous media. They find "cross-over from capillary fingering (IPT-like) to compact or Euclidean behavior as capillary number was increased".

Our work handles realistic geology in the porous medium as well. We model real porous media at depositional resolution and study flow at constant viscosity ratio and very small capillary numbers. We deal with negligible viscous forces in our work and hence lie in the capillary fingering domain in Figure 2-1.

2.4 Realistic geologic domain representation: Model building

2.4.1 Threshold pressure domain from grain size distribution

Berg (1975) gives the mathematical relationship between capillary pressure and oil migration through porous sandstones. The relationship between grain diameter and capillary entry pressure (threshold pressure) for unconsolidated sediments was determined to be:

$$P_{th}\ (\text{Pa}) = 16.3 \times \frac{IFT(mN/m)}{D\_mm} \qquad \ldots (2\text{-}1)$$

where

IFT is interfacial tension, mN/m

P_{th} is threshold pressure, Pa

D_mm is the grain diameter, mm

Meckel (2012, in review) explains in detail the technique used to obtain the geologic samples used in this work and the methods to extract digital models of these samples. The grain sizes observed in the samples are used in Eq. 2-1 above to obtain threshold pressure values for our simulation models.

2.4.2 CO_2 and brine properties

Typical geologic storage schemes use formations deep enough (> 800 m) to ensure CO_2 is in a dense phase i.e. supercritical phase. The Atlas of Gulf of Mexico Gas and Oil Sands was published by BOEMRE (The Bureau of Ocean Energy Management, Regulation and Enforcement) in 1999, and updated in 2001, 2003, 2004, 2005 and 2006. The values of CO_2 densities from the 2006 sands file are used in this work. The frequency distribution for this density data is shown in Figure 2-3.

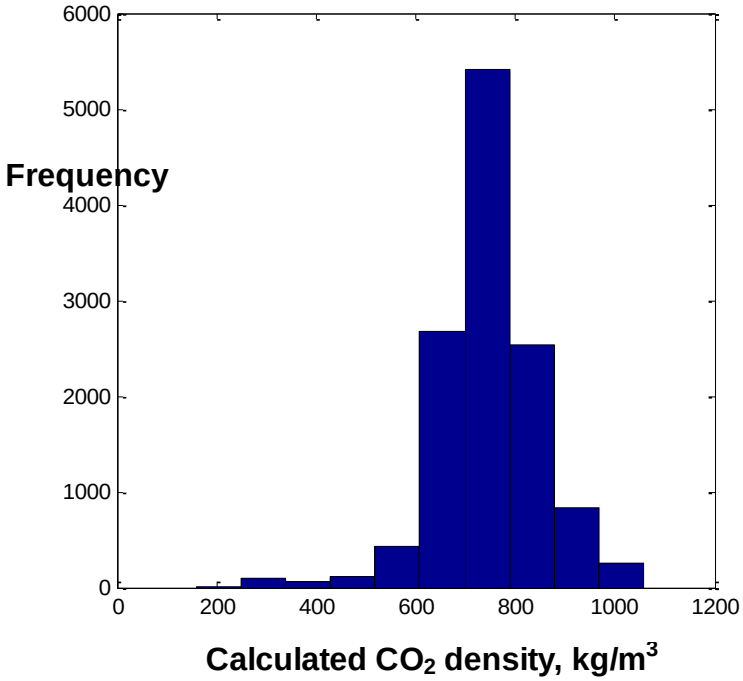

Figure 2-3: CO_2 densities calculated from pressure and temperature data (Atlas of Gulf of Mexico Gas and Oil Sands, 2006)

In this work, we assume a default density contrast of 300 kg/m^3 for our simulations, unless indicated otherwise. The fluid PVT properties for the full-physics simulation models are borrowed from the GEM model input properties in Saadatpoor (2009).

3) PHYSICS OF GEOLOGICAL CO_2 STORAGE

3.1 Fundamental concepts

Before we get into the dynamics of CO_2 movement in the reservoir, we shall review a few related fundamental concepts. We start by defining basic terminology and then proceed to understand the physics controlling CO_2 migration in the reservoir. We conclude with the assumptions we have made in building the simulation cases for capillary channel flow of CO_2.

3.1.1 Capillary pressure, P_c and threshold pressure, P_{th}

The capillary pressure of the leading edge of the CO_2 front P_c (Figure 3-1) is given by

$$P_c = \Delta\rho g h_{eff} \quad \text{..... (3-1)}$$

where

P_c is the capillary pressure at the leading edge of the CO_2 plume

$\Delta\rho$ is the density difference between CO_2 and native brine

h_{eff} is the effective height of the plume front measured vertically from the leading edge to the bottom of continuous column of migrating CO_2

g is the acceleration due to gravity

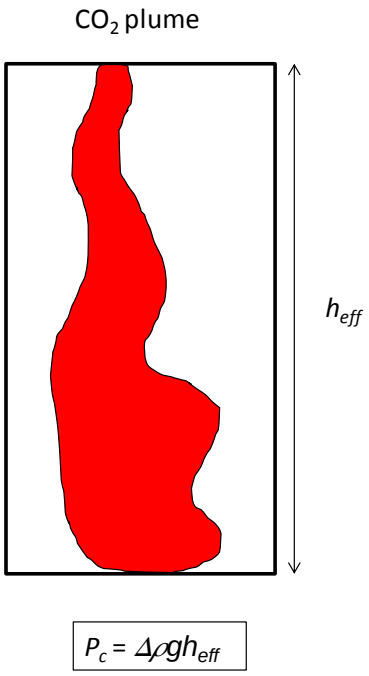

Figure 3-1: Illustration of the capillary pressure at the leading edge of CO_2 plume in a brine-filled rock. $\Delta\rho$ is the density difference between CO_2 and native brine and g is the acceleration due to gravity. h_{eff} is the effective height of the plume front measured vertically from the leading edge to the bottom of continuous column of upward migrating CO_2.

The capillary entry pressure or the threshold pressure for drainage, on the other hand, is a rock property. The ability of a rock containing wetting phase to be invaded by non-wetting fluid phase is expressed in terms of its threshold pressure. This is defined as the minimum pressure difference between nonwetting and wetting phases needed to initiate the displacement of a wetting phase by a nonwetting phase from the porous medium 100% saturated with the wetting phase.

There are various methods to obtain threshold pressure from physically measurable properties of a porous medium sample. In this work we arrive at the threshold pressure distribution of the media from the grain size distribution map of the geologic specimen.

For our epoxy-imbibed solid relief peel sample, the grain size distribution analysis is a reasonable way to estimate P_{th} values. Here, threshold pressure is calculated from the measured grain size distribution by assuming the simple Berg equation (Berg, 1975) applies for CO_2-H_2O system.

$$P_{th} = 16.3 \times \frac{IFT}{D\_mm} \quad \text{... (3-2)}$$

where

16.3 is an empirical constant, dimensionless

P_{th} is the threshold pressure, Pa

IFT is the interfacial tension, 30 mN/ m for CO_2- H_2O system

D_mm is the grain diameter, mm

3.1.2 Reservoir rocks and seal rocks

In this work we split rocks into two basic types. CO_2 is injected into and migrates through the 'reservoir rock'. The reservoir rock could consist of various depositional fabrics and corresponding grain size distributions. Hence the reservoir rock would be the heterogeneous medium we are primarily concerned with. We characterize the degree of heterogeneity of our reservoir rocks using the spatial and frequency distributions of threshold pressure, P_{th}. As buoyant CO_2 migrates through the reservoir rock, it may encounter 'seal rocks' which are massive capillary barriers. The seal rock is a different rock type with very high threshold pressure value, P_{th}^{seal} compared to the reservoir rock. Typical CO_2 plume heights are such that the P_c of Eq.3-1 << P_{th}^{seal} and hence CO_2 cannot breach this capillary barrier. Oil and gas accumulations found in nature are a result of accumulation beneath such seal rocks.

3.1.3 Grain-size data: Brief review

Sediment (grain) sizes are measured using the phi scale. Phi, ϕ is defined as the negative log base 2 of the grain diameter in mm. Boggs (1994) explains important characteristics of grain size distribution as follows:

"Grain size is a fundamental property of sedimentary rocks which affects the related derivative properties of porosity and permeability. Because the size and sorting of sediment grains may reflect sedimentation mechanisms and depositional conditions, grain-size data are assumed to be useful for interpreting the depositional environment of ancient sedimentary rocks.

The sorting of a grain population is a measure of the range of grain sizes present and the magnitude of the spread or scatter of these sizes around the mean size. The mathematical expression of sorting is standard deviation. In conventional statistics, one standard deviation encompasses the central 68% of the area under the frequency curve i.e. 68% of the grain-size values lie within plus or minus one standard deviation of the mean size. Verbal terms for sorting corresponding to various values of standard deviation are as follows (after Folk, 1974):

Standard deviation	
<0.35ø	very well sorted
0.35ø – 0.5ø	well sorted
0.5ø – 0.71ø	moderately well sorted
0.71ø – 1.0ø	moderately sorted
1.0ø – 2.0ø	poorly sorted
2.0ø – 4.0ø	very poorly sorted
>4.0ø	extremely poorly sorted"

Grain-size analyses of the peel specimen can thus be used to explain geologic controls on peel topography. This quantitative detailing of physical samples helps us study the influence that these small-scale sedimentary structures have on buoyant fluid migration by enabling a physically based assignment of relevant petrophysical properties. We use the simplistic Berg equation (Berg, 1975) to convert the range of grain sizes in a rock to the range of threshold pressures in the rock. Hence the poorer the sorting, the wider the range of grain sizes and range of threshold pressures in that medium.

3.1.4 Invasion percolation

The capillary number *Ca* is a dimensionless measure of the relative strength of viscous and capillary forces. If $Ca < 10^{-4}$, then the system is said to be capillary-dominated; in our application this means any fluid motion would be primarily buoyancy-driven (England *et al.*, 1987). The basic physics of buoyant migration of the non-wetting CO_2 phase through a heterogeneous domain is an extension of invasion percolation. Invasion percolation is sufficient to model the fluid flow structure obtained under very slow drainage conditions (negligible viscous forces) for sufficiently heterogeneous domains. The key rule governing invasion percolation at the pore scale, i.e. where an individual meniscus is entering a pore throat, is that if the capillary pressure (P_c) exceeds the threshold pressure (P_{th}) of the pore throat, then nonwetting fluid passes through the throat and enters the adjoining pore; otherwise the pore throat continues to act as a barrier. If the nonwetting phase enters the pore, then it thereby has access to new pore throats, and the same condition for invasion of these throats is applied. Figure 3-2 depicts the basic principle of invasion percolation.

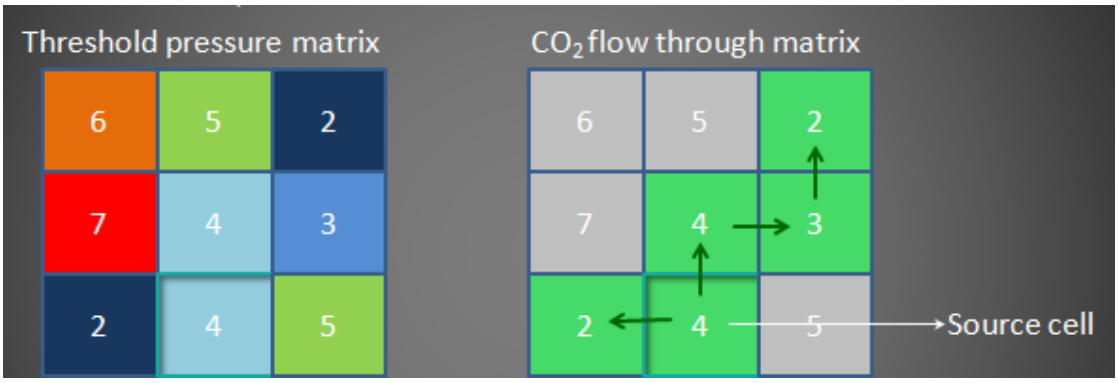

Figure 3-2: Schematic of the principle of invasion percolation in a porous medium. (Left) The individual cells represent pore throats having the indicated threshold pressure value. CO_2 is sourced with a capillary pressure equal to the threshold pressure (4 pressure units) of the source cell (middle cell of bottom row, outlined in green) and allowed to percolate through the matrix. (Right) The cells highlighted in green depict the migration path of CO_2 in this medium.

For buoyancy driven flow, the capillary entry pressure is provided by the buoyancy gradient, so the displacement of brine and flow of CO_2 occurs when

$$\Delta\rho g h_{eff} \approx P_{th}$$

Consider the spatial distribution of threshold pressure in a porous medium as in Figure 3-2. The numbers in the cells represent the values of threshold pressure (psi or kPa) for each pore throat in the medium. Suppose CO_2 were to be introduced into this system from the 'source cell' (middle cell in the bottom row here) with capillary pressure equal to the threshold pressure of the 'source cell' at 4 pressure units. Under the rules of invasion the CO_2 will move through only those cells to which the CO_2 has access and which have threshold pressure values less than or equal to 4 pressure units. The cells with threshold pressure values greater than 4 pressure units would behave as capillary barriers that do not allow flow of CO_2 through them. Hence the green cells in the panel to the right in Figure 3-2 would represent the final migration path of CO_2 through this matrix.

The essence of invasion percolation is that CO_2 would go through all the pore throats that it **can** penetrate. Where external pressure gradients (viscous forces) are negligible, away from the influence of injection, frontal advance is governed by two factors only, the capillary pressure of the CO_2 plume (determined by column height of CO_2 and density difference between CO_2 and brine) and the threshold pressure distribution of the pore throats in the medium. Here we employ the extension of this concept to flows at larger scales, which replaces the pore throat with a volume of rock with a characteristic value of capillary entry pressure. The capillary channel flow regime occurs wherever buoyancy drives the CO_2 migration, i.e. in most of the reservoir, and where the capillary pressure at the leading edge of the plume is comparable to this characteristic threshold pressure.

3.2 Qualitative aspects of CO_2 storage

We envisage the process of CO_2 sequestration with focus on the dynamics of fluid flow through time and space in the storage reservoir. We take CO_2 to be the non-wetting phase and native brine as the wetting phase fluid present in the pore spaces of the rock. The storage reservoir considered in our study is brine-filled formation (saline aquifer). When buoyant CO_2 travels to displace the native water, this scenario is a drainage process.

Sequestration of CO_2 typically involves getting as much CO_2 into the storage reservoir as possible. To achieve this, the field operator would inject CO_2 at high injection pressures limited by the estimated fracture pressure of the reservoir rock. For example, the Sleipner project has been injecting 1 million metric tons of CO_2 per year since 1996 at a supercritical bottomhole flowing pressure of approximately 10.5 MPa which is below the fracture pressure of the rock. When CO_2 is injected into a storage reservoir during sequestration, viscous forces dominate flow behavior near the wellbore due to high injection rates and large pressure gradients (regime (a), Figure 3-3). Typical injection of CO_2 is done in the lower strata of the storage reservoir. The shape of the CO_2 saturation front in this typically near-wellbore region is determined by the spatial correlation of

permeability in the storage formation. Due to its large capillary pressure CO_2 completely floods all the pores it encounters in the rock here. Close to the wellbore we expect the CO_2 to displace brine down to residual saturation (we ignore the drying front: Noh *et al.*, 2004; Ozah *et al.*, 2005; Celia and Nordbotten, 2009). As CO_2 advances into the medium farther from the injection well, the velocity of propagation of CO_2 and the pressure gradient decrease. Eventually the pressure gradient from injection becomes negligible compared to buoyancy forces. This point is closer to the wellbore after injection ends. At this point capillary forces begin to determine whether the meniscus between migrating CO_2 and native brine will move into a pore throat, and by extension, whether the CO_2 phase will displace brine from a volume of rock. Flow in this buoyancy-driven regime is driven by the density difference between CO_2 and native brine. Radial pressure profiles (analytical solutions) for typical injection wells (Figure 1-6) indicate that this regime change occurs within hundreds of meters from the wellbore itself.

As CO_2 progresses through the reservoir rock, being driven by buoyancy and influenced by capillarity, a competition emerges between the CO_2 plume height (and hence the capillary pressure at the leading edge of the front P_c) and the magnitude of the threshold pressures P_{th} in the reservoir rock. Generically three possible outcomes exist for this competition, yielding flow regimes (a), (b) and (c) in Figure 3-3.

In flow regime (a), $P_c > \max(P_{th})$, i.e. the capillary pressure exceeds the maximum threshold pressure of the reservoir rock and *compact flow* of CO_2 occurs where CO_2 enters every pore throat it encounters. This would be a continuation of the near-wellbore viscous-dominated migration regime, with brine displaced down to its irreducible saturation.

In flow regime (b) $\min(P_{th}) < P_c < \max(P_{th})$, i.e. the CO_2 capillary pressure is greater than the smallest threshold pressure but does not exceed the highest threshold pressure in that portion of the reservoir rock. The CO_2 migration pattern adopts a *capillary channel* structure characteristic of invasion percolation (where the direction of invasion is

vertically biased due to buoyancy, in contrast to conventional invasion percolation models in which invasion is isotropic). Because CO_2 migrates through potentially much less of the rock volume in this regime, a given mass will migrate much farther than in compact flow, with important consequences for CO_2 storage. .

In flow regime (c) where the capillary pressure is smaller than the minimum threshold pressure of a *seal rock*, i.e. $P_c < \min(P_{th}^{seal})$, further migration of the plume is blocked or redirected. If CO_2 cannot migrate around this barrier, it will accumulate with progressively increasing P_c similar to natural reservoirs of hydrocarbon or CO_2. *Secondary accumulation beneath a seal* rock occurs when CO_2 plume encounters rocks with very high threshold pressures (characteristic of seal / cap rocks) compared to *Pc* of CO_2. If CO_2 can accumulate enough to build up capillary pressure such that $P_c > min(P_{th}^{seal})$, then CO_2 plume can breach this barrier, else CO_2 remains trapped under it for geologic time.

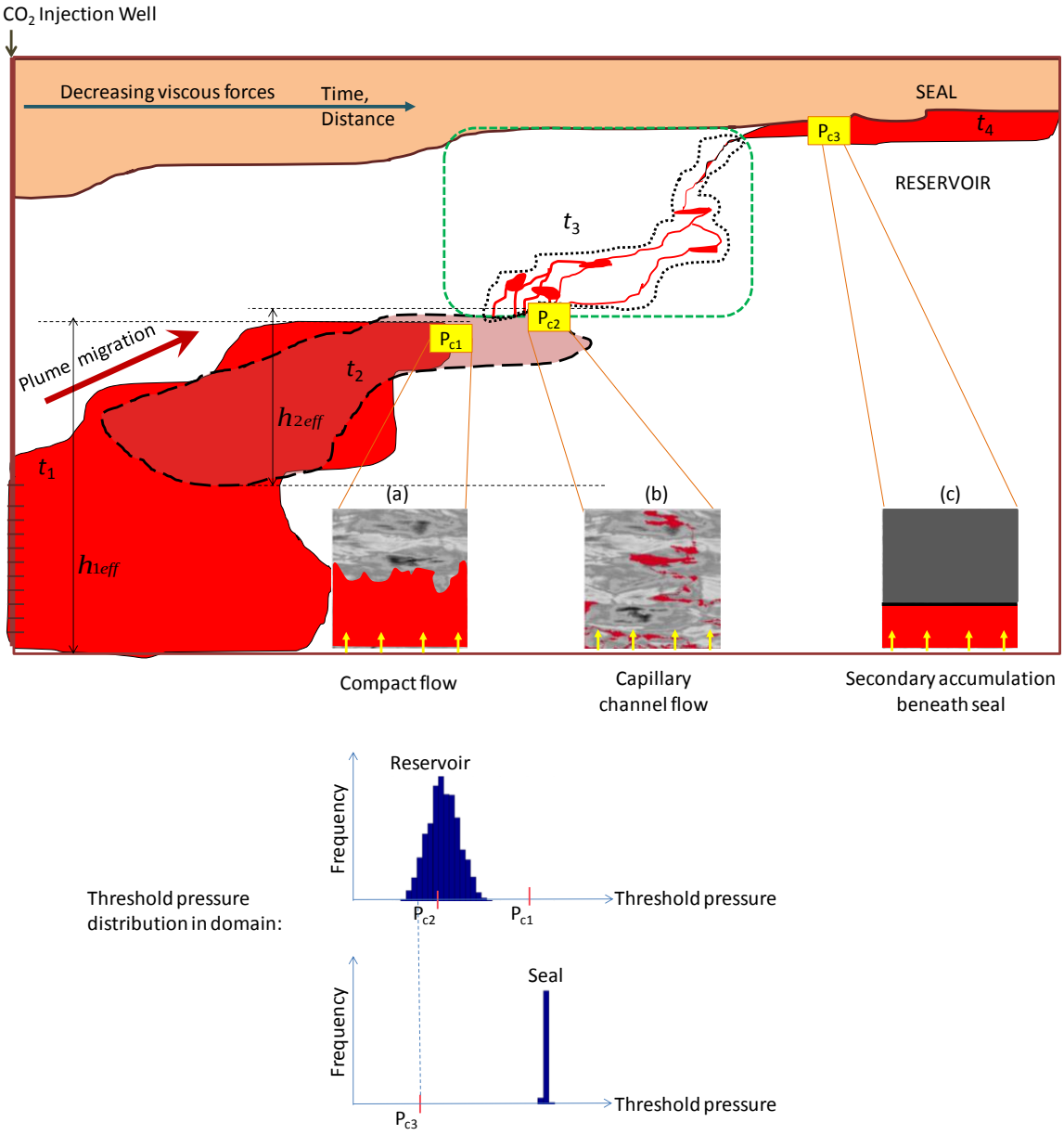

Figure 3-3: Schematic of spatial and temporal evolution of CO_2 flow regimes from viscous-dominated to buoyancy/capillarity-dominated. The storage reservoir is heterogeneous with a threshold pressure field P_{th} with frequency distribution shown at the bottom of the diagram; the sealing formation has a much larger threshold pressure. h_{eff} is the effective height of the plume front measured vertically from the leading edge to the bottom of continuous column of migrating CO_2. At time t_1, for a continuous column

height of h_{1eff} the capillary pressure at the leading edge of the CO_2 plume is $P_{c1} = \Delta\rho g h_{1eff}$. As the CO_2 plume moves through time (outlines of plume at times t_1 through t_4 are shown as black solid or broken lines) and distance in the storage reservoir (extreme vertical exaggeration), possible flow regimes are: (a) *compact flow* where $P_{c1} > \max(P_{th})$; (b) *capillary channel flow* where $\min(P_{th}) < P_{c2} < \max(P_{th})$; and (c) *secondary accumulation beneath a seal* where $P_{c3} < \min(P_{th}^{seal})$. The yellow arrows in the insets describing the flow regimes indicate the CO_2 being sourced from the bottom of the rock section. In this work, we explore flow regime (b) within the green dotted rectangle.

The competition between capillary pressure and threshold pressure exhibits rich dynamics (Saadatpoor *et al.*, 2009; Singh *et al.*, 2010; Zhang *et al.*, 2011) for three reasons: 1) the influence of injection pressure gradient varies with distance from the injection well and with time; 2) the plume height (h_{eff}) and hence P_c varies with distance traveled especially once injection ceases and subsequent migration leaves residual CO_2 saturation behind; and 3) spatial heterogeneity in the petrophysical properties (P_{th}) of the storage formation. The three flow regimes have very different implications for the extent of plume migration and for storage efficiency. Thus it is important for simulations of sequestration to capture these various regimes. Compact flow is familiar from the coarse-grid simulations commonly applied to storage at the reservoir-scale (e.g. Eclipse, GEM); these simulations typically neglect capillary pressure. The influence of seals is also familiar, though usually encountered as a region of very small or zero permeability imposed on the domain, rather than as a capillary barrier. We explore capillary channel flow by explicitly accounting for the heterogeneous distribution of threshold pressures of the rock in this work.

3.3 Model assumptions: Tie-back to the big picture

In this work we present simulations of CO_2 migration and displacement patterns for the capillary channel flow regime (regime (b); green dotted rectangular region in Figure 3-3). We assume that CO_2 is migrating through the reservoir post-injection under hydrostatic

conditions or at a sufficient distance from the injection well during injection and now this compact plume has capillary pressure (column height) that is comparable to the threshold pressure distribution of the rock section it comes into contact with. We treat the limiting case in which a compact plume has just reached the point of transition to buoyancy-dominated migration. Thus a line source (in 2D simulations) of CO_2 is placed at the bottom of the rock section under study. As shall be demonstrated in the next chapter, the line source gives limiting case of the characteristic migration paths which we analyze for effective rock-fluid contact.

We work with meter-scale rock specimen at high resolution (~2.7 million points ranged at about 25 data points per sq. mm of specimen; Figure 4-5) and simulate CO_2 migration upwards from the bottom of this rock section. Our work investigates CO_2 flow in the capillary channel regime during the upward migration of CO_2 far from any extensive flow barriers (seals or cap rocks) in a domain assumed to be part of a laterally continuous reservoir section. We thus assume that the porous medium is laterally continuous and the migrating fluid does not see the effects of boundaries. Our simulations thus assume periodic lateral flow boundaries for the model domains. The height of the compact plume is assumed sufficient for CO_2 to enter the domain. In the IP simulator, P_c is initialized with the minimum threshold pressure of the region contacted by the source and the plume builds column height until percolation. Percolation is said to occur once CO_2 traverses the entire height of the model domain and reaches the top boundary. We record the percentage of the model domain invaded by CO_2 at percolation to characterize rock-fluid contact for different invasion patterns.

As CO_2 tries to rise through each rock section, displacing the native brine, the capillary channels take up interesting structures. We find that within the capillary channel regime, we get CO_2 migration pathways (patterns) ranging from capillary fingering structures to structures that fill up much bigger accumulation pools of CO_2 in the domain (back-filling structures).

For the purpose of this study we ignore residual saturation trapping, dissolution and geochemical reactions and consider only the mechanism of local capillary trapping (Saadatpoor, 2009) to occur during the migration of CO_2. The presence of these neglected trapping mechanisms would only serve to restrain further migration of CO_2 in the reservoir and aid in increasing long-term storage security.

3.4 Quantification of results: Characterization

We characterize upward CO_2 migration in brine-filled rock sections on the basis of fundamental rock and fluid properties in the system.

Rock properties: In nature, no two reservoir rocks are exactly the same. We use two variables to characterize rock heterogeneity in our model domains: the spatial distribution of grain sizes (grain size is a surrogate for permeability) and the range of grain sizes distributed in the rock. The spatial distribution of grain sizes can also be expressed in terms of the correlation length of the threshold pressures in different principal directions. Here, we investigate the influence of depositional fabric of the porous medium by varying the correlation length of the threshold pressure values in the horizontal and vertical directions. The range of grain sizes is a primary influence on the heterogeneity of the rock with more homogeneous media having narrower ranges of grain size and the heterogeneity increasing as the width of the range of grain sizes (analogous to sorting) increases. Hence the second variable in our sensitivity analysis is the range of threshold pressure distribution in the medium.

Fluid properties: The fluid property that affects buoyant fluid migration is the density difference between CO_2 and native brine. We explore the effect of increasing density difference between CO_2 and brine, and hence increasing buoyancy forces in the medium. The percentage of CO_2 invading the domain at percolation and the D-metric (explained below in section 3.4.4) are quantitative aids we use to characterize capillary invasion patterns. In this study, we use the following definitions of parameters to characterize our results:

3.4.1 Fluid property: $1/(\Delta\rho g)$

The term $1/(\Delta\rho g)$ represents the reciprocal of the buoyancy forces in the system and is a function of the fluid properties where $\Delta\rho$ is density contrast between CO_2 and native brine and g is acceleration due to gravity.

3.4.2 Rock properties:

a. Dimensionless threshold pressure field, $<P_{th}>/\sigma_{Pth}$

The term $<P_{th}>/\sigma_{Pth}$ is a measure of the extent of variation or spread with respect to a given mean threshold pressure (and hence mean grain size). Larger values of the dimensionless threshold pressure imply little change in average grain size with location in the domain, and relatively little variation in sorting with location in the domain.

b. Correlation lengths of threshold pressure in specific directions

We build geostatistical models with prescribed correlation lengths of threshold pressures in the horizontal and vertical directions. We input the correlation length of P_{th} in both these directions as a multiple of the cell height (dz; constant for all models). Hence we can define ratio of correlation lengths of P_{th} in the horizontal and vertical directions. For a fixed horizontal correlation length with respect to the cell height, we vary the vertical correlation length for different models and hence can also define the ratio of horizontal to vertical correlation length to characterize our simulation models.

3.4.3 Percentage of the domain invaded by CO_2 at percolation

We let carbon dioxide migrate upward from the source at the bottom of the domain until it reaches the top boundary. We measure the percentage of the domain invaded by CO_2 at percolation as a measure of the effective rock-fluid contact volume for that simulation.

Percentage of the domain invaded by CO_2 at percolation is defined as
% of the domain invaded by CO_2 at percolation = *number of cells in the model domain in which CO_2 is present / total number of cells in the model domain.*

Invaded CO_2 fraction at percolation gives the buoyant fluid saturation pathway spanning the vertical dimension of model. This measure would be used throughout for the quantification of CO_2 presence in different simulations.

3.4.4 'D-metric': Quantitative index

We attempt to characterize the migration patterns in the capillary channel flow regime with a dimensionless quantity. This dimensionless quantity, which we call the 'D'-metric, would help corroborate visual differentiation of the migration patterns and quantify the degree of 'compactness' of the saturation distribution in the porous medium. The 'D' metric concept has been borrowed from Carruthers (1998) and modified for implementation on the results of our simulations.

We calculate the D-metric or the D-index as follows (Figure 3-4 and 3-5):
Step 1: From the saturation map of the model domain at any given time step, we count the number of saturated cells in a 9-cell window centered on the saturated cell. This 9-cell window moves row-wise in a regular fashion through the entire model domain.

Small values of the D-metric imply fingers or very disperse saturation distribution while large values of D-metric imply very compact, filled structures. Theoretically, the least D value possible is 1 while the largest D value possible is 9. For a connected CO_2 column, the least D-value would be 2 while 9 would be the maximum for a CO_2 accumulation.

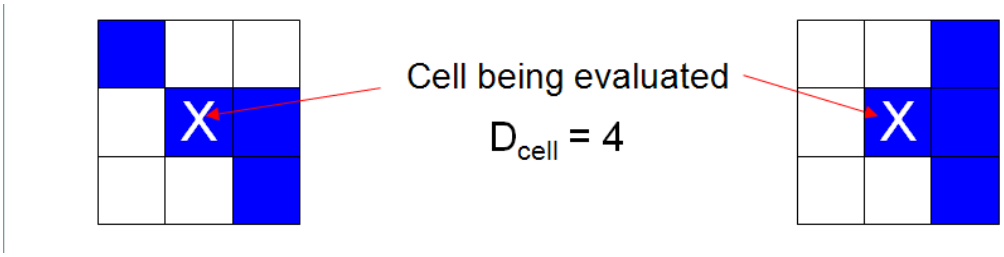

Figure 3-4: Cell counting to determine D-index. A D-index of 4 could mean different possibilities of saturation distribution but all with the same degree of 'compactness'.

The frequency histogram of D-metric for all the cells in the domain gives an idea of the rough saturation density in the medium (Figure 3-5).

(a) Color coded plot of D-metric

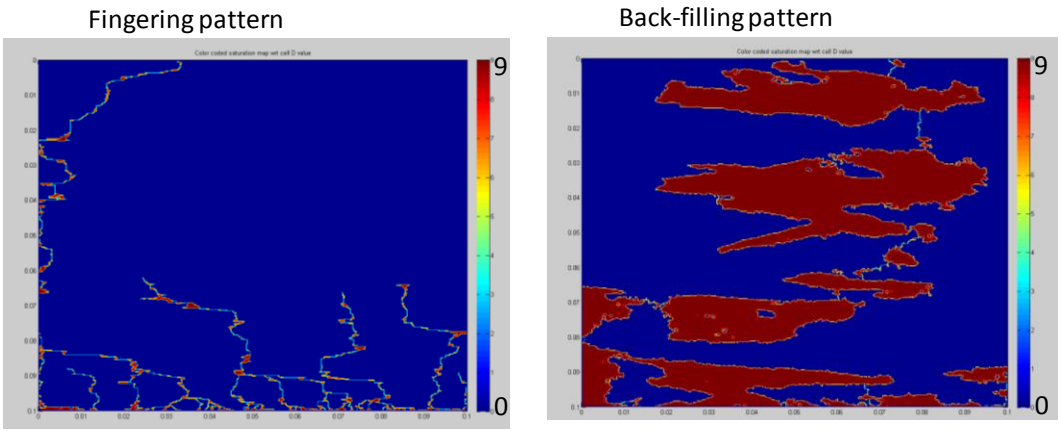

(b) Cellwise probability estimation of D-metric

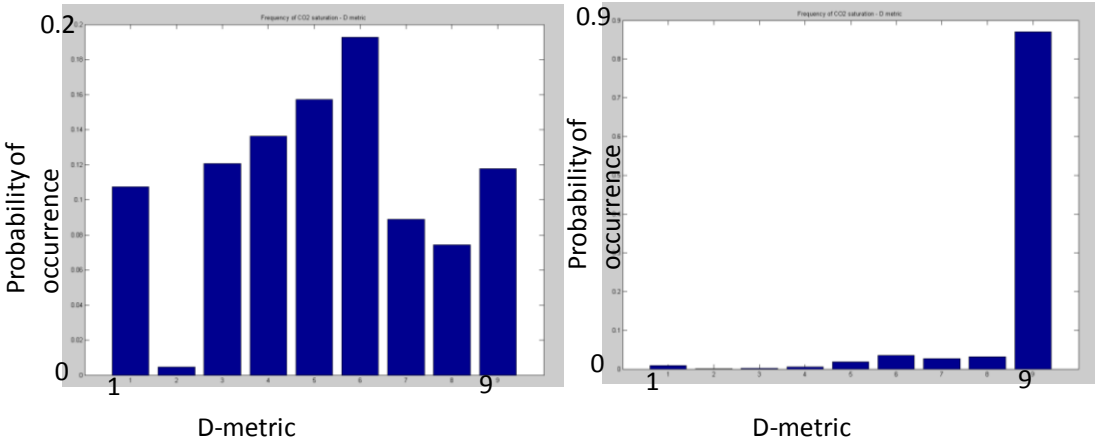

Figure 3-5: Frequency/ Probability histogram of D-metric for fingering and back-filling invasion patterns. The panels on the left represent a fingering pattern while the panels on the right represent back-filling pattern. The top row shows the color coded plot of D-metric while the bottom row is the cellwise probability of the D-metric being a certain value. D-metric of '0' indicates the background domain where no CO_2 is present. Difference is clearly visible between regimes. Back-filling patterns have most of the domain having high D values (accumulations) with hardly any smaller D values for the narrow connection paths between the accumulations.

Step 2: The average D-metric for the domain at a given time step in a model is determined by normalizing the D-metric by the total number of saturated cells in the domain.

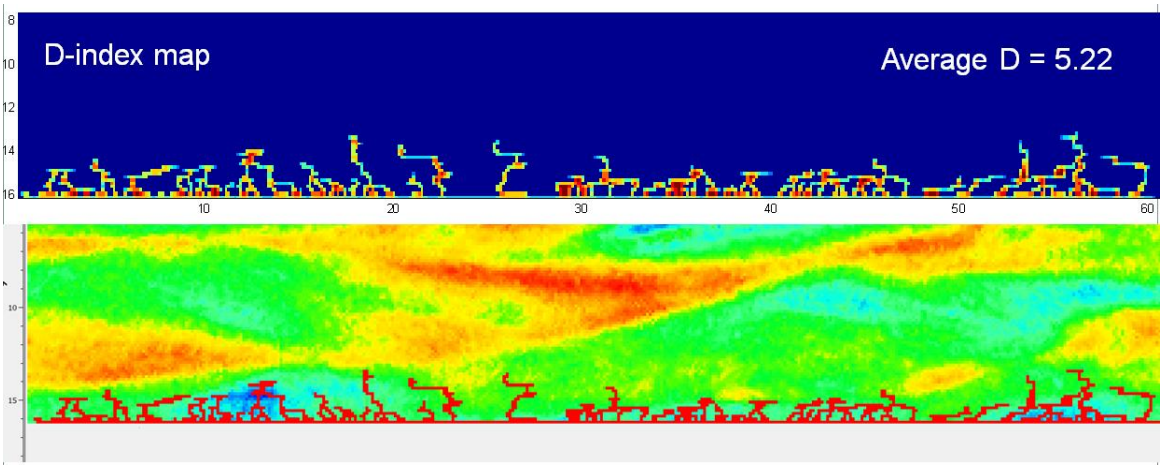

Figure 3-6: Map illustrating the calculated D-metric for a sample line source simulation. (lower panel) Red cells connected to the line source at the bottom of the domain indicate the presence of CO_2. Color scale in rest of image indicates the rock property of threshold entry pressure. (Upper panel) The D-index map with hotter colors indicates higher values of D. D values vary from 1 to 9. The average D value for this example is found to be 5.22 which points to the sparseness of the CO_2 saturation in the domain.

Figure 3-6 depicts the evaluation of the D-metric. Panel at the bottom of Figure shows the saturation map of CO_2 (in red) in a sample model domain. To determine the average D-metric we perform the calculation steps listed earlier. The saturation map is redrawn as the D-metric map with the color scale indicating the values of D for that particular cell. The average D is found to be 5.22 for this sparse saturation distribution in the model domain.

4) MODEL BUILDING

4.1 Introduction

We simulate CO_2 migration in the capillary channel flow regime in 2-D and 3-D models with various underlying depositional fabrics. We build the digital depositional fabric of our isotropic models in two ways: statistically and from real physical samples.

Geostatistical models are a common method to investigate fluid flow behavior in reservoir rocks. We generate geostatistical models of synthetic rocks using the "FFT Simulation" code from Jennings (2000). This software produces a desired number of threshold pressure values based on statistical properties like the Dykstra-Parson's coefficient (0.7) and the probability distribution function. The output has a mean of zero and the variance that is specified in the input as sill. Post-processing is needed to convert the output column data into the threshold pressure matrix with desired mean and standard deviation values. This generates heterogeneous domains with realistic correlation lengths of threshold pressure in the two principal directions, namely, horizontal and vertical directions. Stochastic parameters used for the threshold pressure field are given in the table 4-1. The mean threshold pressure value corresponds to upper very fine sand. Figure 4-1 gives the resulting threshold pressure fields.

Parameter	Value		
	Fabric (A)	**Fabric (B)**	**Fabric (C)**
Correlation length in x direction, m	0.024	0.024	0.024
Correlation length in y direction, m	1e-6	1e-6	1e-6
Correlation length in z direction, m	1e-6	0.0024	0.024
Cell dimensions: $dx = dy = dz$, m	0.00024	0.00024	0.00024
Mean, $< P_{th} >$, kPa	10	10	10
Standard deviation of $\ln(P_{th})$	1	1	1
Horizontal correlation length of P_{th} / Vertical correlation length of P_{th}	100	10	1
Horizontal correlation length of P_{th}, number of cells	100	100	100

Table 4-1: Stochastic input parameters used to derive the threshold pressure field

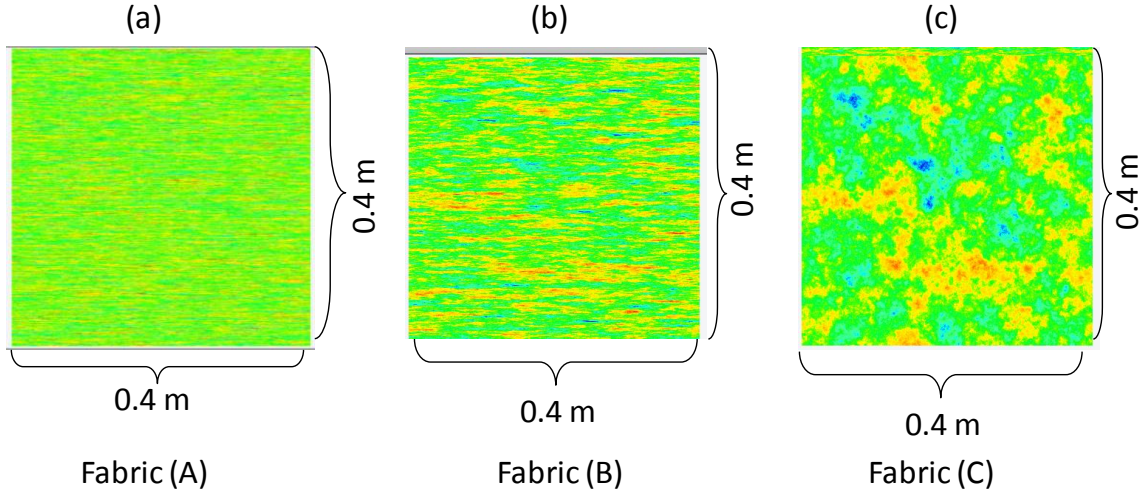

Figure 4-1: Geostatistical simulations of threshold pressure (in kPa) used for the correlation length sensitivity studies in this work. The horizontal correlation length of P_{th} is held constant (= 100 × cell height). The vertical correlation length is varied as a) = none, b) = 10 × cell height, c) = 100 × cell height. The 2-D domain consists of 2000 ×

2000 cells that are 2 mm × 2 mm each. The color scheme from cooler to hotter colors represents increasing threshold pressure values. The frequency distribution of threshold pressures is normal in nature. We label the models as Fabrics (A), (B) and (C) for use in this study.

We also create digital model domains from two real geological specimens. The physical specimens are quasi-2D fluvial sedimentary samples from the well-studied Brazos basin. The first peel (peel # 1; ~1.0 m × 0.5 m) represents depositional fabric transverse to flow direction. A second peel (peel # 2; ~0.4 m × 0.6 m) oriented parallel to depositional flow (i.e., perpendicular to the working model) was taken concurrently at the same location. Figure 4-2 shows the peel samples. We extensively use the depositional fabric of peel # 1 sample in our research.

Figure 4-2: Peel sample # 1 and #2. The peels are fluvial relief samples obtained from the Brazos basin. Peel # 1 is ~ 1 m tall × 0.5 m wide while peel # 2 is ~ 0.4 m tall× 0.6 m wide.

The peels have a specific depositional fabric and grain size distribution. We wish to investigate a wider range of threshold pressure distributions (spatial variation of average grain sizes). This would help us understand the range of migration behavior practically possible in rocks with varying degrees of heterogeneity. For this purpose we also create a set of models that retain the same depositional fabric, but with the different threshold pressure distribution assigned to the domain.

A tray of unconsolidated sand samples (Figure 4-3(a)) with various mean grain sizes and sorting coefficients is a realistic example representing different facies with varying degrees of heterogeneity. Each row in the sample tray is a particular sorting while each column has a particular median grain diameter as shown. The rows moving downward from the top have progressively worse sorting while the columns from left to right have smaller mean grain sizes (finer grained). The grain sizes are lognormally distributed in nature (Figure 4-3(b)).

Figure 4-4 gives the dataset of threshold pressure distributions we use in this work. The rows in Figure 4-4 have fixed standard deviations of threshold pressure while the columns have fixed mean threshold pressure values. The standard deviations of threshold pressure (σ_{Pth}) increase from 0.013 kPa to 22.28 kPa as we move row wise from the top towards the bottom row. The mean threshold pressure ($<P_{th}>$) values increase from 0.58 kPa to 11.8 kPa as we move from left to right column-wise. We input these threshold pressure distributions to domains with different depositional fabrics to create media of varying degrees of heterogeneity. The model domains are labeled using the colloquial term 'sorting' as a synonym for the standard deviation of their respective threshold pressure distributions. Extremely well-sorted (EW) domains hence have the least σ_{Pth} = kPa and so on as shown in Figure 4-4.

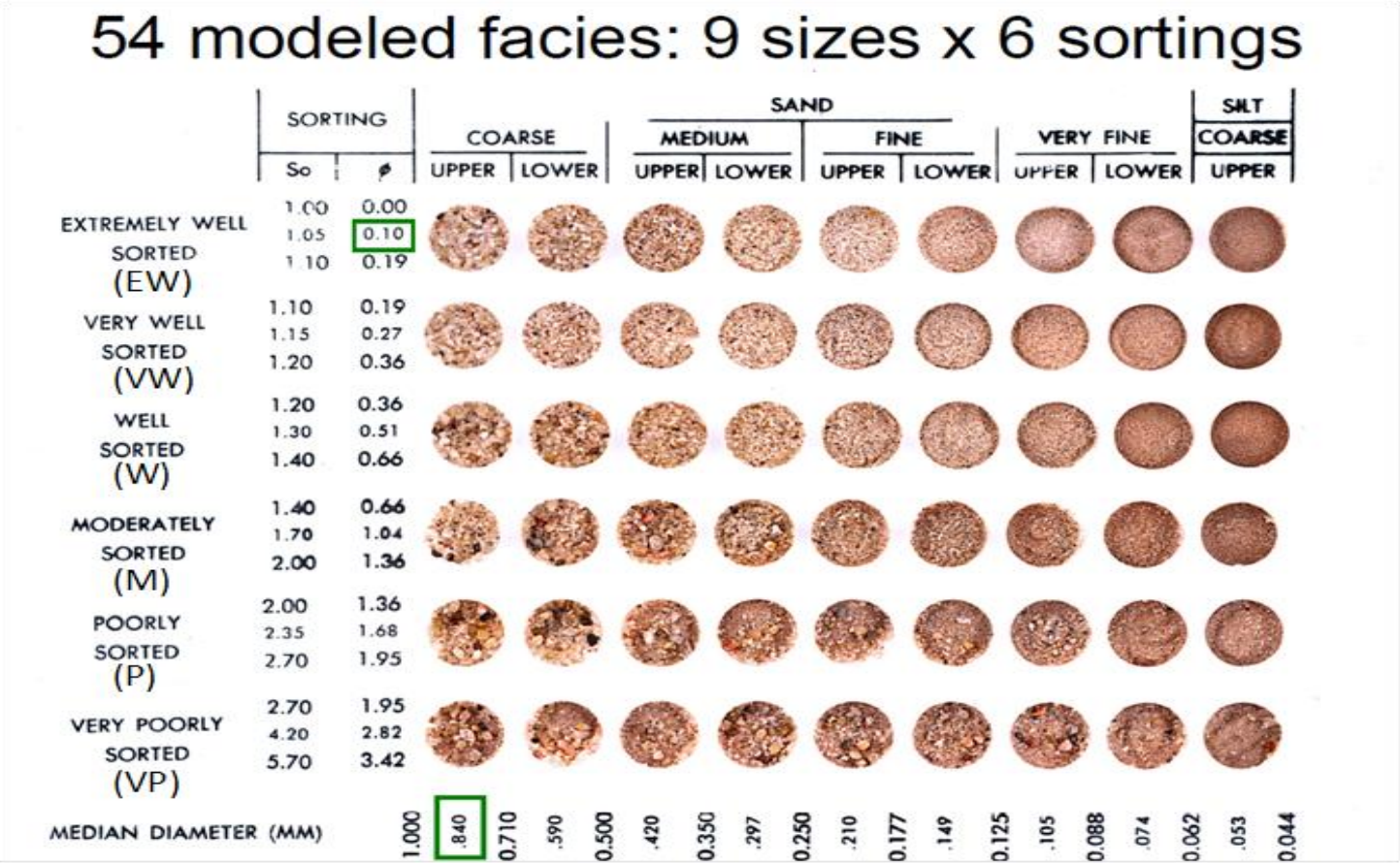

(a) Unconsolidated sand sample tray. Each row represents a specific sorting with the rows moving downward from the top having decreasing sorting / worse sorting. Each column represents a specific mean grain size with the columns from left to right having decreasing mean grain sizes.

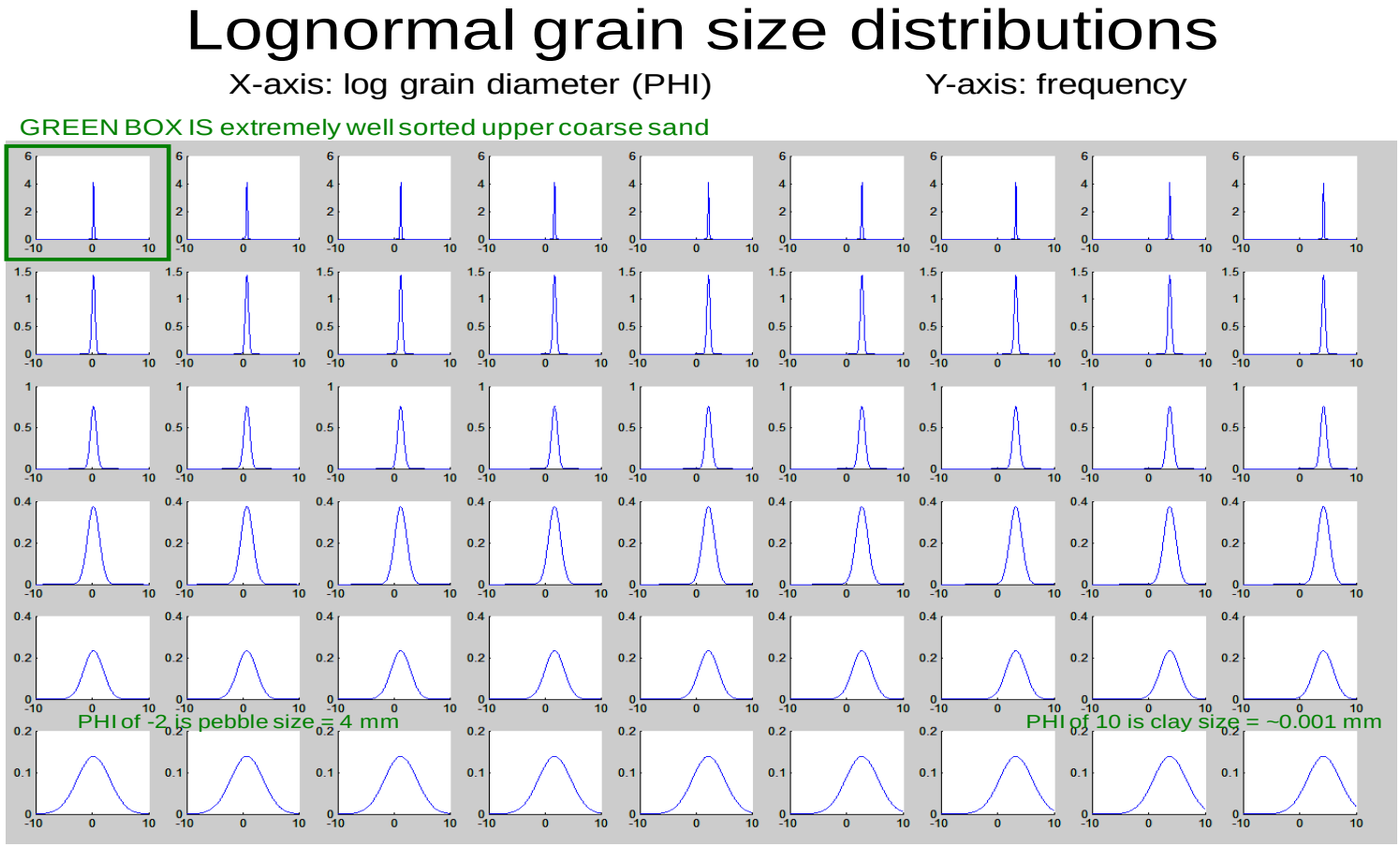

(b) Grain size distribution dataset extracted for the unconsolidated sand sample tray shown above. Grain size distribution: X-axis is phi values (log grain diameter) and Y-axis is frequency.

Figure 4-3: Grain size distribution from tray sample of unconsolidated sand grains representing different depositional facies.

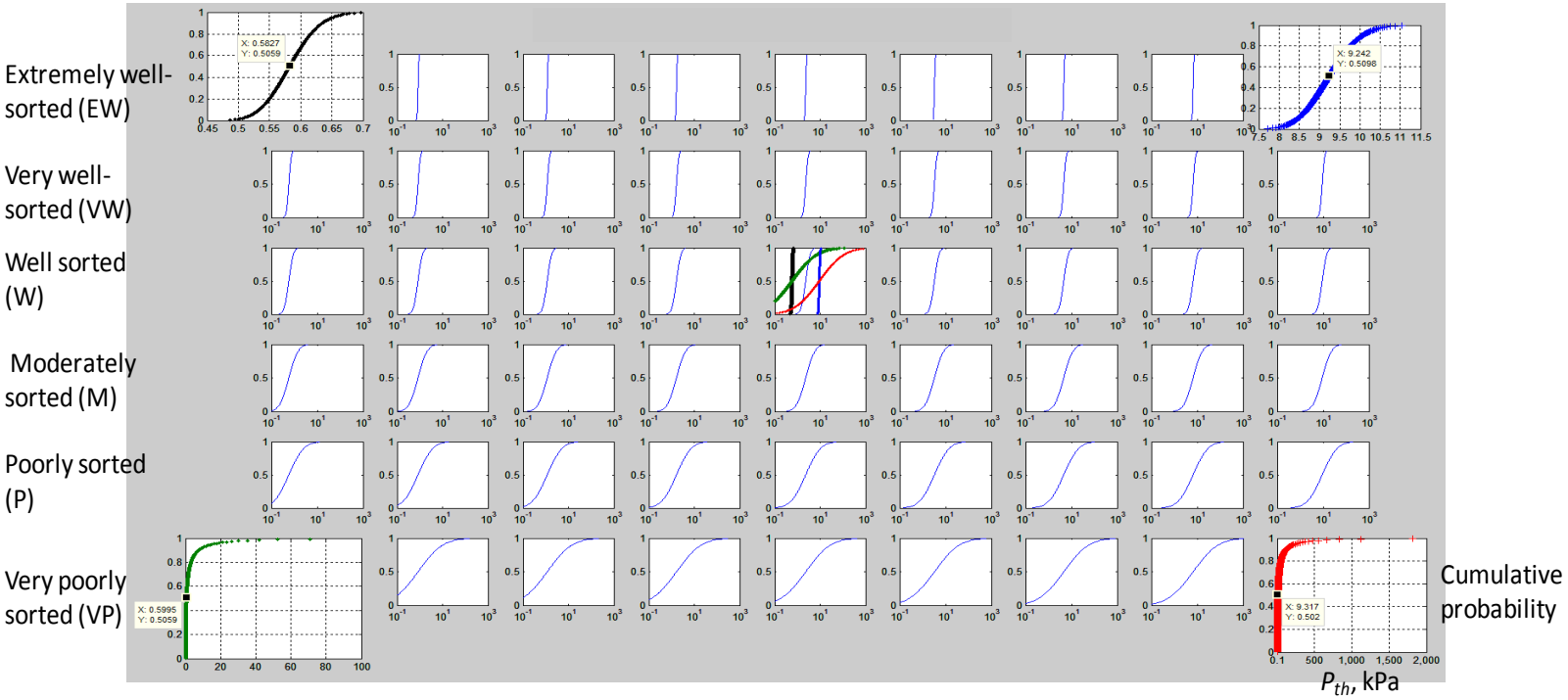

Figure 4-4: Threshold pressure distribution dataset: Cumulative Distribution Function, CDF of threshold pressure distribution. X-axis is P_{th} values (kPa) and Y-axis is cumulative probability. Each row has a particular standard deviation (σ_{Pth}) while each column has a particular median threshold pressure value as shown. The rows moving downward from the top have increasing σ_{Pth} while the columns from left to right have increasing $<P_{th}>$. Corner plots have linearly-scaled P_{th} while the others are in log-scale. The middle plot also has the four corner plots added in it to demonstrate comparison of the extremes.

Statistical models thus have the background depositional fabric A, B or C generated with specific correlation lengths of threshold pressures in the horizontal and vertical directions, while the models derived from the peel have the depositional fabric of the respective real peel samples. We briefly explain the salient features of the techniques used in building high-resolution digital models of the peel samples in this section. Refer Meckel (2012, in review) for in-depth explanation of this technique. Next, we explain the input fields for the modified invasion percolation simulator and the full-physics finite difference simulator used in this study.

4.2 Data sampling technique for physical geologic samples: Steps involved in building the digital model

We present the salient features of the technique used to measure data from the physical peel sample using one peel specimen (peel # 1). The same technique can be similarly used for quantifying the characteristics of other such sedimentary samples.

Building the digital model of the peel involves the following four main steps (Figure 4-5):

a. Obtaining the relief peel sample by epoxy imbibition (imbibition with viscous fluid to sufficiently explore the range of variability in the sample properties);
b. Subjecting the peel specimen to high-resolution laser scanning and imaging techniques to study epoxy imbibition and grain size distribution;
c. Digital elevation map (DEM) derived from topographical variations measured on the peel;
d. Correlating the grain diameter and elevation measurements to threshold pressure values to generate the digital high-resolution model representing the sample.

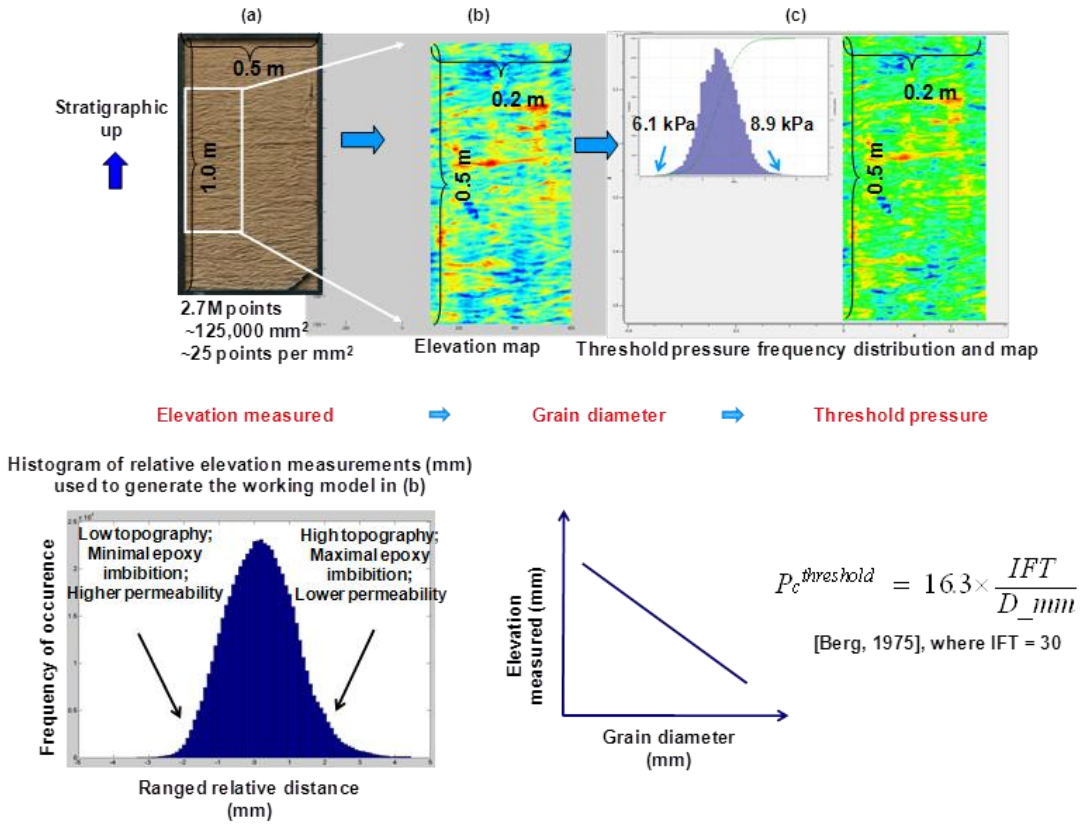

Figure 4-5: Summary of the geologic model. Optically ranged topography and grain diameter measurements on a 1 m by 0.5 m peel from a river alluvium are used to build high-resolution digital model populated with threshold pressure values. Sequential stages of building the digital model from the epoxy-imbibed geologic peel specimen we obtained are (Meckel, 2012 in review): (a) Peel specimen subjected to high-resolution laser scanning and imaging techniques to study epoxy imbibition and grain size distribution; (b) Digital elevation map derived from topographical variations in the peel due to epoxy imbibition; (c) Digital high-resolution model (>2 million cells) representing the threshold pressure distribution of the model domain generated from grain diameter measurements corresponding to determined topography.

4.2.1 Sample collection technique (peel # 1)

The quasi-2D vertically oriented sedimentary relief peel sample # 1 (~1.0 m × 0.5 m) broadly consists of cm-scale ripple-laminated well-sorted lower-fine to lower-very-fine sand. The sample collection technique involves saturating vertical exposures of unconsolidated sediment with viscous fluid that "penetrates the sample by capillary action" (McMullen and Allen, 1964). The rate and extent of penetration are a function of the viscosity of the imbibing liquid and the grain size distribution of the sample. Greater epoxy imbibition thus occurs in regions with smaller pore throats, and hence smaller permeability and larger threshold pressure. The greater extent of imbibitions leads to higher peaks in the topography of the peel surface. This motivates the measurement of elevation described next.

4.2.2 Measurements and statistics of the Digital Elevation Model (DEM)

We briefly explain the technique used to extract grain size and topology data from the epoxy-imbibed relief peel samples.

Grain size measurements for more than 2000 grains were obtained from a high dynamic range (HDR) digital microscope and further compared with elevations of the specimen. The distribution of grain sizes is shown in Figure 4-6. The maximum and minimum grain sizes measured were 0.08 and 0.055 mm.

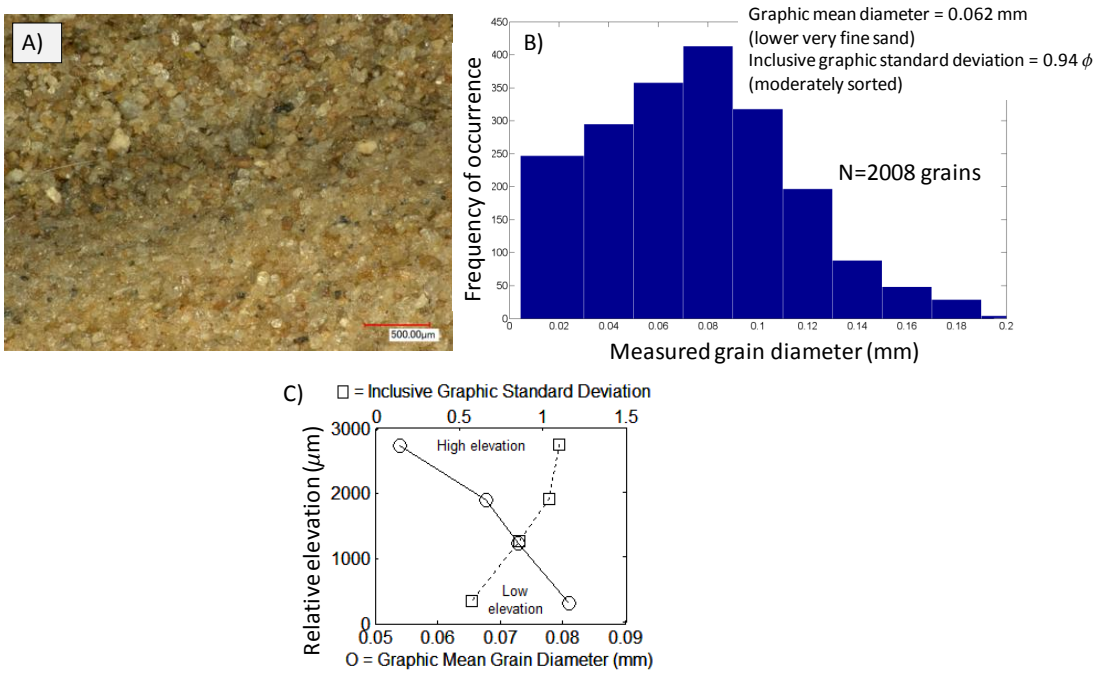

Figure 4-6: A) Distribution of peel grain-sizes observed using digital microscope. N = 2008; Graphic mean 0.062 mm, standard deviation 0.94 Ø. B) Histogram of the measured grain diameters for the 2008 grains in A). C) Graphic mean grain diameters and standard deviation for four elevation ranges from the working peel model. The trend is assumed to be linear for grain size changes with measured elevation.

Topographic relief of the peel was digitally scanned using a Suphaser 25 SP 3D laser scanner at the Texas Bureau of Economic Geology. The ranged distance (mm) between the scanner and the peel surface is obtained which provides the primary dataset to create a finely resolved digital elevation model (DEM) of the peel relief (Figure 4-5 panel (b)). The peel # 1 model sub-section we work with contains 1,767,398 ranged data points, representing ~14 range measurements per mm^2. The raw ranged measurements are linearly interpolated appropriately to provide regularly gridded representation of the peel specimen at native resolution such that we perform minimal interpolation and sample with enough data density at the same time.

We also evaluate the correlation length of threshold pressures in horizontal and vertical principal directions to quantify the anisotropy in the peel samples. For this purpose we run a MATLAB script to calculate the directional variograms for each of the representative peel sample sections. Figure 4-7 gives the variograms extracted for the peel samples.

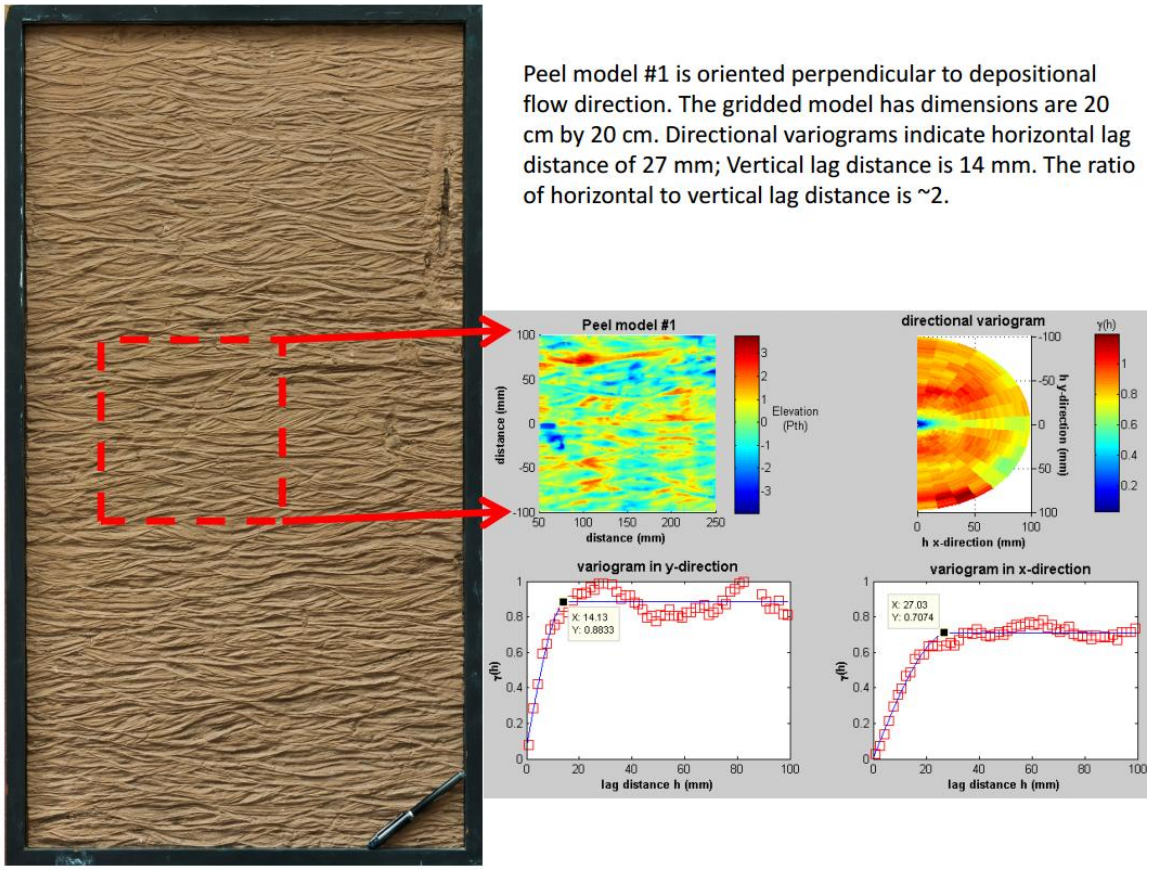

(A) Directional variograms for peel # 1. The gridded model of 20 cm × 20 cm is used to calculate the directional variograms as shown. The ratio of horizontal to vertical lag distance is 2 in this case.

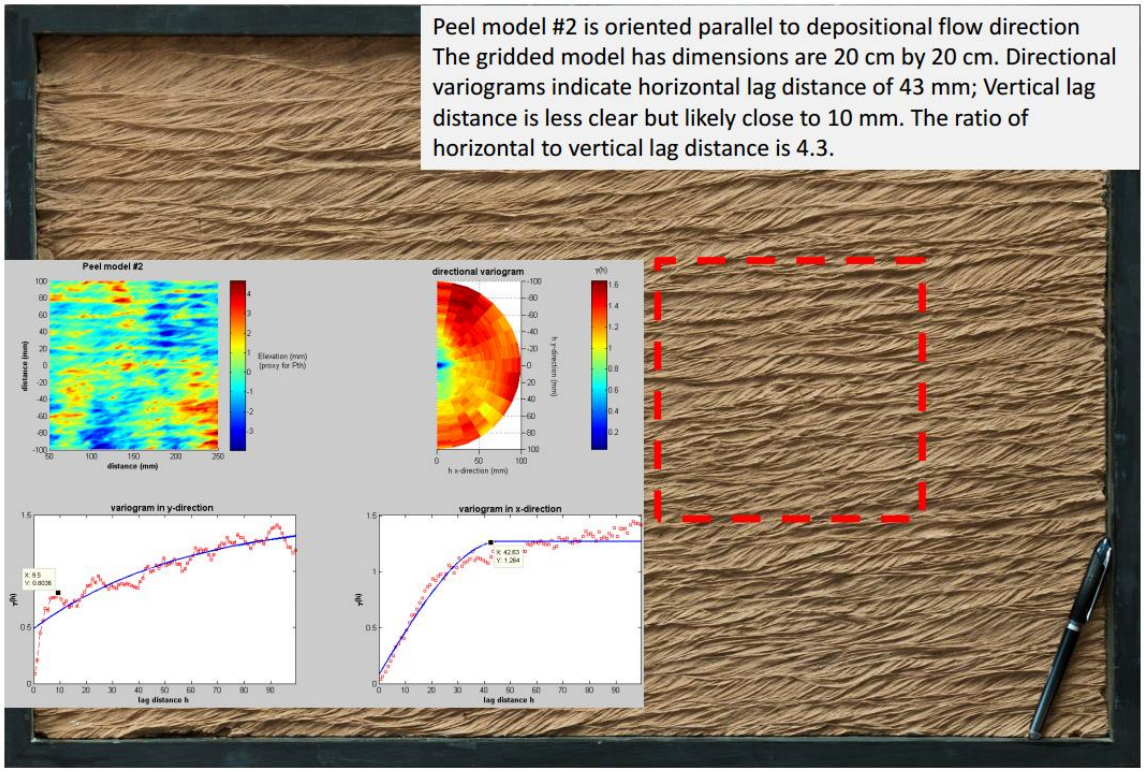

(B) Directional variograms for peel # 2. The gridded model of 20 cm × 20 cm is used to calculate the directional variograms as shown. The ratio of horizontal to vertical lag distance is a higher 4.3 in this case.

Figure 4-7: Geostatistical information on the two natural peel specimen to characterize their anisotropy. (A) and (B) give the directional variogram analysis performed for peels # 1 and # 2 respectively.

The anisotropy or the ratio of correlation length of threshold pressures in horizontal to vertical directions for peel # 1 is calculated to be 2 while that for the peel # 2 is 4.3.

4.2.3 Digital elevation model (DEM) of peel

Figure 4-8 gives the histogram of the elevation data measured on the peel samples.

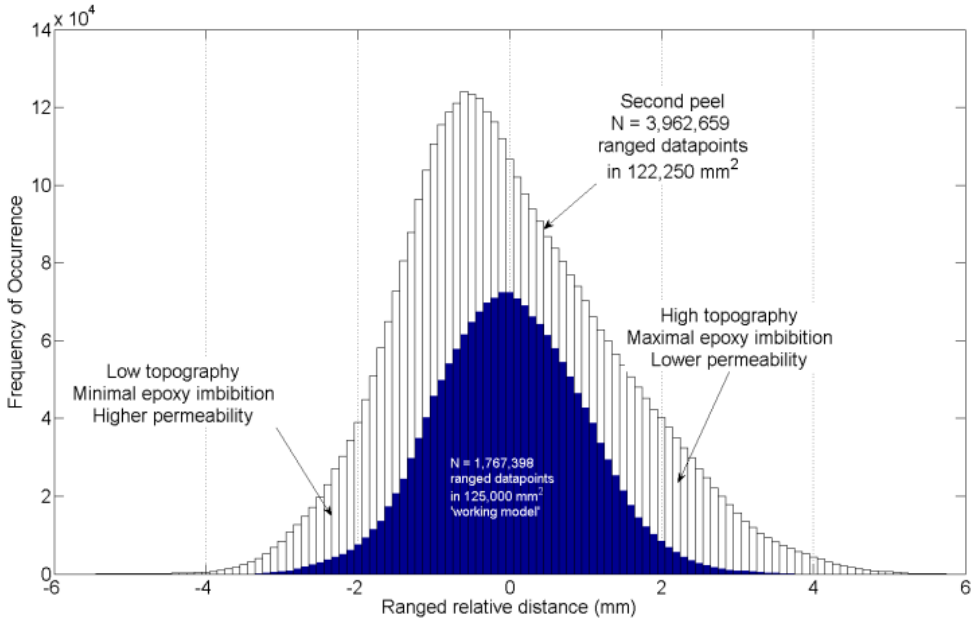

Figure 4-8: Histogram of the elevation data measured on the two peel samples. The elevations are measured with respect to a reference plane (ranged distance between the scanner and peel surface) and hence the topography has both positive and negative variations. The elevation values are observed to be normally-distributed for both the peel samples.

Statistical properties for this sample indicate that the elevation measurements are normally-distributed. Peel topography is documented to result from changes in mean grain diameter and standard deviation, so that the topography can be used as a proxy for spatially varying rock properties related to grain sizes. Due to the fine resolution of the data measurements our digital models would be highly resolved to depositional resolution. The high-resolution digital elevation map obtained through laser range scanning (Figure 4-5 panel (b)) and the direct grain size measurements indicates that peel topography is linearly correlated with variations in measured grain size (in mm) and sorting (Figure 4-6 panel C)). Thus higher elevations correspond with greater imbibitions as a result of smaller average grain size (hotter colors, Figure 4-5 panel (b)) and lower

elevations correspond with lesser imbibition as a result of larger average grain size (cooler colors, Figure 4-5 panel (b)).

4.2.4 Digital simulation model of peel from the DEM dataset

We use simplistic conversion of the highly-dense elevation data measurements into key petrophysical properties governing fluid migration in the medium. Peel topography is used to populate a threshold pressure continuum field for invasion percolation (IP) simulations. Observed grain size data from the peel can be used to determine a range (minimum, maximum) of P_{th} that are used as the extremes of the topography distribution and then mapped to elevation to create a lognormally distributed P_{th} field (Appendix A). (A normal distribution of grain sizes leads to a lognormal P_{th} distribution because P_{th} scales with the reciprocal of grain size). For synthetic domains, we assume normal distribution of threshold pressures throughout in this work. Maximum and minimum P_{th} values for the distribution are calculated from equation 3-2 to be 6.1 to 8.9 kPa, corresponding to maximum and minimum grain sizes of 0.08 and 0.055 mm and an interfacial tension of 30 mN/m (for CO_2- H_2O system).

The simulation model is thus a representation of the heterogeneity of the peel as shown by the correspondence between the DEM and the threshold pressure map in Figure 4-5 panel (b) and (c). Figure 4-5 panel (c) gives the threshold pressure map color coded with red shades implying regions of highest threshold pressure that correspond to highest elevations in the domain. For presentation of simulation results, the threshold pressure maps shows lighter gray shades in the grayscale domain background corresponding to high P_{th} (hotter colors in Figure 4-5 panel (c)) and the lower P_{th} values represented by the darker gray shades (cooler colors in Figure 4-5 panel (c)). Section 4.3 gives more details about model definition in the simulator.

The digital dataset used for sensitivity analysis (working model shown in Figure 4-9) is a representative subset of the peel # 1 specimen that is 0.4 m wide × 0.4 m tall with 2000 ×

2000 cells. The digital nature of the datasets from the obtained peels allows for modification of petrophysical properties while working with the fundamental depositional fabric. Hence we also investigate migration in domain with the depositional fabric of the peel #1 which is closer to reality than geostatistical models.

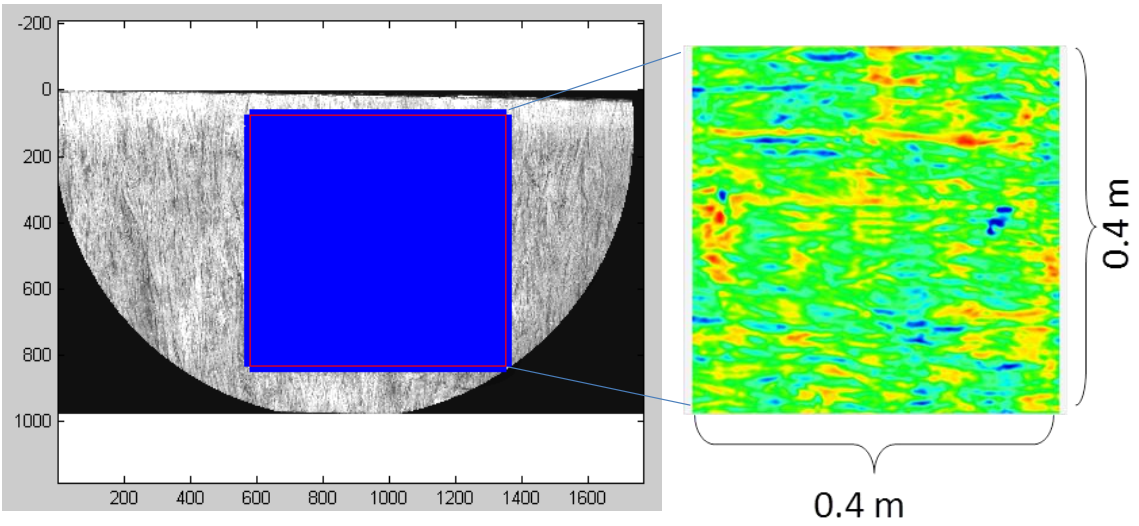

Figure 4-9: Working model of the peel with the threshold pressure map. The working model is a 0.4 m × 0.4 m section extracted from the peel with the model consisting of 2000 × 2000 cells. The background on left panel is a grayscale image of the peel subsection as seen through the high resolution 3D optical microscope. The blue box indicates the location we have sampled the working model from the peel # 1.

Also, we recognize the potential to generate database of different facies from real geological samples, on similar lines, to be incorporated as well-defined lithologies in various simulation scales.

4.3 Permedia® simulation models

4.3.1 Aquifer model initialization in Permedia®: simple FID-PAR models

We use Permedia®, a modified invasion percolation based simulator distributed by Halliburton, for investigating the rise of buoyant CO_2 through a heterogeneous domain as

a percolation process. Permedia's migration fluid-flow solvers are applicable for capillary-dominated drainage flow conditions. We use this tool to build our FID-PAR models (described below) and simulate Static Migration® in them. FID-PAR models are very simplistic and useful in studying fluid displacement patterns in heterogeneous media. The models show where the invading buoyant fluid is and how it got there. Options to visualize fluid saturation (presence of CO_2 in any cell), invasion time sequence etc. are available for the static migration models.

a) Volume editor tool: Defining FID properties

b) Descriptive statistics: Threshold pressure histogram

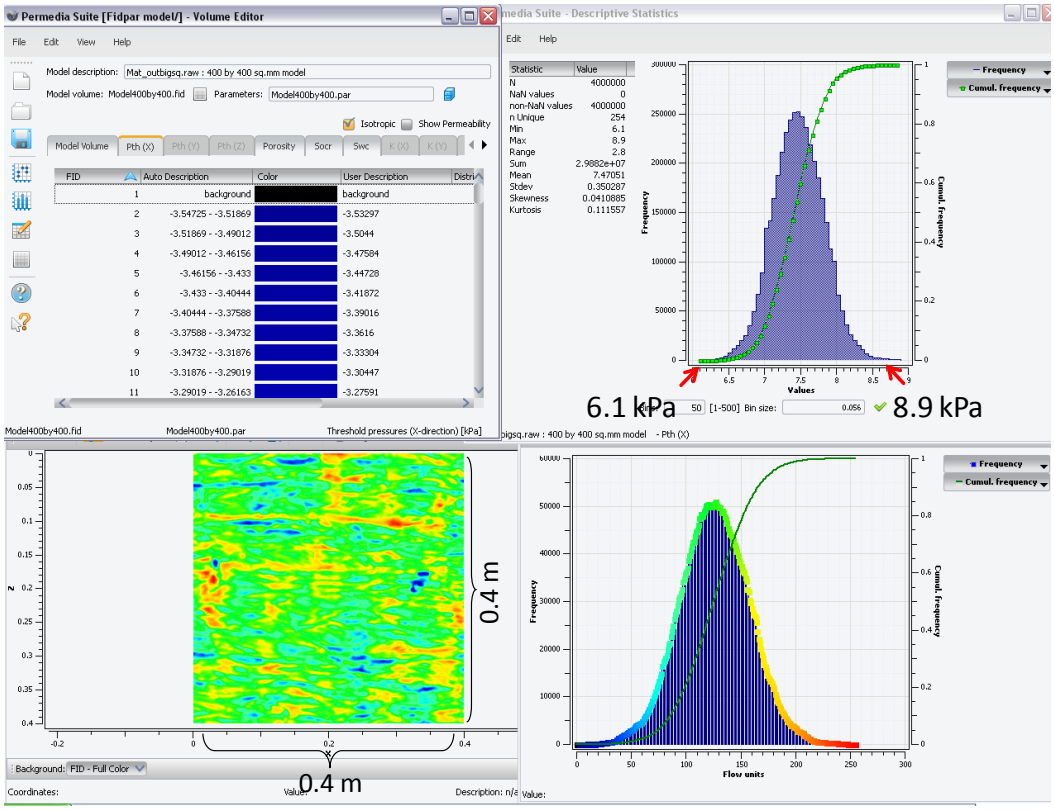

c) 2D viewer: Visualization of model domain

d) Descriptive statistics: FID histogram of model domain

Figure 4-10: Sample input FID-PAR file for the peel # 1. Panels give an illustration of the normal threshold pressure distribution in this medium. Panel a) is a snapshot of the Volume Editor tool in Permedia® used to define properties to the FIDs (Flow unit IDs).

Panel b) shows the histogram of the assigned threshold pressure values to the domain in panel c). The color scheme in Panel c) represents increasing threshold pressure values for cooler to hotter colors. The threshold pressure values for the peel are normally-distributed with a mean of 7.4 kPa per panel b). Panel d) gives the histogram of the FIDs in the model domain. The model has higher frequency of green FIDs (mid-range P_{th} values) as evident in panel c).

The FID-PAR models have a FID (Flow unit ID) assigned to each grid block or cell in the model. The petrophysical input parameters (PAR) namely threshold pressures, porosity, connate water saturation, residual oil saturation and permeability values (permeability values in X, Y and Z directions) are assigned to each FID in the model. The FID-PAR models we use to explore CO_2 migration patterns have the threshold pressure field as the input parameter characterizing the heterogeneity of the medium. The threshold pressure frequency distribution is taken to be normally-distributed for all our model simulations. To generate the threshold pressure field in the FID-PAR models, each FID is assigned a P_{th} distribution from which the threshold pressure for a simulation run is randomly chosen. A random seed generator value decides the P_{th} that is assigned to each FID during each simulation run. We specify the mean and standard deviation of for each FID in the model. These values are assigned in linearly increasing order for coolest to hottest FID colors. The mean for the least FID (darkest blue) is set to the minimum P_{th} (6.1 kPa for peel # 1) and the mean for the largest FID (darkest red) is set to the maximum P_{th} (8.9 kPa for peel # 1). A standard deviation of zero yields a discrete value of P_{th} for that FID. The simulations in this study use a standard deviation of 0. The remaining P_{th} values for the other FIDs are obtained by linear interpolation between the minimum and maximum P_{th} values. Typical simulations use 255 FIDs.

The porosity, connate water and critical oil saturations are assigned arbitrary constant values in our simulations. The threshold pressure field is the critical input parameter

influencing invasion patterns of CO_2 in the capillary channel regime. Table 4-2 gives the values for the peel # 1 simulation in this study.

Parameter	**Value**
Threshold pressure	6.1-8.9 kPa; normal distribution of values with mean = 7.4 kPa and standard devation = 0.4 kPa
Porosity	20%
Connate water saturation, S_{wc}	20%
Critical oil saturation, S_{ocr}	2%
Flow boundary conditions	CLOSED / PERIODIC lateral flow boundaries
Depth from datum	1615.44 m
Density difference between CO_2 and brine	300 kg/m^3
Interfacial tension, IFT multiplier*	0.065

Table 4-2: Input properties for the peel # 1 model in Permedia®. This model is used to explore capillary channel flow regime of CO_2.

*IFT multiplier stands for interfacial tension scaling factor. In Permedia, P_{th} values are specified as Mercury-Air P_{th} values and then scaled by Permedia to the relevant fluid system (e.g. CO_2-H_2O system). All P_{th} values in the domain are multiplied by this value.

Now that we have defined the digital model for simulation we need to specify the simulation criteria and boundary conditions based on the physical scenario. The nature of the source of CO_2, the time steps for migration and the scale of the models have much physical significance attached to them. We justify the values we use in this work in the following sub-sections:

4.3.2 Sourcing for percolation models

The geometric nature of the CO_2 source that comes into contact with the rock section of interest has a significant bearing on the characteristics of the migration pathway to percolation. Various stages of plume migration in the reservoir can be represented in simulation models using different source geometry. Compact plume at the transition of viscous flow regime to the buoyancy-driven flow regime is fairly represented in 2-D as a line source. Once CO_2 migration is dominated by buoyancy forces, single-point to multiple point sources spanning the width of the domain represent the plume contacting the rock section of interest. Figure 4-11 illustrates a sample comparison case between the limiting cases of single-point source and line source using the 0.4 m × 0.4 m peel # 1 model. Panel (a) in Figure 4-11 represents the migration pathways when a line source of CO_2 was set at the bottom of the domain. Panels (b) and (c) in Figure 4-11 represent point source simulations for two arbitrary choices of the point location along the bottom edge of the domain. Panel (b) has the point source located at cell (400, 1999) while panel (c) has the source located at the cell (1700, 1999). All the simulations are run to percolation with periodic lateral flow boundaries. Percolation is said to occur once the fluid traverses the height of the domain to reach its top boundary.

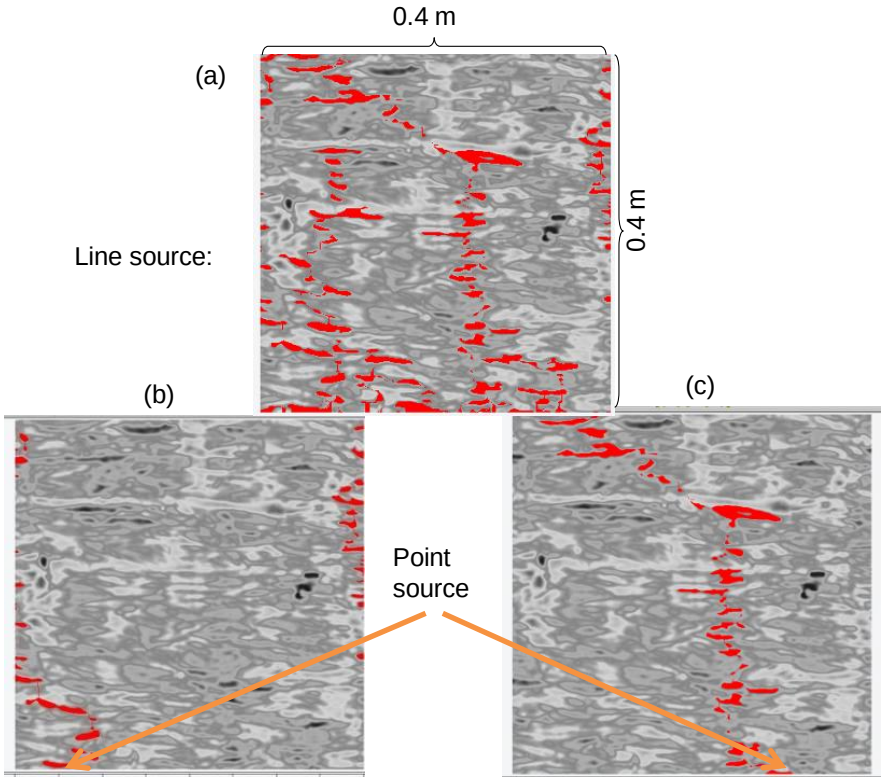

Figure 4-11: Illustration of a sample comparison between line source and point source of CO_2 being introduced into the peel domain. All the simulations are run to percolation, i.e. till the fluid spans the entire height of the domain to just reach its top boundary, with periodic lateral flow boundaries. The point source simulations show migration in subsets of the saturation pathways that occur in the line source scenario. Hence the line source scenario gives an upper bound on the percentage of the domain invaded by CO_2 at percolation. The model domain used is a 0.4 m × 0.4 m sub-section of peel # 1.

We perform the exercise of moving the point source of CO_2 at regular cell intervals (point source simulations at every 100 cells from (100, 1999) to (1900, 1999)) scanning the peel model domain. Figure 4-11 shows the result for two of these point sources. All the various point source simulations result in subsets of the saturation pathways that occur in the line source scenario.

The major saturation pathways that branch in the line source scenario for the peel all proceed to percolate to the top boundary, some slower than the others. This is observed in the simulation where a copy of the peel model is placed at the top edge of the original peel model. There is, however, a path of least resistance to percolate through the domain which CO_2 prefers and this is the pathway we observe at percolation. A histogram of the percentage invasion values of the domain by CO_2 at percolation is given in Figure 4-12.

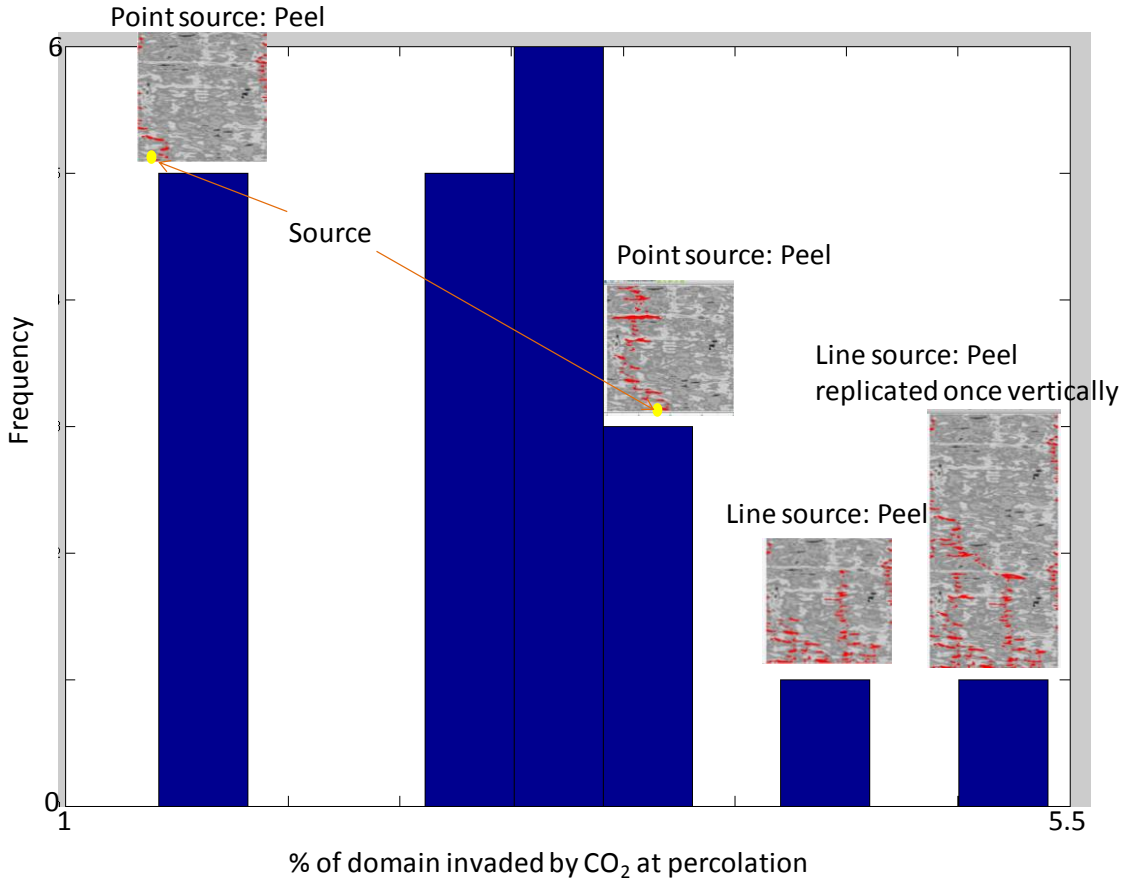

Figure 4-12: Histogram of percentage invasion of domain by CO_2 for all the different point sources and line source simulations. The line source simulation gives an optimistic value for the percentage of the domain invaded by CO_2 at percolation. Insets illustrate sample invasion patterns for simulations with corresponding % invasion values. The peel replicated once vertically (i.e. copy of the peel model is placed at the top edge of the

original peel model) gives complete invasion patterns where all the characteristic saturation pathways percolate through the first individual peel section. The invasion patterns for different point source simulations turn out to be subsets of this limiting case percolation scenario.

This histogram is a compilation of all the point source simulations along with the line source simulation. Depending on the location of the point source, different migration pathways become characteristic paths of least resistance that span the domain. We clearly see that the line source scenario gives an upper bound (sum of all pathways in point source cases) of the percentage of the domain invaded by CO_2 at percolation. Hence we source CO_2 as a line from the bottom of the domain in our simulations.

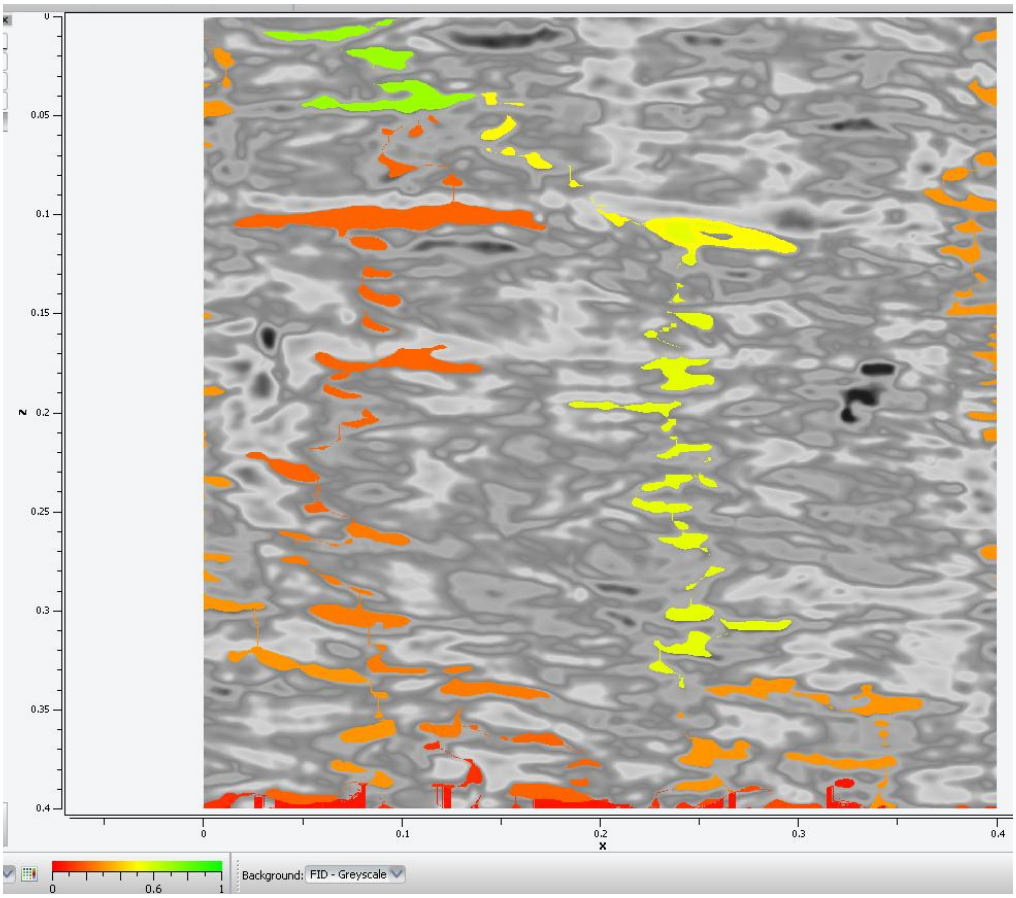

Figure 4-13: Probabilistic analysis of CO_2 presence in the model domain. This analysis is performed on the set of 20 point source simulations at different points in the bottom row

of the domain and a line source simulation. The color scale shown at the bottom left is from 0 to 1 for probability of CO_2 presence in any cell in this model domain. The background is the threshold pressure distribution map of the peel # 1. The model domain used is a 0.4 m × 0.4 m sub-section of peel # 1.

The results can also be compiled by overlaying all the simulations to find the probability that a particular cell in the model domain sees CO_2 in any simulation. We make use of the Risk analysis tool in Permedia® to explore for the probability that any particular cell in the model domain would see the presence of CO_2 during migration. Figure 4-13 gives the results of such probabilistic analysis on the peel # 1 sample. The areas in cooler colors indicate higher probability of the presence of CO_2 in the model domain. This means that once CO_2 traverses the bottom quarter portion of the model domain, there is a higher probability that the yellow/ green pathways would prevail leading to percolation.

4.3.3 Temporal evolution of CO_2 saturation in the domain

CO_2 percolates through the medium following a characteristic path of least resistance to percolation depending on the nature and location of the source. We observe that any CO_2 being further sourced into the medium would, almost always, continue along this already pre-established path of least resistance rather than venture into new migration paths. This section explains our choice of time step to present our IP model simulations.

For this purpose we perform simulation runs of capillary channel flow in a set of models M11 through M18 with progressively increasing heterogeneity of the domain. All models M11 through M18 have the sedimentologic fabric from the 0.4 m × 0.4 m (2000 cells wide × 2000 cells tall) peel # 1 section with different threshold pressure distributions assigned to them. The density difference between CO_2 and connate water is 300 kg/m^3. The background depositional fabric and the fluid properties for these models are the same with only the range of threshold pressure varying in each model. The $<P_{th}>$ for all the models is held constant at 7.4 kPa (determined from peel # 1) while the σ_{Pth} is increased

from M11 through M18 as 0.01 kPa to 1.4 kPa. M11 is the most homogeneous domain (narrowest threshold pressure distribution) and the heterogeneity increases with M18 being the most heterogeneous domain (widest threshold pressure distribution). Table 4-3 gives the input parameters for all models. The threshold pressure distributions of the various models are given in Figure 4-14 below.

Parameter	**Value**
Threshold pressure	Normal distribution of values from Figure 4-15
Porosity	20%
Connate water saturation, S_{wc}	20%
Critical oil saturation, S_{ocr}	2%
Flow boundary conditions	PERIODIC lateral flow boundaries
Depth from datum	1615.44 m
Density difference between CO_2 and brine	300 kg/m^3
Interfacial tension, IFT multiplier	0.065

Table 4-3: Input properties for the models M11 through M18 in Permedia®. These domains have the depositional fabric of peel # 1. The threshold pressure distributions are varied in each model thus varying its degree of heterogeneity.

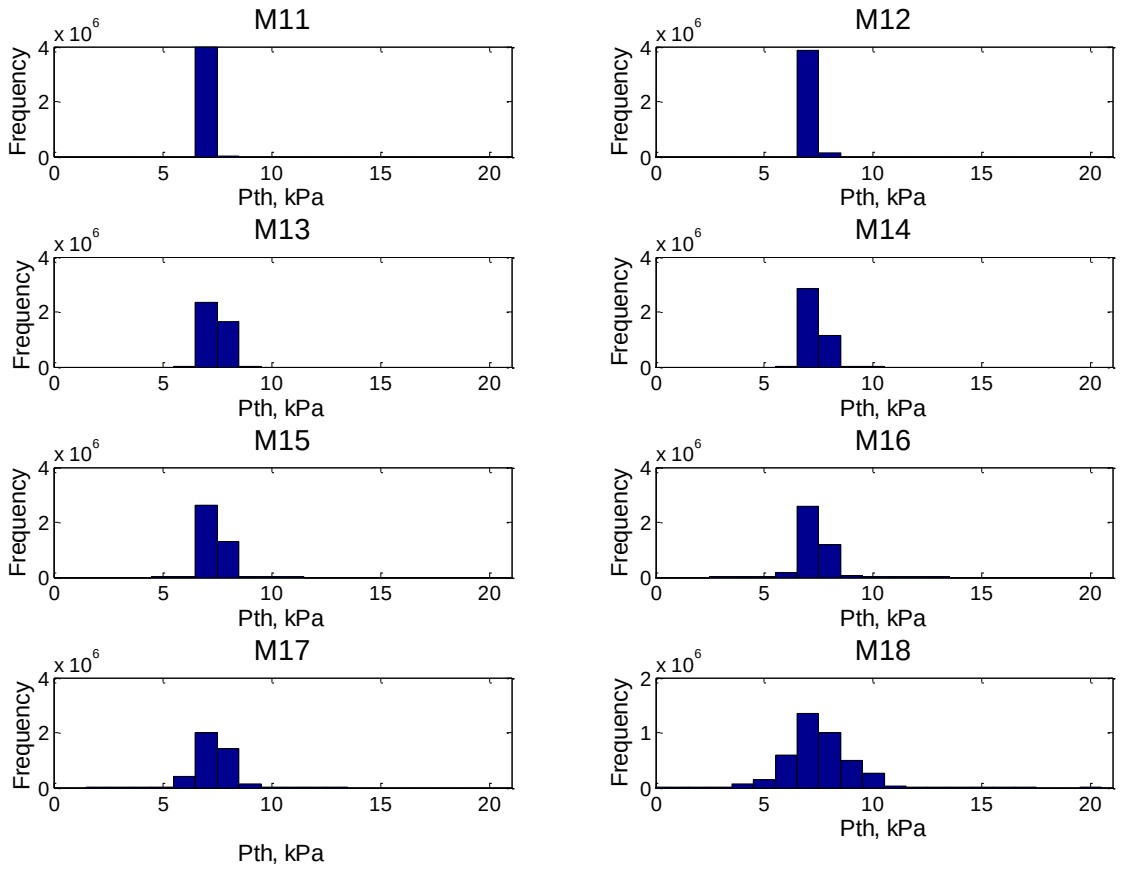

Figure 4-14: Threshold pressure distribution of models M11 to M18. The depositional fabric in these models is that of peel # 1.

For a line source of CO_2 in these model domains with periodic X-boundaries, we study displacement patterns at various time steps until CO_2 percolates to the top boundary of the domain. Figure 4-15 illustrates the time sequence plot for one line source simulation on the peel # 1.

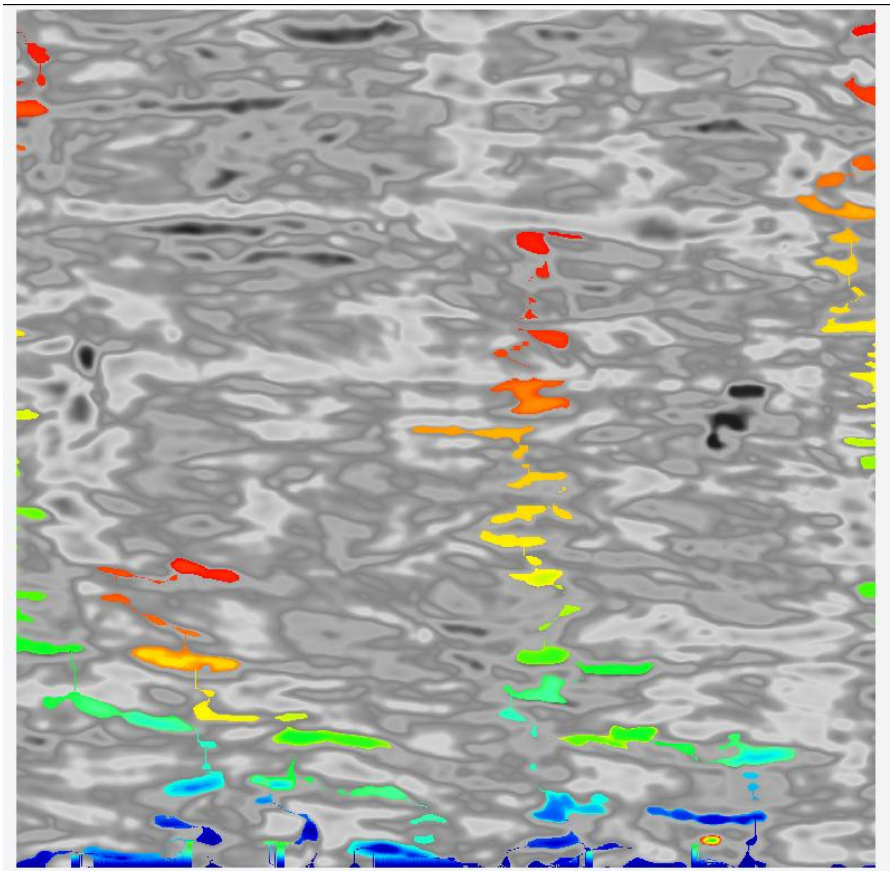

Figure 4-15: Time sequence plot for model M12. The color scheme from cooler colors to the hotter colors represent increasing time steps (earlier to later time). Some paths progress faster to the top boundary than others. Given enough time, all the paths that start out ultimately percolate to the top. Model M12 is 0.4 m × 0.4 m (2000 cells wide × 2000 cells tall) with the depositional fabric of peel # 1. CO_2 is sourced into the source cells at every time step until it can no longer move into any new cell. More CO_2 is sourced in the next time step to build capillary pressure and migrate through the domain. This process repeats until percolation. The time steps in these percolation models thus have arbitrary units.

We can see from Figure 4-15 that some paths progress faster to the top boundary of the model domain than others. Given enough time to migrate, all the major saturation pathways ultimately percolate through to the top of the domain. The D-metric is

calculated for each of the eight domains (rocks M11 to M18) at various time steps from the initial sourcing till when CO_2 percolates to the top boundary of the domains. The time-varying behavior of the D-metric is plotted in Figure 4-16.

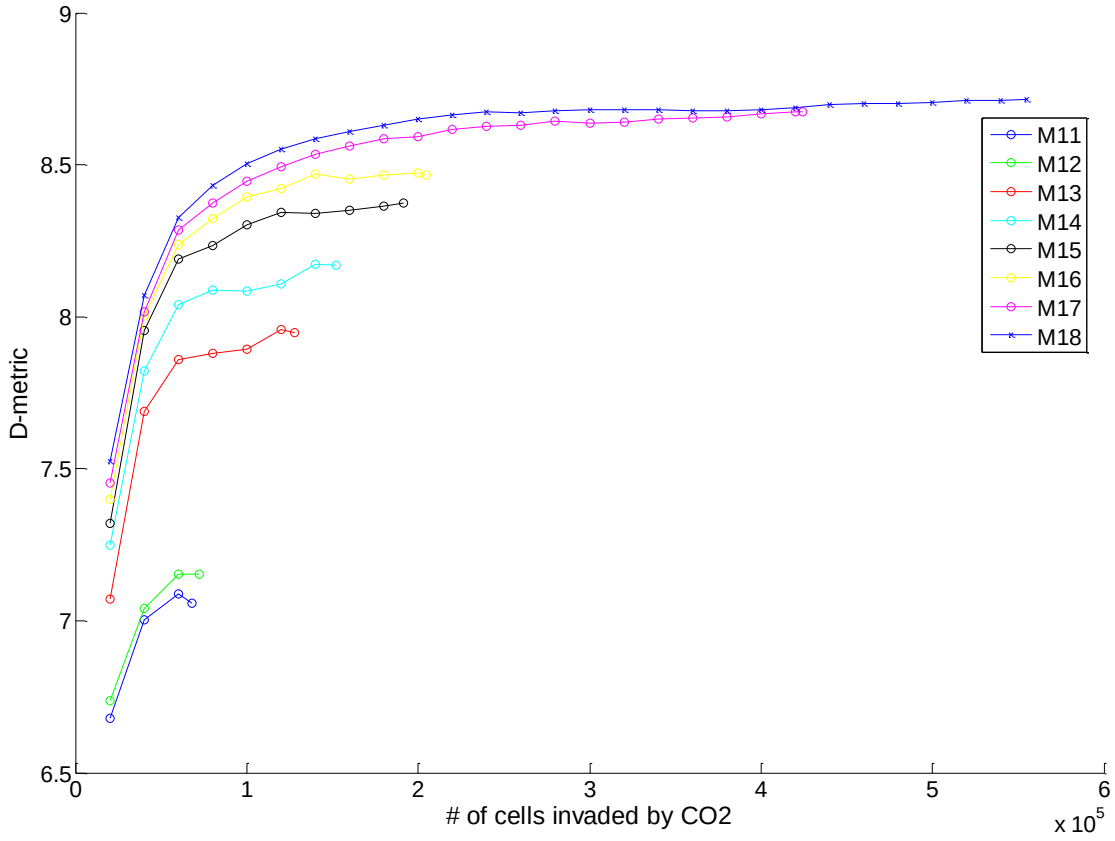

Figure 4-16: Evolution of the time varying behavior of D-metric for models of varying heterogeneity until percolation. Models M11 through M18 represent rocks with increasing heterogeneity. More homogeneous rocks attain equilibrium values of D-metric earlier and yield sparser saturation distributions in the domain as shown by the lower values of the D-metric. As heterogeneity increases, the saturation distribution becomes more compact with higher values of the D-metric and we observe equilibrium values of the D-metric being attained at later time steps in the simulations. All models attain equilibrium values of the D-metric at percolation.

Figure 4-16 shows how the D-metric increases as % cells filled increases until it reaches a stable D value for any simulation. Hence the representative D-metric for a given simulation would be this stable value. We pick the time step when percolation occurs because this case always occurs at the stable D-metric values. The migration patterns described for various scenarios in this work are thus at the special temporal case of percolation for all simulation results.

4.3.4 Small-scale models to realistic larger-scale migration behavior

We simulate capillary channel flow in small-scale models (meter-scale) in this work. The ease of simulating on representative smaller sub-sections of a large high-resolution domain reflects savings on computational effort and time. However, we must ensure that we do not lose out on the essential dynamics when we scale-down the rock section. We perform this exercise to illustrate the effect of model size on capillary channels of CO_2.

Figure 4-17 shows the models used for this exercise. The smaller model sections of 0.3 m $\times$ 0.1 m, 0.2 m $\times$ 0.1 m and 0.1 m $\times$ 0.1 m are sub-sampled from the model with the peel # 1 depositional fabric. The orange rectangular box in each model indicates the sampled section of each model to its right (Figure 4-17). Each model, at the same depositional resolution, is sourced with a line source of CO_2 into the domain with periodic lateral flow boundaries.

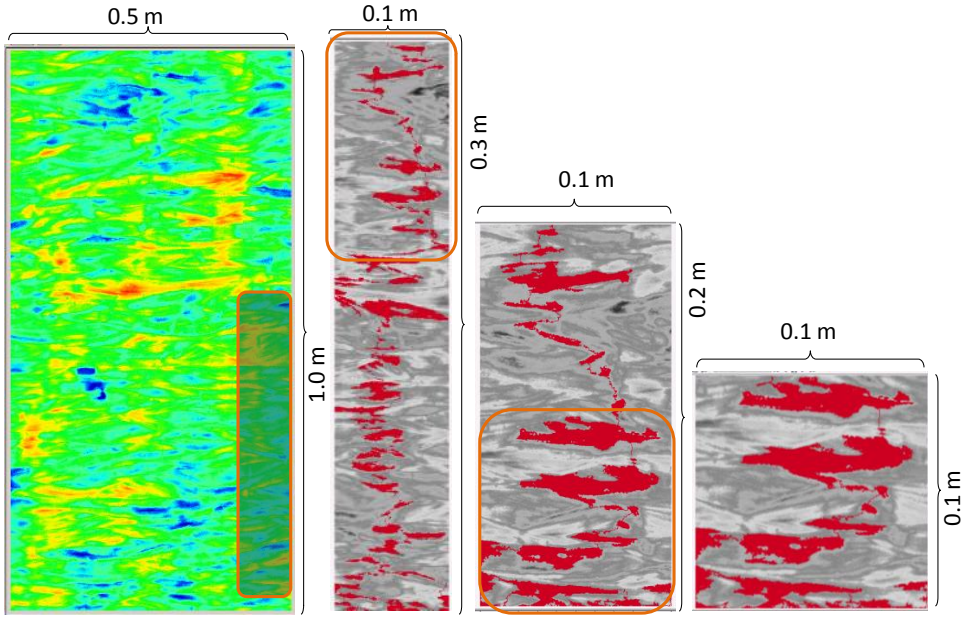

Figure 4-17: Comparison of migration patterns in peel model sections of varying dimensions. Leftmost model is the complete peel # 1. Sub-sections of the peel that are zoomed-in are indicated in the orange rectangular region. Threshold pressure distribution is considered to be 0.01- 20 kPa here.

We assign P_{th} distributions of four arbitrarily chosen models M11, M13, M16 and M18 on the three model domains extracted in Figure 4-17. Figure 4-18 is a plot of the percentage of the model invaded by CO_2 at percolation for the three different size subdomains with several distributions of threshold pressure.

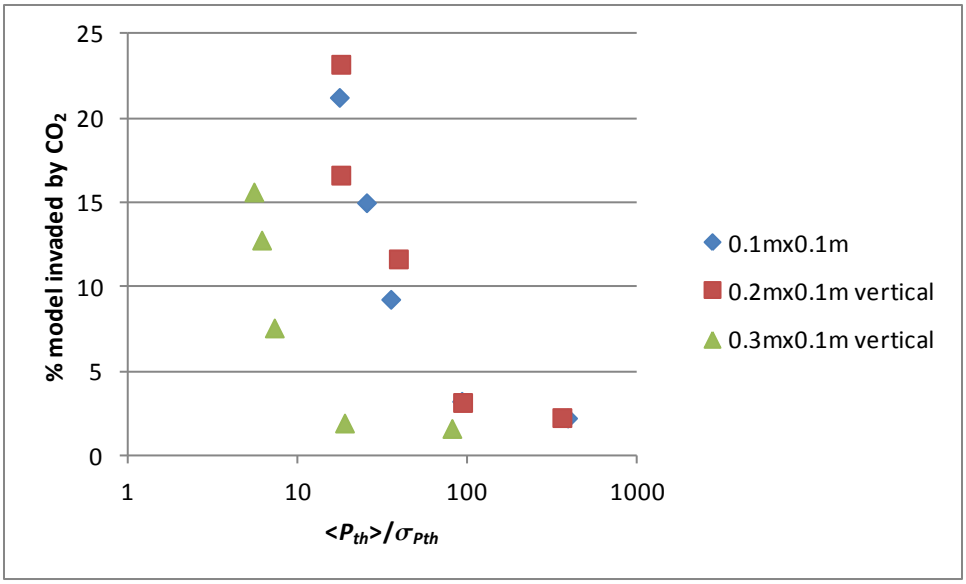

Figure 4-18: Various model sections of the peel fabric with different threshold pressure ranges compared for the % model invaded by CO_2 at percolation.

Fingering flow patterns dominate very homogeneous domains while back-filling structures take over as the heterogeneity of the domain increases (lower $<Pth>/\sigma_{Pth}$). The migration pathway followed (style of filling) remains the same (Figure 4-17) for different size subdomains for a given value of dimensionless threshold pressure. The model size we sample, however affects the actual percentage invasion values due to the difference in the total number of cells in the domains.

If the domain consists of layers of different depositional facies, the location of CO_2 source/ supply in the different facies affects the migration paths. Figure 4-19 gives an example domain we create by superimposing geostatistical model fabrics (B) and (C) to visualize CO_2 capillary invasion patterns.

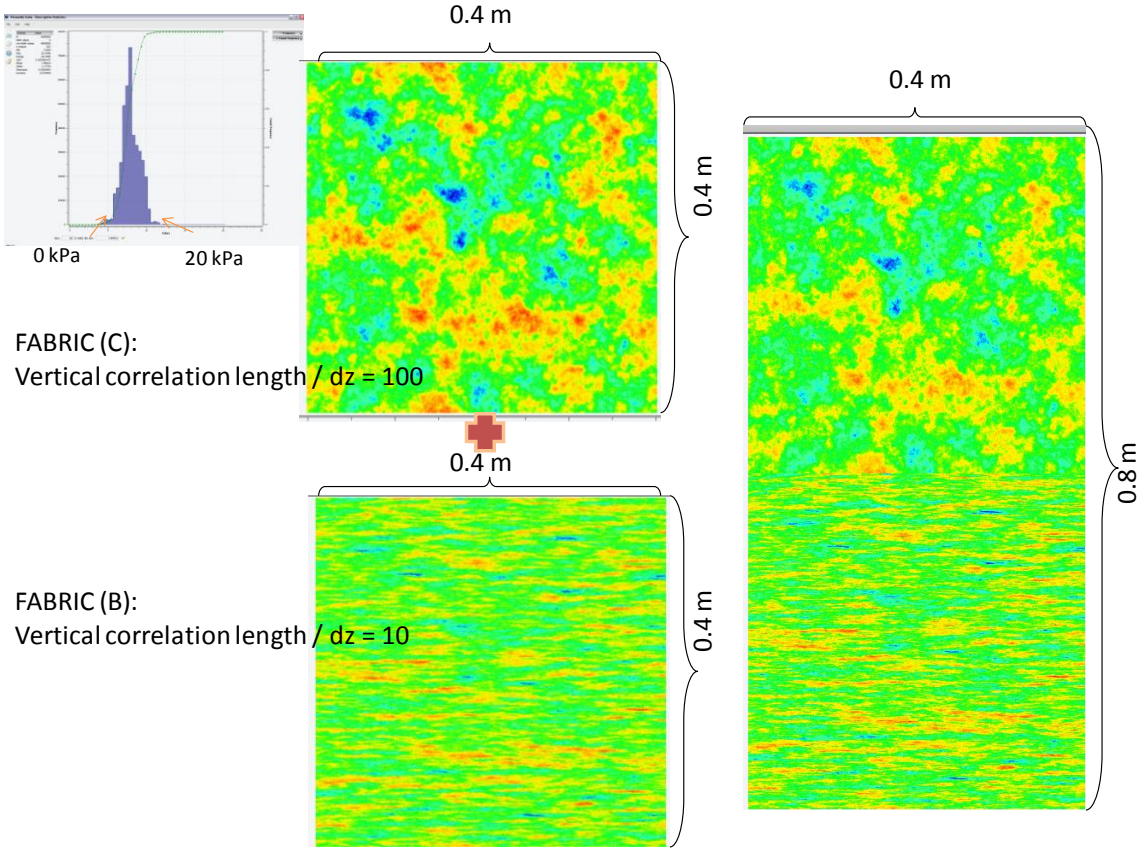

Figure 4-19: Heterogeneous model generated by joining two geostatistical models i.e. fabrics (B) and (C). Threshold pressure range of 0.01-20 kPa is used.

0.4 m × 0.4 m model with Fabric (C) is superimposed vertically on the top edge of a 0.4 m × 0.4 m model with Fabric (B) to give the combined model as shown in Figure 4-19. The invasion patterns for a line source of CO_2 at the bottom of the combined model (Figure 4-19) is shown in Figure 4-20. We see that CO_2 enters the upper half of the domain (facies with fabric (C)) only from single or a few points/ cells. The migration path that CO_2 follows in the upper stacked domains would thus be characteristic of that specific source location (section 4.3.2).

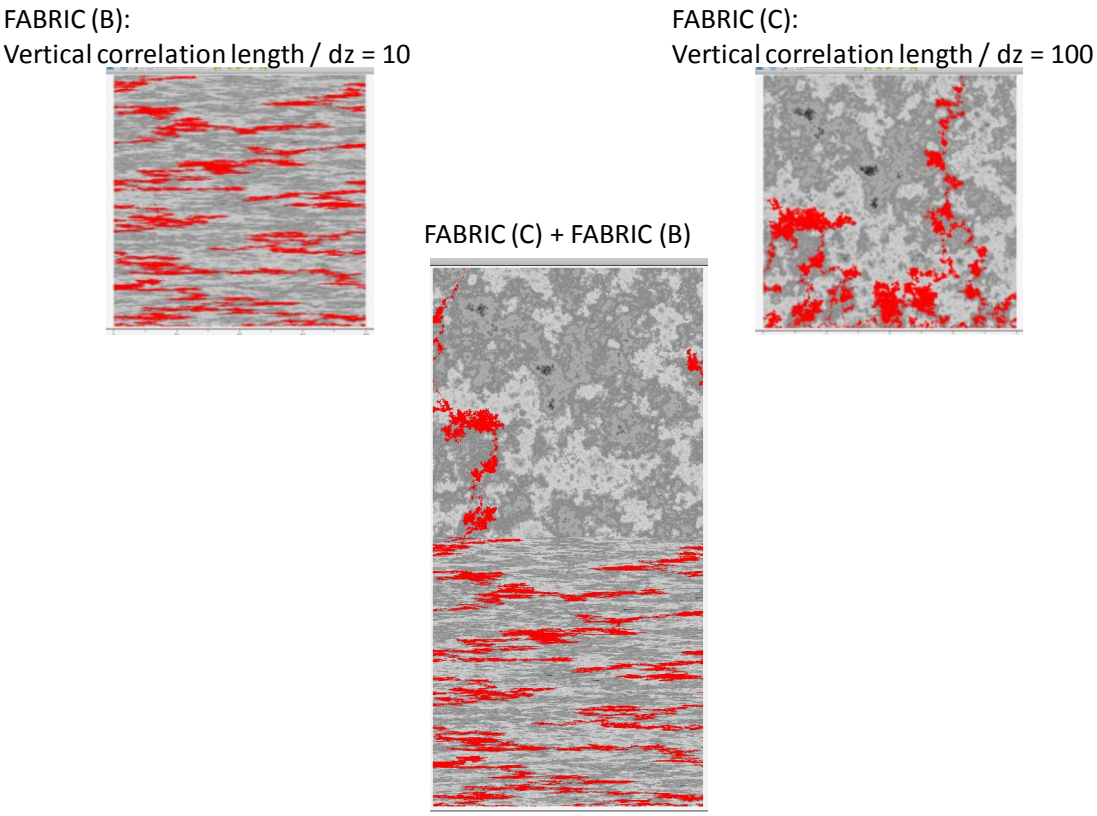

Figure 4-20: Migration pathways for line source in models generated by superimposing two geostatistical models i.e. fabrics (B) and (C). Source geometry affects the migration pathways followed by CO_2. Individual simulations of line source in Fabrics (B) and (C) are shown at the top of the figure. The simulation in the combined model appears in the center of the figure with a line source of CO_2 at the bottom of the model.

The flow patterns in Figure 4-20 suggest that the upper stacked domains/ facies would see only a single point source or a very narrow multiple point source but not the limiting case of CO_2 line source. The path of least resistance makes it first to percolation and proceeds into the above-lying facies/ rock. The migration pathway in Fabric (C) in the combined model illustrates this.

4.4 Full physics simulation models in GEM®

Our comparison studies are based on simulations performed with CMG's (Computer Modeling Group) simulator GEM (General Equation of state Model). GEM is a robust, general equation of state based compositional reservoir simulator. It accounts for the full physics of buoyancy driven two-phase flow and displacement.

We build the aquifer model and set the fluid properties as described by in Saadatpoor (2009). Saadatpoor (2009) studied the fractal behavior of buoyant CO_2 inside 2-D and 3-D heterogeneous aquifer models. We adopt similar strategy to explore the two-phase (aqueous and gas), two-component (CO_2 and brine) system in our models which have entry pressure fields identical to those used in the Permedia simulation models.

4.4.1 Aquifer model initialization: Getting input field from Permedia to GEM

The GEM model represents the line source of CO_2 in the Permedia models as a large CO_2 saturation in the bottom layers of the 2-D aquifer model. The boundaries of the domain are closed (no-flow boundaries) for the models used in the comparison cases. A drainage capillary pressure curve is assigned to each grid block in the GEM model; the capillary entry pressure for the drainage curve is the same as the threshold pressure in the Permedia model. The model scheme and other correlations for the input parameters is borrowed from Saadatpoor (2009). The permeability and porosity fields for the model domains are calculated from the threshold pressure values using correlations from Saadatpoor (2009). The Peng-Robinson equation of state was fitted to data for CO_2-brine system by Kumar *et al.* (2004). The authors tuned the Peng Robinson EOS (Equation of State) using experimental data for the critical properties and interaction coefficients of the components in aquifer conditions.

The models used in the comparison cases are 400 cells wide × 100 cells tall chosen for ease of computational effort involved. The aquifer in this series of simulations is assumed to be located 1615.4 m (5299.9 ft) below the surface, with an initial pressure of 2265.2 psi (15617 kPa) and temperature of 60 ^{o}C (140 ^{o}F) which are typical of deep saline aquifers.

4.4.2 Sourcing in GEM models

There are two ways to build the large initial CO_2 saturation in the GEM model equivalent to the line source used in Permedia simulations.

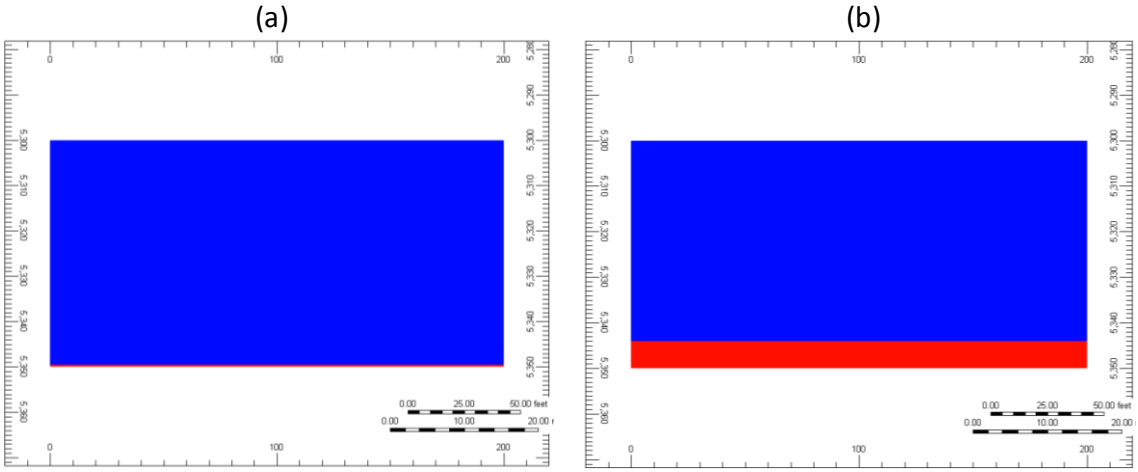

Figure 4-21: Initial condition for GEM simulations for two sourcing options. Panel (a) illustrates the use of 'volmod' option while panel (b) gives the option where a several layers of large CO_2 saturation at the bottom of the domain acts as the source. The model in this illustration is a heterogeneous domain 400 cells wide × 100 cells tall with each grid block being 0.1524 m × 0.1524 m (0.5 ft × 0.5 ft). The cells in red indicate the source cells in GEM.

Large saturation initial block of CO_2 option (Saadatpoor, 2009): A large initial saturation of CO_2 is emplaced at the bottom of the aquifer. The bottom-most row of the aquifer is the top-most part of this saturation block. This mimics the line source of CO_2 at the bottom edge of the domain in the Permedia simulations. Homogeneous layers containing CO_2 are added to supply a mass of CO_2 equal to the amount that enters the domain in the Permedia simulations. These CO_2 layers have the permeability and porosity equal to the average permeability and porosity of the aquifer itself.

VOLMOD option: Pore volumes in GEM are calculated based on the bulk volume of the reservoir rock and the porosity. Pore volume multipliers associate arbitrary volumes with grid blocks in the reservoir without affecting their physical dimensions. Hence a pore volume modifier of 2 would imply that the same grid cell now has an equivalent pore volume twice the base cell value but occupies the same physical volume as the single base cell. We use the keyword VOLMOD in GEM to input an array of pore volume modifiers on the source blocks to represent a large initial plume of CO_2 situation beneath the domain of interest. This option modifies the pore volume of the cells in the bottom-most row of the aquifer model for an equivalent line source. This method thus enables us to source volumes of CO_2 equivalent to the amount that enters the domain in Permedia simulations.

4.4.3 GEM model inputs: Incorporating heterogeneity in threshold pressures

In reality, every representative elementary volume of rock would have a different capillary entry pressure and hence our simulation model must also take into account this heterogeneity. The heterogeneity of the medium in Permedia is represented by the threshold pressure value assigned to each FID. We borrow the capillary pressure scaling concept from Saadatpoor *et al.* (2009). Saadatpoor *et al.* (2009) incorporated this concept in the full-physics models by using the Leverett J-function scaling to scale the capillary entry pressure for each grid cell in the heterogeneous domain. In GEM, the keyword *PCGMAX is used to scale the gas-liquid capillary pressure table to a different end point value and hence introduces the scaling coefficient for each grid cell with respect to the reference capillary pressure curve. Hence the input threshold pressure continuum of the Permedia model is extracted and normalized into the scaling factor (*PCGMAX input file) for the GEM model.

Once the models are built with all the appropriate input parameters according to the simulator, the simulation begins and buoyancy drives the migration of CO_2 within this aquifer.

5) RESULTS AND DISCUSSION

Sensitivity studies are carried out to analyze the effect of fluid density contrasts and the threshold pressure distribution (varying mean and standard deviation of threshold pressure distributions) in rocks with different sedimentologic fabrics. The depositional fabrics (correlation length of threshold pressures in the horizontal and vertical directions) we consider are the natural depositional fabric of the peel # 1 and the geostatistical model fabrics (A), (B) and (C) described in Chapter 4. We use threshold pressure distribution motivated from considering unconsolidated sand samples in Chapter 4 and density contrasts between CO_2 and native brine from the Atlas of Gulf of Mexico Gas and Oil Sands. We compare migration patterns in a couple of well-defined real geologic specimens with the understanding gained from behavior in generic porous media (geostatistical models). Finally, we verify the applicability of the invasion percolation simulator to study capillary channel flow physics by comparison with a full-physics simulator.

5.1 Sensitivity studies on capillary channels in heterogeneous media

We choose to work with a random 0.4 m × 0.4 m representative subsection (2000 × 2000 cells) from the peel # 1 model (Figure 4-9) to resolve CO_2 migration patterns at native depositional resolution. We also perform analogous studies on the geostatistical models with well-defined depositional fabric, introduced in the earlier chapter (Figure 4-1 fabrics (A), (B) and (C)).

5.1.1 Effect of fluid densities on capillary channels

As the CO_2 migrates through different depths in the reservoir, we expect density changes to occur. In this section we explore the effect of increasing buoyancy forces due to density difference variations during the process of migration. For domain resolution of 4,000,000 cells on the 0.4 m × 0.4 m peel # 1 sub-section (Figure 4-9) having threshold pressure distribution of 6.1 – 8.9 kPa ($<P_{th}>$=7.4 kPa; values correspond to entry

pressures estimated via Berg's equation for samples having median grain sizes corresponding to the minimum, maximum and mean grain sizes in the peel, respectively), we simulate the effect of increasing density difference between CO_2 and native brine from 300 to 950 kg/m^3 (Figure 5-1).

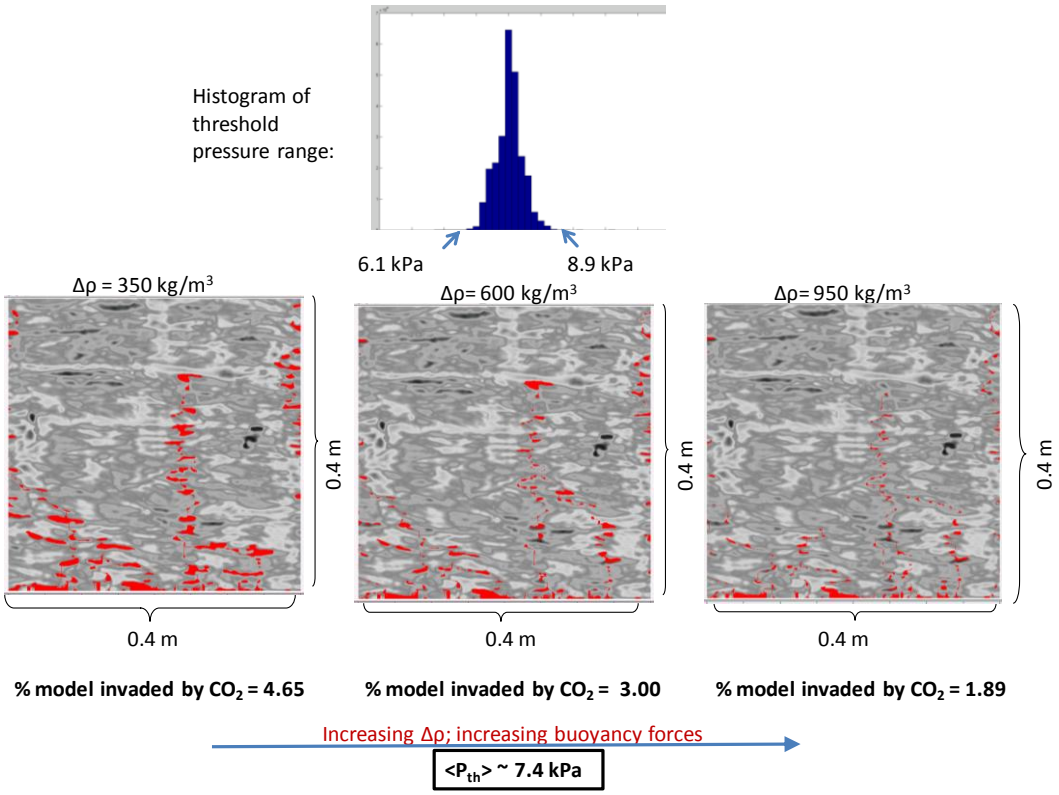

Figure 5-1: Flow transition from back-filling to fingering patterns occurs with increasing density difference between the CO_2 and native brine. Threshold pressure range of 6.1-8.9 kPa with $<P_{th}>$ of 7.4 kPa is used for all model simulations. The depositional fabric is taken from the peel #1 working subdomain. Cell dimensions in the model are 2 mm × 2 mm. The domain is thus 2000 cells wide × 2000 cells tall (i.e. 0.4 m ×0.4 m).

Plot of percentage of the domain invaded by CO_2 at percolation versus reciprocal of buoyancy gradient, $1/(\Delta\rho g)$ is given in Figure 5-2.

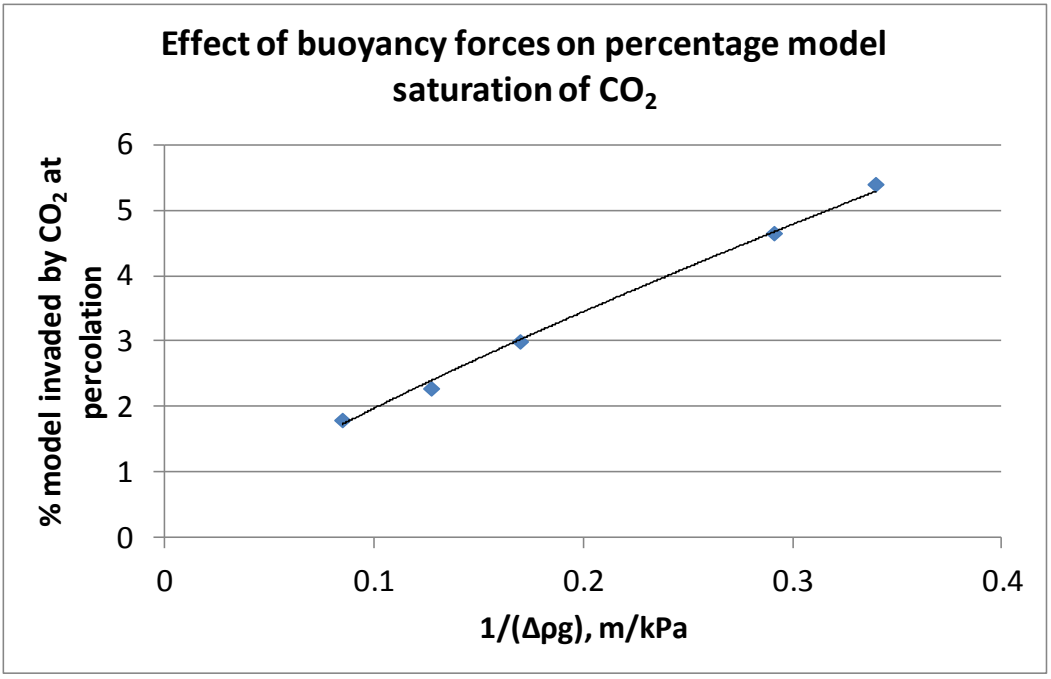

Figure 5-2: Effect of buoyancy forces on capillary channels of CO_2. The % CO_2 invasion of domain at percolation has a positive correlation with $1/(\Delta\rho g)$. Higher buoyancy forces lead to fingering and less invasion of the domain while lower buoyancy forces enhance lateral movement of CO_2.

The % CO_2 invasion of domain at percolation has a positive correlation with $1/(\Delta\rho g)$. With larger buoyancy forces, CO_2 fingers through the same rock that it back-fills when the density difference between CO_2 and brine is smaller. As buoyancy force increases the fluid potential to overcome any capillary barriers it encounters in the medium is higher. Hence CO_2 can finger through with minimal rock contact in such cases.

5.1.2 Effect of heterogeneity on capillary channels

In this section we simulate buoyancy-driven migration of CO_2 in the capillary channel migration regime on rocks of varying degrees of heterogeneity. To achieve this, we can vary two aspects that control heterogeneity of a medium namely, threshold pressure distribution and the correlation length of the threshold pressures in the horizontal and vertical directions i.e. the range of grain sizes and their spatial distribution in the rock.

5.1.1.1 Effect of threshold pressure range on capillary channels

In the first case we keep the depositional fabric (correlation structure of depositional sedimentary fabric) the same but change the assigned values (ranges and magnitudes) of threshold pressure. We vary the standard deviations of the threshold pressure distribution about the mean threshold pressures, which are held constant at a particular value for each set of simulation runs. Wider ranges of threshold pressure imply more spatial heterogeneity in the medium, e.g. more variation in average grain size or in sorting, while narrower threshold pressure ranges suggest more homogeneous or well-sorted domains. The density difference between the CO_2 and native brine is held constant at 300 kg/m^3 for all the simulations in this case.

We explain one such set of simulations here. In the 0.4 m wide × 0.4 m tall percolation model domain with depositional fabric of peel # 1 (Figure 4-9), we increase the standard deviations from 0.08, 0.48 to 1.37 kPa about the mean threshold pressure, which is held fixed at 7.4 kPa. The $<P_{th}>$ of 7.4 kPa is determined from sampling the actual peel. Smaller $<P_{th}>/\sigma_{Pth}$ (or high σ_{Pth}) values represent heterogeneous media while larger $<P_{th}>/\sigma_{Pth}$ values imply very homogeneous media.

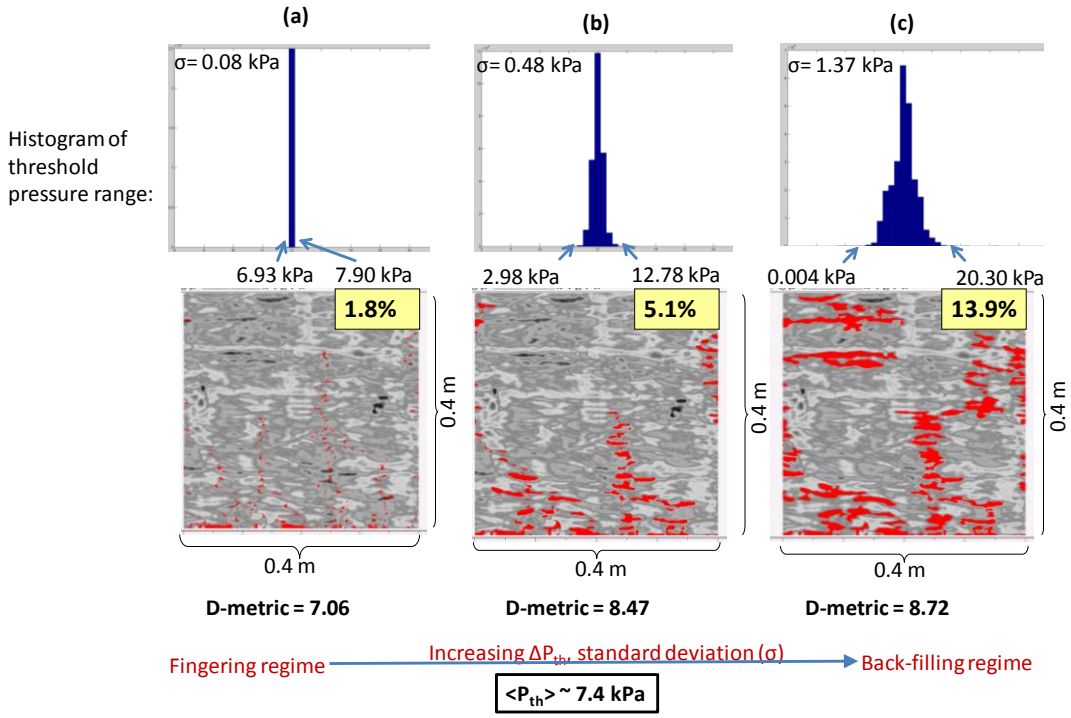

Figure 5-3: Flow patterns vary from fingering to back-filling patterns with increasing threshold pressure range in peel # 1 depositional fabric. Here, threshold pressure range = max(P_{th}) - min(P_{th}). <P_{th}> is held fixed at 7.4 kPa. Domains with wider threshold pressure distribution cause CO_2 to back-fill beneath contiguous regions of larger threshold pressure (light gray areas in background P_{th} map) causing more CO_2 to invade the domain. Cell dimensions are 2 mm × 2 mm. The IP model domain is 0.4 m wide × 0.4 m tall having 2000 cells × 2000 cells. Density difference between the CO_2 and native brine = 300 kg/m^3 in all cases. The insets at the top right corner of the simulations indicate the percentage of the domain invaded by CO_2 at percolation. The D-metric for each of these simulations also varies.

In this fixed depositional fabric, CO_2 migration in capillary channels exhibits very different migration patterns varying from capillary fingering to back-filling structures as threshold pressure distribution widens in the domain (Figure 5-3). The fingering pattern exhibits structures of narrow, mostly vertical, preferential flow paths that yield a very

small average saturation of CO_2 in the domain. In an extremely well-sorted rock (Figure 5-3(a)) CO_2 encounters few capillary barriers due to the narrow range of threshold pressure distribution. These capillary channels efficiently transport all CO_2 that enters the domain through a few narrow, generally vertical pathways. The back-filling pattern (Figures 5-3(c)) has numerous pools connected by finger structures yielding a larger average saturation. The pools are macro-scale accumulation zones having high CO_2 saturations, and pools are usually connected by narrow flow paths or fingers. Higher σ_{Pth} values lead to more probable capillary barriers that drive more lateral migration and bigger accumulations of CO_2 form due to capillary trapping compared to very homogeneous rocks. Poorer sorting (Figures 5-3(b) and 5-3(c)) thus reduces efficiency of CO_2 migration through the domain.

The results from Figure 5-3 are quantitatively represented in Figure 5-4. Figure 5-4 shows the percentage of the domain invaded by CO_2 for increasing dimensionless threshold pressure, $<P_{th}>/\sigma_{Pth}$. σ_{Pth} is a dominant control on the CO_2 migration patterns.

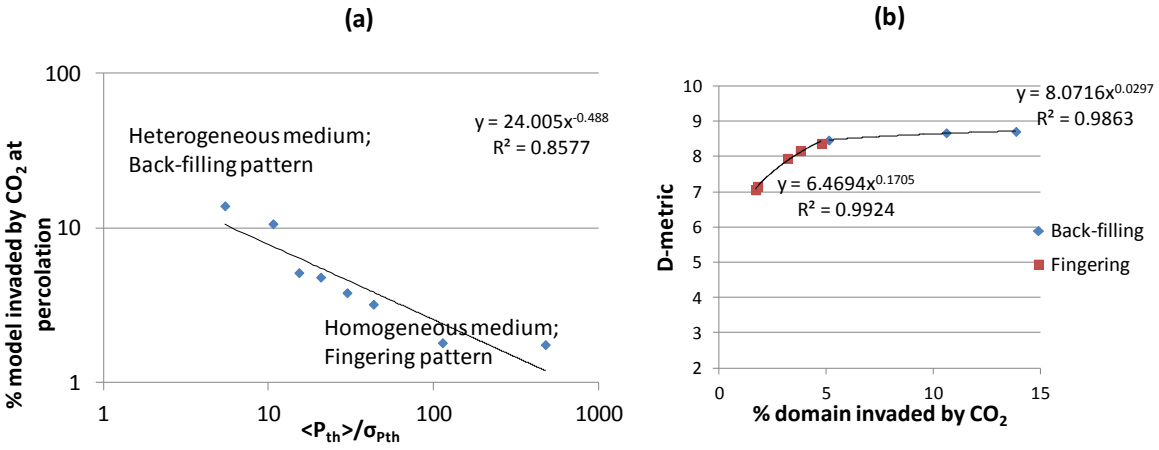

Figure 5-4: Flow transition from fingering to back-filling patterns compiled for the peel fabric with wider threshold pressure distributions. Panel (b) shows the D-metric versus the percentage of the domain invaded by CO_2 at percolation. $<P_{th}>$ = 7.4 kPa with increasing σ_{Pth}. Model dimensions are 0.4 m × 0.4 m with 2000 × 2000 cells with peel # 1 depositional fabric. Line source of CO_2 enters the model domains having periodic lateral

boundaries and migrates until percolation. Density difference between the CO_2 and native brine = 300 kg/m^3 in all cases.

The models interestingly exhibit power law correlation between the % domain invaded by CO_2 and the dimensionless P_{th} parameter. We observe distinct trend change in the average D-metric values at percolation as flow patterns transition from fingering to back-filling for wider ranges of threshold pressure as seen in Figure 5-4 panel (b) i.e. the slope of the D-metric values for the fingering pattern simulation runs is quite different from the D-metric trend for the back-filling simulations due to distinct differences in both these invasion styles. This transition between the flow patterns is continuous and gradual as panel (a) indicates.

We perform the same exercise of increasing the σ_{Pth} on the 0.4 m × 0.4 m rock section with other $<P_{th}>$ values. $<P_{th}>$ values of 7.4 kPa (from peel #1), and 5 kPa are picked for this exercise. Higher $<P_{th}>$ implies finer mean grain sizes in the medium with σ_{Pth} being a measure of the range of mean grain sizes throughout the medium (i.e. not the sorting at any single location). The depositional fabric for all these simulations is from the peel # 1 (Figure 4-9). Figure 5-5 shows the percentage of the model invaded by CO_2 at percolation for different $<P_{th}>/\sigma_{Pth}$ values.

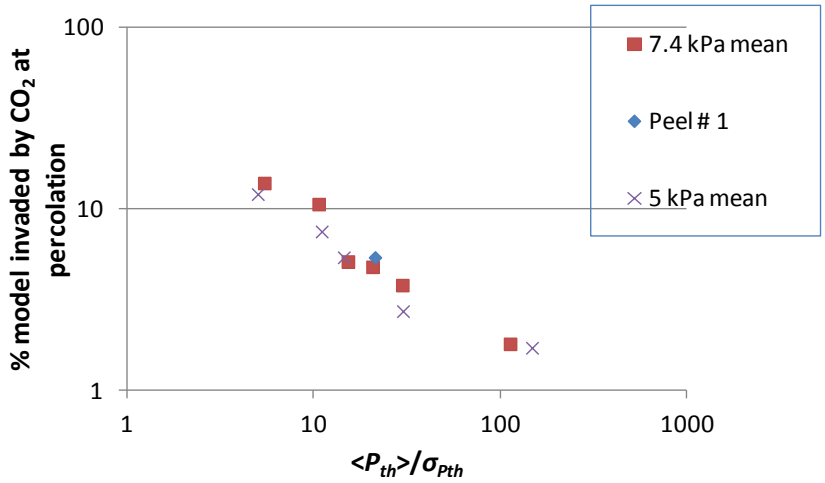

Figure 5-5: Plot of percentage of the domain invaded by CO_2 versus dimensionless threshold pressure for different $<P_{th}>$. The depositional fabric from the peel # 1 is used

for all the model domains. For a given $<P_{th}>/ \sigma_{Pth}$, CO_2 migration regimes are found to be the same. σ_{Pth} is a dominant control on the CO_2 migration patterns. The models are 0.4 m × 0.4 m with periodic lateral boundaries and have a line source of CO_2 entering from the bottom of the domain. Density difference between the CO_2 and native brine = 300 kg/m^3 in all cases.

Figure 5-5 highlights the dependence of capillary channels on the ratio of $<P_{th}>/ \sigma_{Pth}$ (i.e. range of grain sizes throughout the domain). The relative difference between the sizes of adjoining pore throats and pore bodies governs percolation. Greater this relative difference, more the possibility of the adjacent pore throat being a capillary barrier to fluid migration. The actual values of $<P_{th}>$ do not greatly affect the percentage invasion values for heterogeneous model domains i.e. ~12% invasion for $<P_{th}>/ \sigma_{Pth} = 5$. $<P_{th}> = 7.4$ kPa gives slightly greater % invasion compared to $<P_{th}> = 5$ kPa in Figure 5-5). Above $<P_{th}>/ \sigma_{Pth} = 30$, we encounter no significant influence of the grain size. Relatively homogeneous model domains which cause CO_2 to finger do not see a pronounced effect of $<P_{th}>$ (~1.8 % invasion for $<P_{th}>/ \sigma_{Pth} = 100$ and 150 in Figure 5-5). Note however that the simulations assume that CO_2 is supplied at whatever capillary pressure is needed to invade the next grid block. Thus for the same pattern to occur in two different domains with the same dimensionless mean threshold pressure, the CO_2 plumes would have to be scaled appropriately in each case.

5.1.1.2 Effect of correlation length of threshold pressures in the horizontal and vertical directions on capillary channels (effect of the depositional fabric)

In this second case we keep the threshold pressure distribution of the medium constant but vary the correlation length of threshold pressures in the horizontal and vertical directions. This academic exercise (in nature it is unlikely that the fabric would change without also changing the grain size distributions) reiterates the influence of the spatial structure of the rock.

The depositional fabrics of the media in this case are generated statistically. We generate geostatistical simulations with the ratio of horizontal threshold pressure to vertical threshold pressure as 1, 10 and 100 (Figure 4-1 fabrics (A), (B) and (C)). Each domain is 0.4 m x 0.4 m like the peel sub-section in the previous case (2000 cells wide × 2000 cells tall) for ease of comparison. Figure 5-6 shows CO_2 migration patterns in these media having constant threshold pressure values normally distributed between 6.1- 8.9 kPa with $<P_{th}>$ = 7.4 kPa. The lateral flow boundaries of the model domains are periodic here as well.

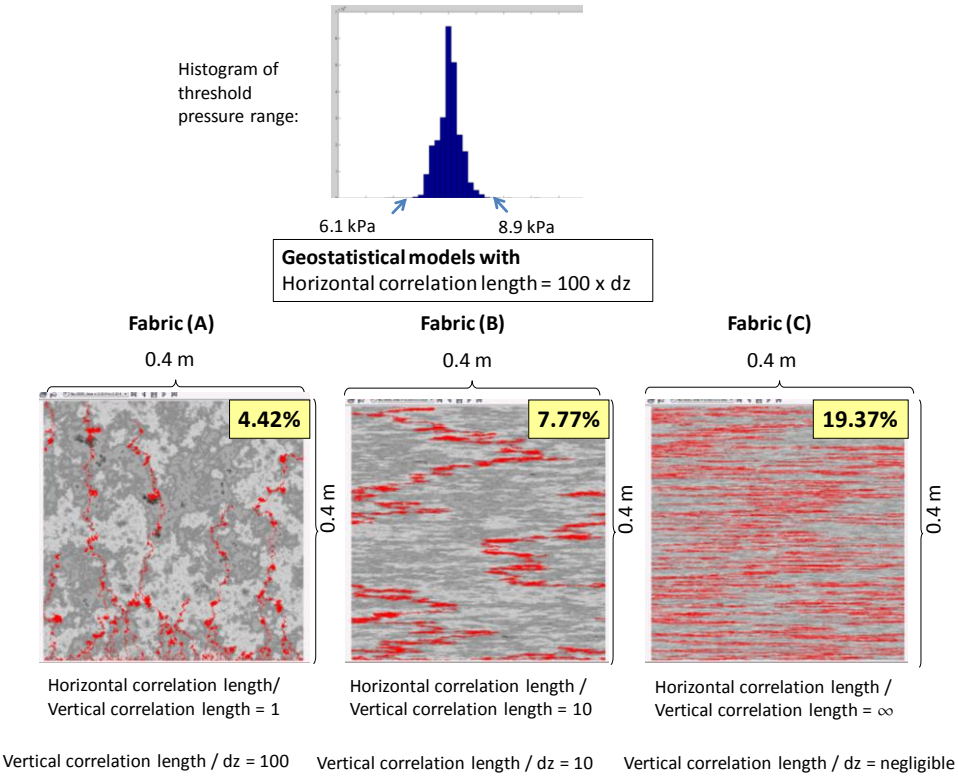

Figure 5-6: Flow transition from fingering to back-filling patterns occurs with increasing ratio of correlation of P_{th} in horizontal and vertical directions. Constant threshold pressure range of 6.1-8.9 kPa with $<P_{th}>$ of 7.4 kPa. Cell dimensions are 2 mm × 2 mm. The domain is 2000 cells wide × 2000 cells tall (i.e. 0.4 m × 0.4 m). Constant density difference between the CO_2 and native brine = 300 kg/m^3.

With greater ratio of correlation length of threshold pressures in the horizontal to vertical directions, the size of CO_2 accumulations increases as flow transitions towards more back-filling. For media with more horizontal correlation length of threshold pressures the capillary barriers are more laterally extensive too. Hence they impose a substantial horizontal flow component that influences CO_2 migration regime and enable more fluid-rock contact as well as higher capillary trapping capacity.

In Figure 5-6 the resolution of the models is constant at depositional resolution. The resolution of the domains is an important aspect of modeling. We maintain the same sedimentologic structure of the domain while coarsening the cell size to illustrate the effect of cell height on capillary channels of CO_2. The fabric (B) with vertical correlation length of $P_{th} = 10 \times dz$ is used for this analysis. Cell dimensions are increased from the original 2 mm × 2 mm to 4 mm × 4 mm, 10 mm × 10 mm and 20 mm × 20 mm in the 0.4 m × 0.4 m model domains. Figure 5-7 gives the results of this analysis of the effect of cell height on the capillary channels of CO_2.

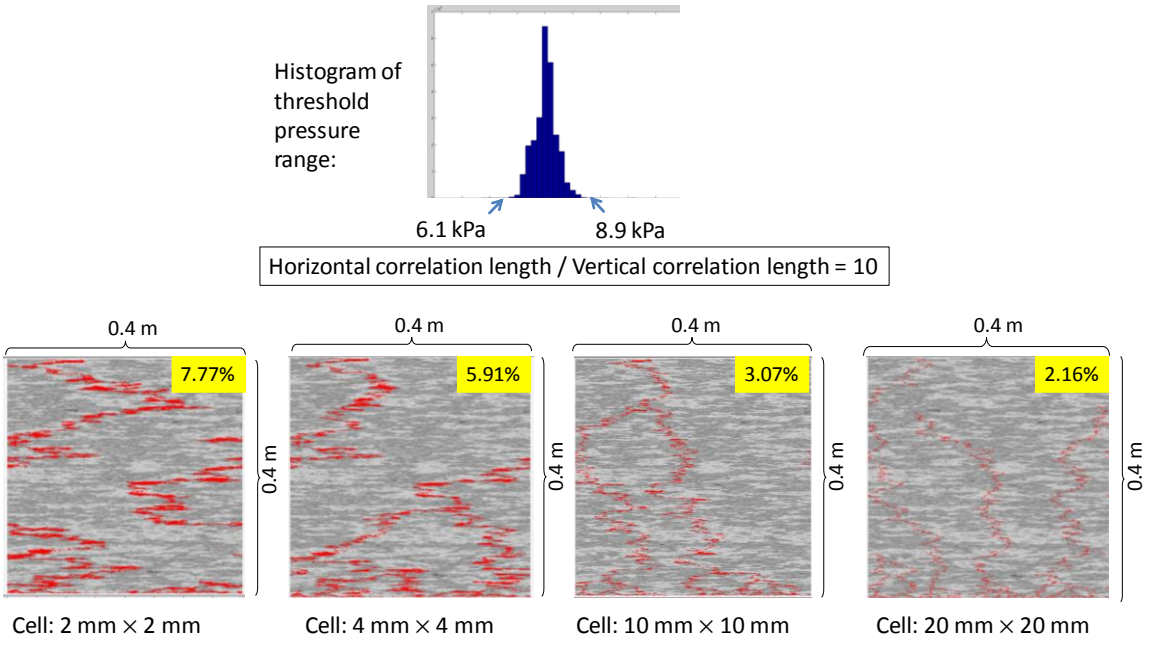

Figure 5-7: Effect of cell height on migration patterns in the capillary channel flow regime. The leftmost panel is the simulation at original depositional resolution. Cell

dimensions increase/ coarsen in multiples of this original value as indicated when we move towards the panels on the right. The geostatistical fabric (B) is used for this set of simulations.

As we coarsen the grid size, for the same sedimentologic structure in Figure 5-7, we observe decreasing effective rock-fluid contact volume and more disperse saturation distributions. The driving force for CO_2 invasion in this case increases with grid size because the plumes are physically taller. The results are thus quite similar to the fluid density contrast cases as the density difference becomes larger. Hence, using the right resolution for the models is an important consideration that could significantly influence predictions of plume dynamics.

The statistical models generated with increasing correlation lengths of threshold pressures in the horizontal and vertical directions represent rocks with increasing degree of heterogeneity. We vary the standard deviations at 0.02, 0.45 and 1.3 kPa about the mean threshold pressure for each depositional fabric (Figure 5-8 columns 1, 2 and 3). The mean threshold pressure is set to 7.4 kPa. The rows A, B, C and D in Figure 5-8 thus correspond to varying depositional fabric while the columns 1, 2 and 3 correspond to specific grain size distributions in 0.4 m × 0.4 m model domains (2000 cells wide × 2000 cells tall). The background depositional fabrics in rows A, B and C of Figure 5-8 are geostatistical simulations with the ratio of correlation lengths of threshold pressure in the horizontal to vertical direction as 1, 10 and 100 respectively. In each geostatistical model, the correlation length of the threshold pressure in the horizontal direction is held fixed (= 100 × cell height). Row D in Figure 5-8 is the set of simulations on the peel # 1 fabric (section 5.1.1.1).

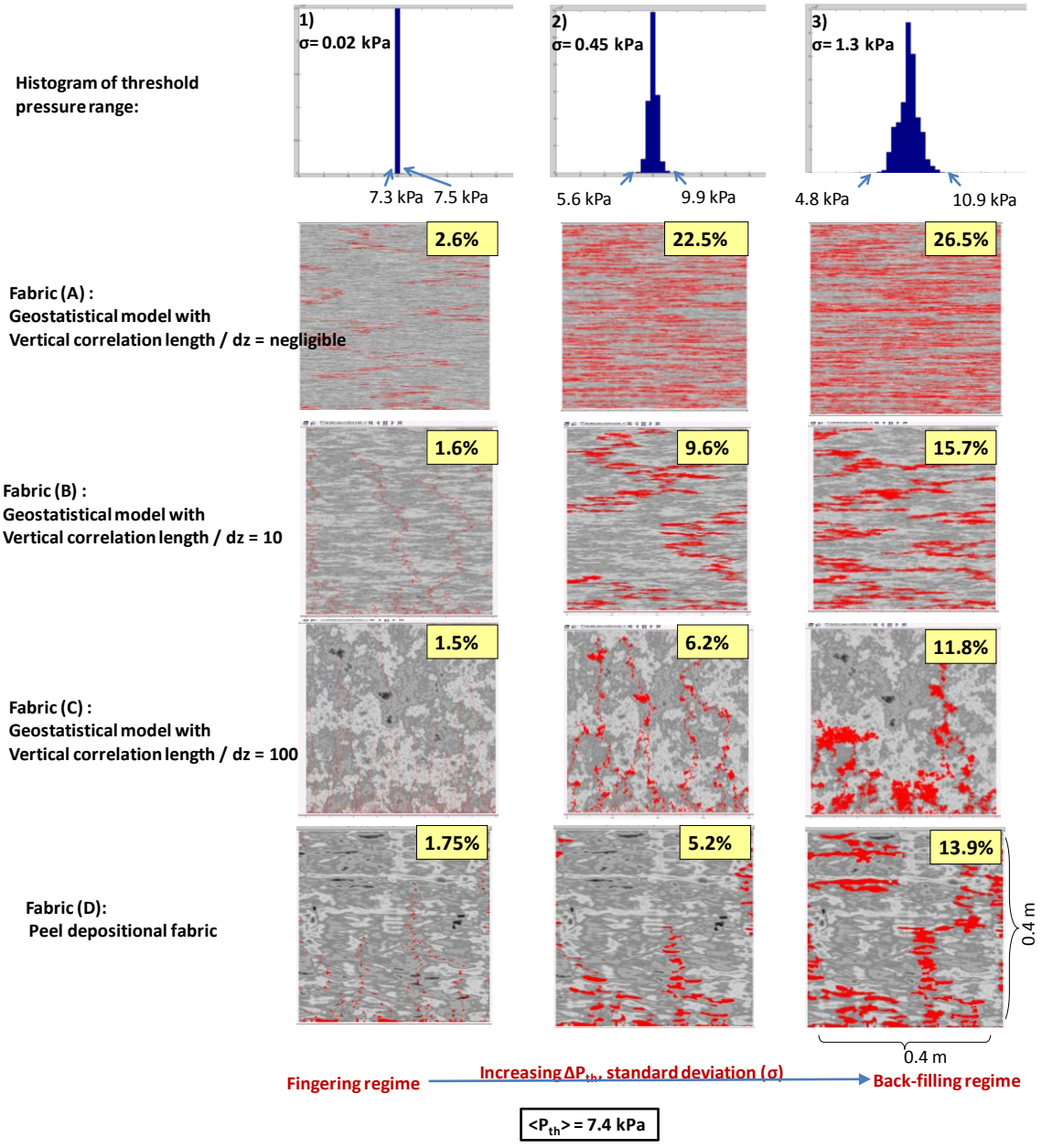

Figure 5-8: Invasion percolation simulations in capillary-channel regime of CO_2 migration. Rows represent a specific depositional fabric while columns represent a specific grain size distribution. The insets at the top-right corner of the simulations indicate the percentage domain invaded by CO_2 at percolation. Row (D) uses the peel natural depositional fabric. Rows (A), (B) and (C) are geostatistical simulations with prescribed correlation of P_{th} in horizontal and vertical directions. Horizontal correlation

length is constant (=100 × *dz*; *dz* = 2 mm), and vertical correlation length varies by row as indicated. In the panels of each row (A, B, C and D), the pattern of rising CO_2 transitions from fingering (1st column) to back-filling (3rd column) patterns as the standard deviation in threshold pressure σ_{Pth} increases for a fixed depositional fabric. $<P_{th}>$ is 7.4 kPa for all panels. Domains with wider grain size frequency distribution cause CO_2 to back-fill beneath contiguous regions of larger threshold pressure (light gray areas in background P_{th} map) causing CO_2 to invade more of the domain. The influence of the background depositional fabric on capillary channel flow patterns is apparent in panels of the 2nd column. The domains are 2000 cells wide × 2000 cells tall (i.e. 0.4 m × 0.4 m). Density difference between the CO_2 and native brine = 300 kg/m^3 in all cases.

For each depositional fabric (Figure 5-8 rows A, B, C and D), we observe CO_2 migration patterns ranging from 'dispersed' capillary fingering structures with minimal rock contact toward back-filled structures with bigger accumulations of CO_2 as heterogeneity increases. Media with more correlation length of threshold pressures in the horizontal compared to the vertical direction impose a substantial horizontal component of migration that enables more fluid-rock contact as well as higher capacity for capillary trapping.

The fraction of the domain invaded at percolation is plotted in Figure 5-9 against dimensionless threshold pressure in the three geostatistical model fabrics. The invaded fraction increases in more heterogeneous domains as there are more potential capillary barriers in the domain that drive lateral migration compared to very homogeneous rocks. The flow patterns for specific values of the dimensionless threshold pressure are found to be the same for different depositional fabrics, with the slight variations in the percentage saturation values attributed to the influence of the fabric itself. The 0.4 m × 0.4 m section of the real peel sample is also plotted in Figure 5-9 (blue data point). The peel behaves as expected from the resulting trend in the geostatistical fabrics. This indicates the

possibility of predictive ability for expected flow patterns when the threshold pressure distribution of the medium and fluid properties of the system are known.

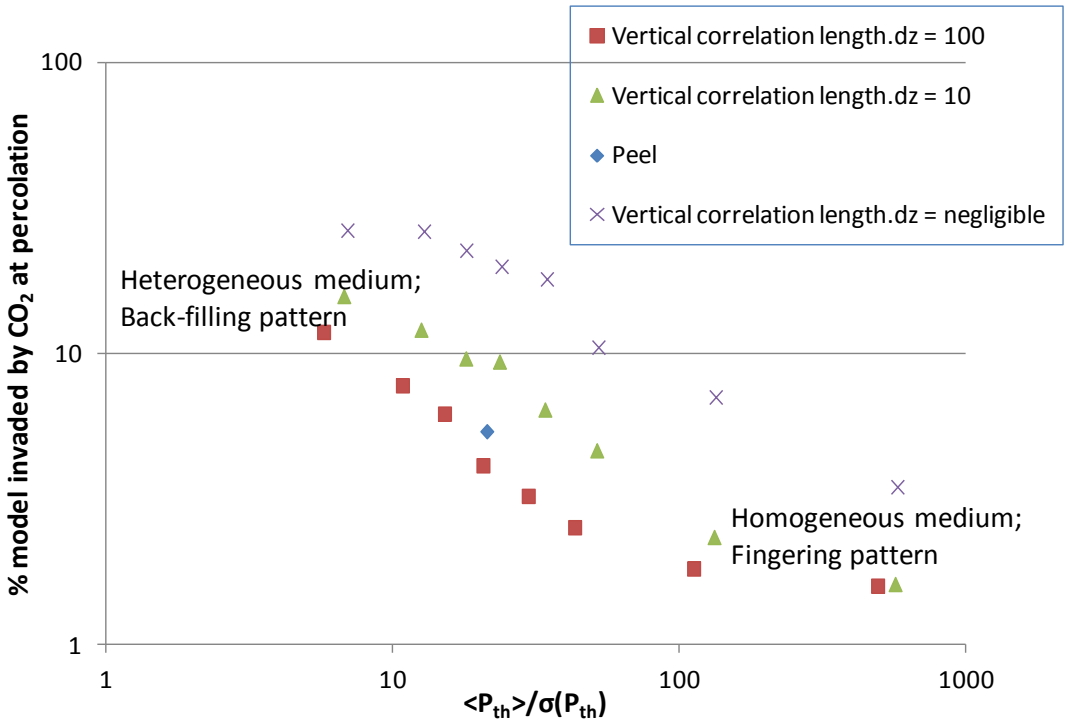

Figure 5-9: Fraction of rock invaded by CO_2 in capillary-channel regime depends on heterogeneity. Except in very homogeneous domains (large dimensionless threshold pressure), where the invaded fraction approaches a lower bound, a power law relates the invaded fraction (values from Fig. 5-8) to the dimensionless threshold pressure $<P_{th}>/\sigma_{Pth}$ of the medium for different depositional fabrics. Simulations for line source of CO_2 on the 0.4 m × 0.4 m domain for $<P_{th}>$ = 7.4 kPa in the three geostatistical models and on the 0.4 m × 0.4 m working peel model are plotted. Each point on the plot represents a simulation for a specific threshold pressure distribution on the given depositional fabric. The rocks are more homogeneous for greater values of $<P_{th}>/\sigma_{Pth}$. For the geostatistical models, horizontal correlation length is constant (=100 × *dz*; *dz* = 2 mm), and vertical correlation length varies as vertical correlation = (100, 10 and negligible) × *dz*.

5.1.3 Sensitivity analysis on sample specimen

We impose threshold pressure distributions of varying means and standard deviations given in Figure 4-4. The percentages of invasion of the 0.4 m × 0.4 m peel # 1 model domain by CO_2 at percolation on these 54 samples are compiled in the Figure 5-10.

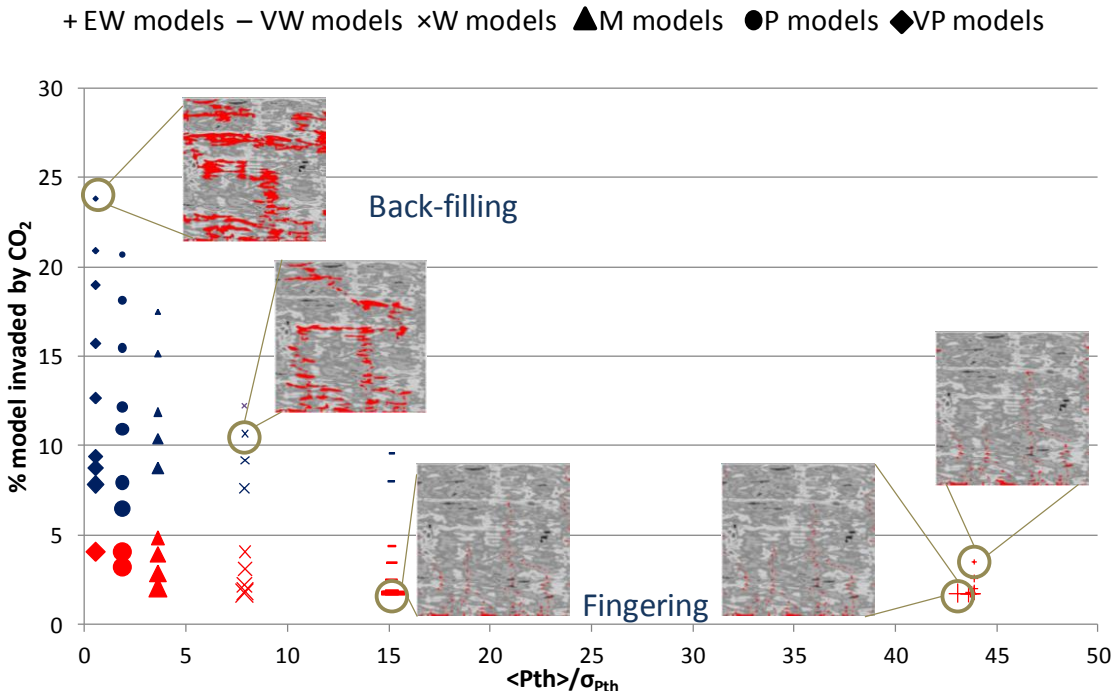

Figure 5-10: Plot of percentage of the domain invaded by CO_2 versus dimensionless threshold pressure data using 54 different frequency distributions of threshold pressure (Figure 4-4). The simulations are grouped columnwise/ vertically according to the standard deviation from small (corresponding to extremely well-sorted, EW) to large (corresponding to very poorly sorted, VP) domains. The size of the data points in each column gives an idea of the mean threshold pressure of the sample i.e. bigger size of data points indicate smaller mean threshold pressure. The fingering pattern simulations are indicated in red. The domains are 2000 cells wide × 2000 cells tall (i.e. 0.4 m × 0.4 m) with periodic X-boundaries. The depositional fabric of the peel # 1 is used for all the simulations. Density difference between the CO_2 and native brine = 300 kg/m^3 in all cases.

Fingering occurs in almost half the samples in Figure 5-10. 28 out of 54 samples result in % invasion values below 5% at percolation. The extremely well-sorted media always exhibit fingering patterns. The $<P_{th}>/\sigma_{Pth}$ for these domains are greater than 30 and hence the effect of $<P_{th}>$ is not dominant here. Very few samples (only 9 out of 54 samples) result in greater than 15% of the domain being invaded by CO_2. The mean grain size has noticeable impact on the flow patterns for a given sorting for $<P_{th}>/\sigma_{Pth} < 30$. This is different from the results in Figures 5-4, 5-5 and 5-9, all of which show that the ratio $<P_{th}>/\sigma_{Pth}$ (dimensionless threshold pressure) is a good predictor of the % invasion achieved in a given model domain. This first order effect of $<P_{th}>$ observed in Figure 5-10 needs to be investigated further.

We next simulate capillary channel flow of CO_2 in wider range of threshold pressure domains (from Figure 4-4) in 3 geostatistical fabrics (A), (B) and (C) (Figure 4-1) to determine characteristic invasion patterns. The model domains in this case are 0.4 m × 0.4 m (2000 cells × 2000 cells) with periodic lateral flow boundaries. Results for all the 0.4 m × 0.4 m domain simulations are compiled in Figure 5-11. These compiled results for the percentage invasion at percolation from Permedia are linearly interpolated to act as an **IP predictor model**. This IP predictor model can be used to interpolate and obtain % invasion values if all three parameters characterizing the system (i.e. anisotropy, $<P_{th}>$ and σ_{Pth}) are known.

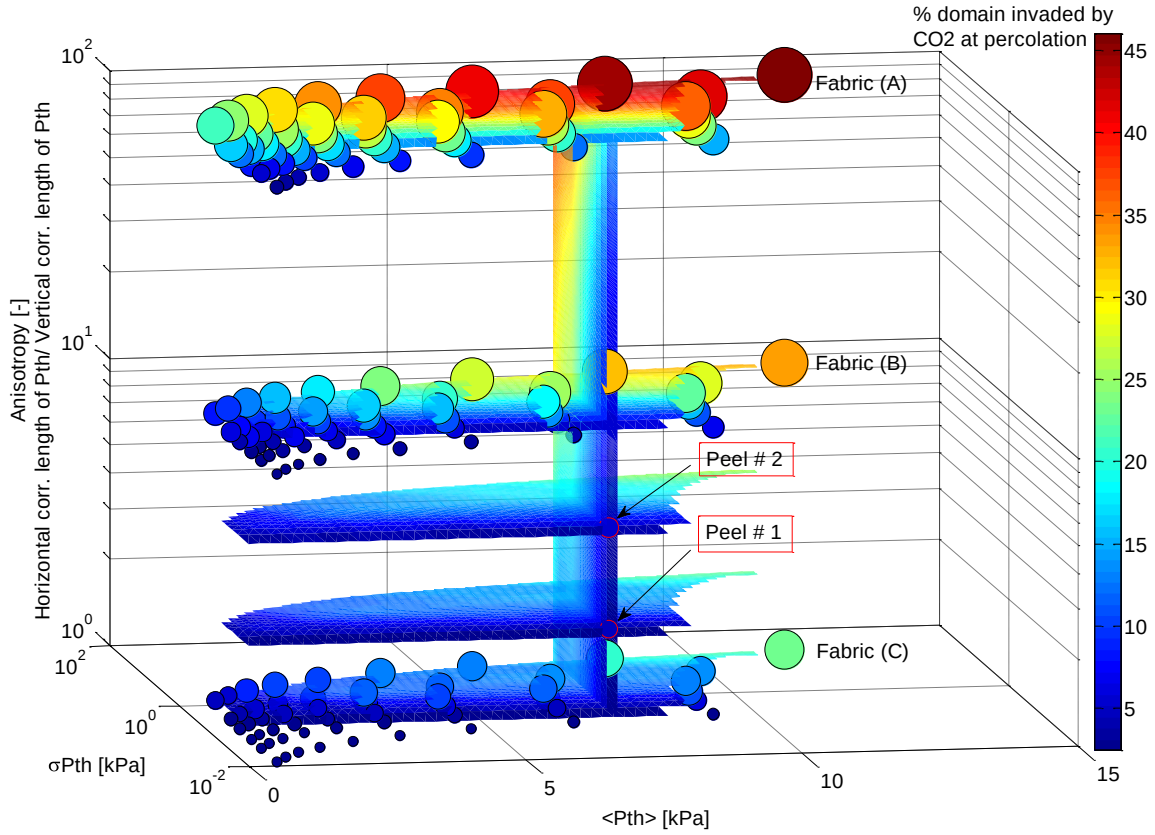

Figure 5-11: Invasion percolation simulations of CO_2 migrating through the geostatistical models with three fabrics (identified by their correlation lengths, the vertical Z-axis), nine average entry pressures (X-axis) and six values of standard deviation of the entry pressure frequency distribution (Y-axis). Colour of dot indicates fraction of domain occupied by CO_2 when CO_2 reaches top of the domain. Continuous line source was placed at bottom boundary of model domains, lateral flow boundaries are periodic. The color gradation in each fabric plane is obtained by linear interpolation; this interpolation is the "IP predictor model". The Permedia results for the 0.4 m × 0.4 m natural peel model sections plot with reasonable accuracy on this linearly interpolated % invasion plot (IP predictor model).

The 54 points in each plane correspond to threshold pressure distributions in Figure 4-4. Each plane in Figure 5-11 represents simulations on a particular depositional fabric (0.4 m × 0.4 m geostatistical models). The variation in the percentage saturation values is

attributed to the influence of the fabric itself for given values of $<P_{th}>$ and σ_{Pth}. Fabric (A) with very high anisotropy sees significant back-filling (up to 46% of domain invaded by CO_2 at percolation) as the heterogeneity of the domain increases. The % invasion increases for finer-grained specimen as the sorting worsens as observed earlier.

The 0.4 m × 0.4 m section of the peel samples are also plotted in Figure 5-11. Both the natural peel model sections (Permedia simulation results) plot with reasonable accuracy on this linearly interpolated % invasion plot (IP predictor model). Peel # 1 gives a simulated value of 5.4% domain invasion at percolation in Permedia while the IP predictor model predicts 4.6%. Peel # 2 gives a simulated value of 5% domain invasion at percolation in Permedia while the IP predictor model predicts 5.7%. This indicates the possibility of predictive ability for expected flow patterns when the threshold pressure distribution of the medium and fluid properties of the system are known.

5.2 Exploring capillary channel flow of buoyant CO_2 in real geologic fabrics

We know behavior in various rock systems from the sensitivity analyses. We corroborate migration behavior by simulating capillary channel flow in the 2 real peel models. Here are the results:

5.2.1 Simulation of capillary channel flow in the peel model # 1

We simulate buoyant CO_2 migration through the 1 m × 0.5 m representative digital model of the peel specimen to study non-wetting phase invasion in the capillary channel migration regime (Figure 5-12). Table 5-1 gives the input parameters for the invasion percolation model of peel # 1.

Parameter	Value
Threshold pressure	6.1-8.9 kPa; normal distribution of values with $<P_{th}>$ = 7.4 kPa and σ_{Pth} = 0.4 kPa
Porosity	20%

Connate water saturation, S_{wc}	20%
Critical oil saturation, S_{ocr}	2%
Flow boundary conditions	PERIODIC lateral flow boundaries
Depth from datum	1615.44 m
Density difference between CO_2 and brine	300 kg/m^3
Interfacial tension, IFT multiplier	0.065

Table 5-1: Input parameters for the invasion percolation model of peel # 1 (1 m × 0.5 m).

Maximum and minimum threshold pressure values of 6.1 to 8.9 kPa ($<P_{th}>$=7.4 kPa) are assigned to the threshold pressure field of the model corresponding to the minimum and maximum grain sizes of 0.055 and 0.08 mm determined for the specimen. Density difference between CO_2 and native brine is taken to be 300 kg/m^3. CO_2 is sourced from the bottom of the medium (periodic X-boundaries) and allowed to migrate through the medium until it percolates through it. Figure 5-12 gives the invasion pattern of CO_2 in this model domain.

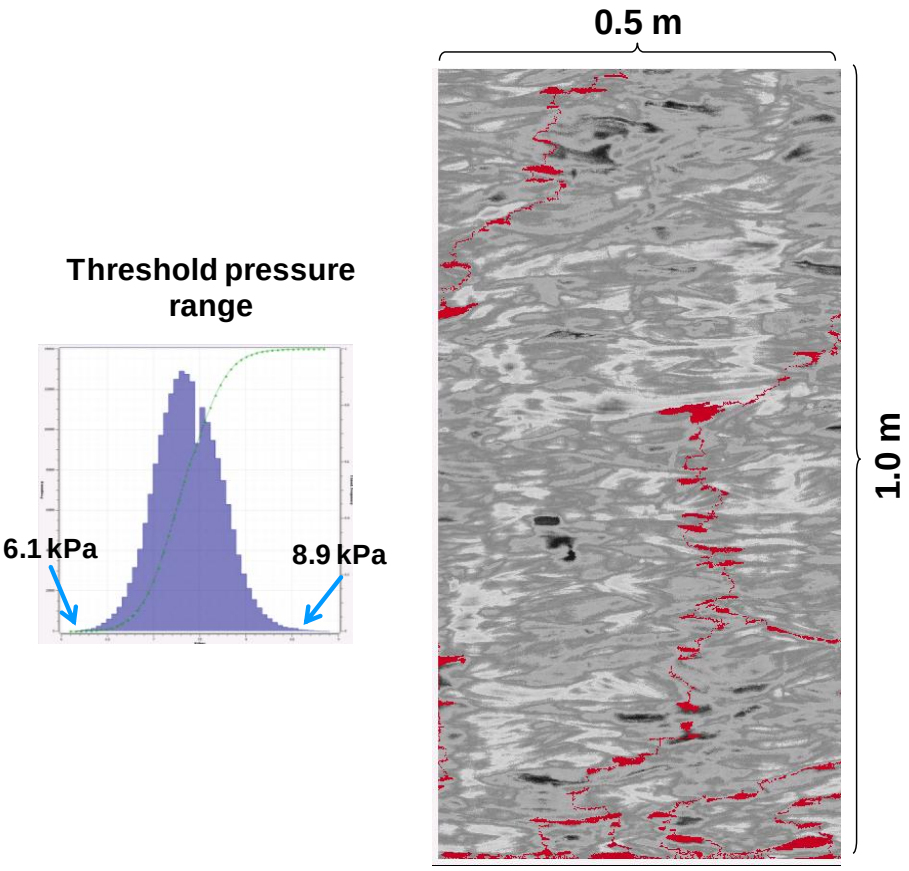

Figure 5-12: Invasion percolation simulation of CO_2 migrating through the peel # 1 model (1 m × 0.5 m). Continuous line source was placed at bottom boundary of model domain, left and right boundaries are periodic. The CO_2 flow pattern is characterized as 'fingering'. 2.86% of the model domain is saturated with CO_2 at percolation.

CO_2 fingers migrate preferentially through regions of lower threshold pressure. The displacement patterns have an architecture defined by the depositional fabric. The percentage of the domain saturated with CO_2 is 2.86%, which is quite small. The CO_2 occasionally forms small accumulations below the light gray patches corresponding to capillary barriers having highest threshold pressures in the domain (Figure 5-12). These capillary channels/ fingers efficiently transport all CO_2 that enters the domain through a few narrow, generally vertical pathways.

5.2.2 Simulation of capillary channel flow in the peel model # 2

We simulate buoyant CO_2 migration through the 0.4 m × 0.4 m representative digital model of the peel # 2 specimen to study non-wetting phase invasion in the capillary channel migration regime (Figure 5-13). Maximum and minimum threshold pressure values of 6.1 to 8.9 kPa ($<P_{th}>$=7.4 kPa) are assigned to the normally-distributed threshold pressure field of the model corresponding to minimum and maximum grain sizes of 0.055 and 0.08 mm. Density difference between CO_2 and native brine is taken to be 300 kg/m^3. CO_2 is sourced from the bottom of the medium (periodic lateral flow boundaries) and allowed to migrate through the medium until it percolates through it. Table 5-2 gives the input parameters for the invasion percolation model of peel # 2.

Parameter	**Value**
Threshold pressure	6.1-8.9 kPa; normal distribution of values with $<P_{th}>$ = 7.4 kPa and σ_{Pth} = 0.4 kPa
Porosity	20%
Connate water saturation, S_{wc}	20%
Critical oil saturation, S_{ocr}	2%
Flow boundary conditions	PERIODIC lateral flow boundaries
Depth from datum	1615.44 m
Density difference between CO_2 and brine	300 kg/m^3
Interfacial tension, IFT multiplier	0.065

Table 5-2: Input parameters for the invasion percolation model of peel # 2 (0.4 m × 0.4 m section).

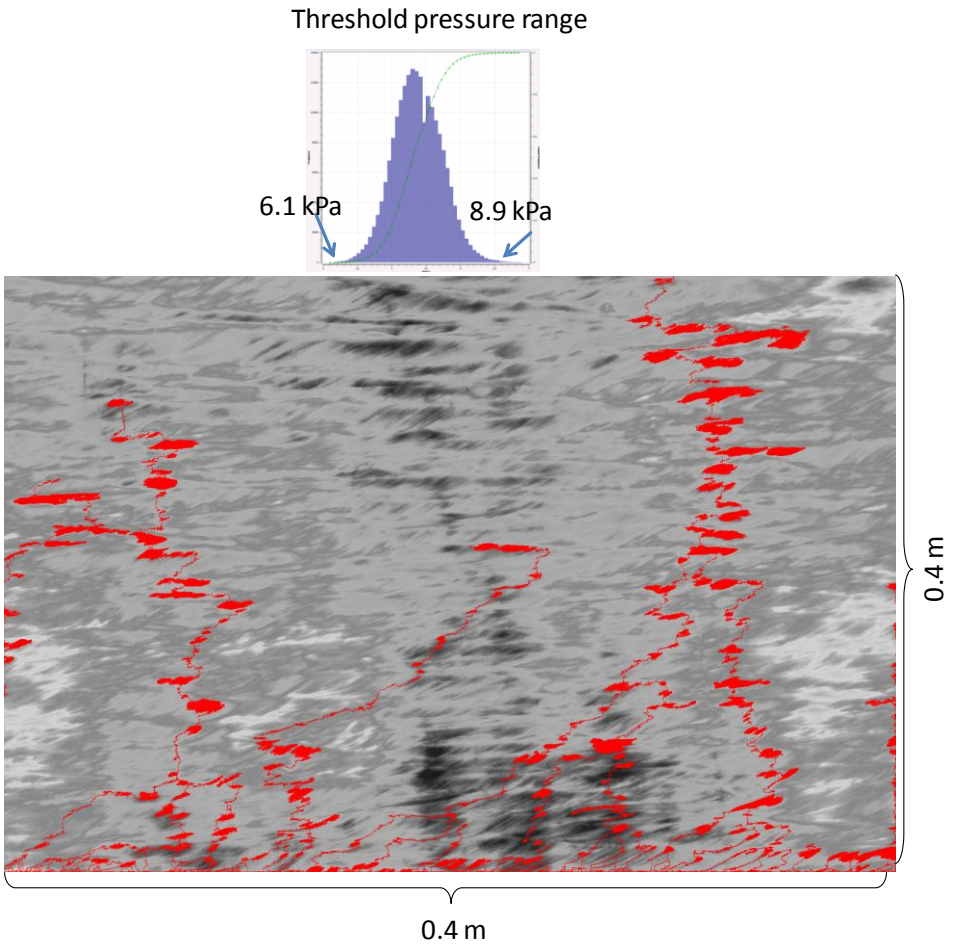

Figure 5-13: Invasion percolation simulation of CO_2 migrating through the peel # 2 model section. Continuous line source was placed at bottom boundary of model domain, left and right boundaries are periodic. 5% of the model domain is invaded by CO_2 at percolation.

5.3 Reproducibility of IP simulation outputs

The threshold pressure distribution in the FID-PAR models is generated by assigning a P_{th} distribution to each FID. The actual threshold pressure value for that FID in the domain is chosen by a random seed generator for each simulation run. The seed value for the random seed generator thus has a bearing on the actual values of threshold pressure of

the pore throats in the medium. We investigate the reproducibility of our results using different P_{th} values sampled from the assigned threshold pressure distribution of the rock.

The model domain is the 0.4 m × 0.4 m sub-section of the peel # 1. Density difference between CO_2 and native brine is taken to be 300 kg/m^3. Line source of CO_2 enters from the bottom of the model domain and is allowed to migrate through the medium until it percolates to the top boundary. The lateral flow boundaries of the model are periodic. The normally-distributed threshold pressure field has $<P_{th}>$=7.4 kPa and σ_{Pth} = 0.4 kPa in this peel model. Table 5-3 gives the values for 10 such sampling trials.

Random seed value	**% domain invaded by CO_2 at percolation**
1234	5.4022
2468	5.4070
6170	5.4066
12340	5.4045
18510	5.4071
24680	5.4057
30850	5.4060
37020	5.4078
49360	5.4028
61700	5.4042

Table 5-3: Values of seed numbers and the resulting percentage invasion of the domain by CO_2 in each case

We observe a very narrow range of variation in the percentage invasion values for the various random seed values. Hence we conclude that the reproducibility for these IP models is very good.

5.4 Comparison cases between invasion percolation physics and finite difference full physics simulators

The migration behavior in Figures 5-12 and 5-13 are specific to that geologic specimen assuming that the height of the CO_2 plume entering the specimen is sufficient for its percolation through that medium. The simulator used is intended for basin analysis, which explores migration of hydrocarbons generated at depth and migrating toward potential traps. Basin analysis identifies traps and potential leads and prospects in the area likely to have received hydrocarbons. While basin modeling is performed on a large scale, buoyancy and capillary forces acting over small domains are still the main drivers influencing hydrocarbon migration. We need to ensure that invasion percolation captures the essential migration behavior equivalent to applying full-scale physics incorporating heterogeneity of the pore throat/size distribution of the medium, saturation and fluid potential gradients.

Considering the physics of invasion percolation gave us qualitatively sensible results for the migration of CO_2 in a heterogeneous domain. CO_2 flowed preferentially through regions of lower threshold pressure in a path of least resistance to percolate through the domain. However, since the purpose of exploring this regime is to ultimately find out its applicability on reservoir scale, we perform a reality check by comparing CO_2 migration behavior in a full physics, finite-difference standard simulator incorporating capillarity.

For the comparison, we generate different model domains with both line and point source of CO_2 in the media. The model domains in this exercise are 2-D consisting of 40000 cells (400 cells wide $\times$ 100 cells tall) for reasonable computational effort. All the boundaries of the model domain are closed. The simulations in both the invasion percolation simulator (Permedia®) and the full-physics simulator (GEM) are compared at the point when CO_2 has invaded the same percentage of the model domains. The test cases we simulate are:

1. Line source of CO_2 in a homogeneous medium (Section 5.4.1).
2. Point source of CO_2 in a homogeneous medium with a seal layer. There is a leak spot in this seal layer that CO_2 can escape through (Section 5.4.2).
3. Line and point sources of CO_2 in a heterogeneous medium (Section 5.4.3).
4. Comparison of capillary channel flow simulations in media of varying heterogeneity (Section 5.4.4).

5.4.1 Uniform rising front for perfectly homogeneous medium

We consider the simplest medium the first test case: homogeneous medium. Table 5-4 gives the input parameters for this model. Line source of CO_2 is introduced at the bottom of the medium (Figure 5-14). The line source in CMG (full-physics simulator) is defined as a block of high saturation of CO_2 below the reservoir. CO_2 is sourced from the bottom 4 rows of the models. Simulations are stopped when equal percentages of the model domains are filled with CO_2. For this comparison case, the flow boundaries of the medium are closed.

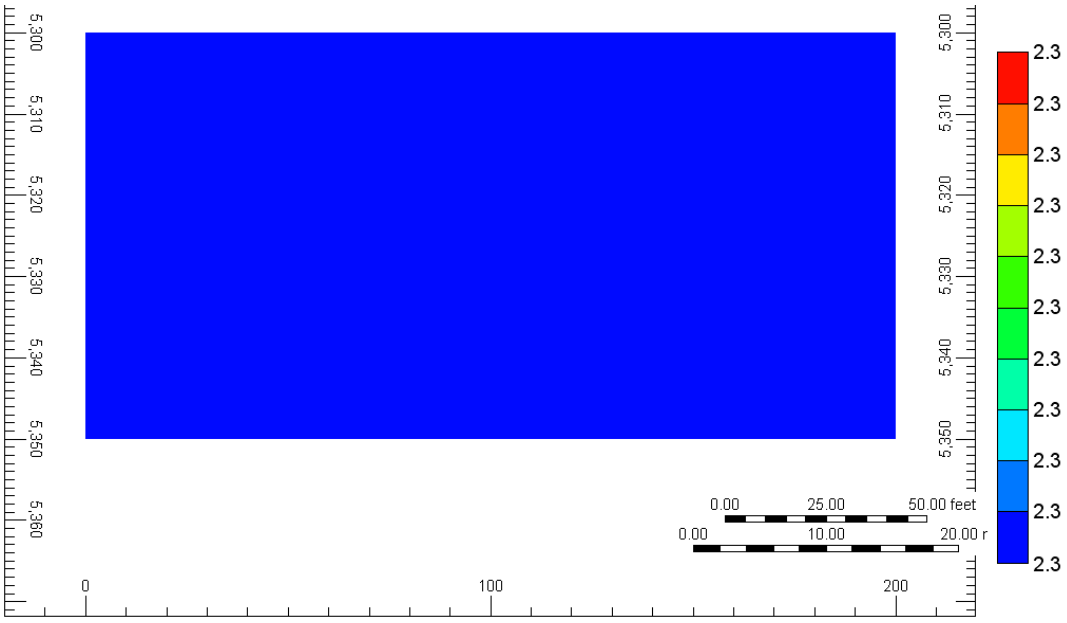

Figure 5-14: Threshold pressure map of the homogeneous model domain. Model dimensions are 60.9 m wide × 15.2 m tall.

Parameter	Value
Model dimensions	60.9 m wide × 15.2 m tall (200 ft wide × 50 ft tall)
Grid cell dimensions	0.1524 m × 0.1524 m (0.5 ft × 0.5 ft)
Threshold pressure	16 kPa (2.3 psi); same value for all cells in the domain
Permeability	200 mD
Porosity	47.6%
Connate water saturation, S_{wc}	20%
Critical oil saturation, S_{ocr}	2%
Flow boundary conditions	CLOSED
Density difference between CO_2 and brine	300 kg/m^3

Table 5-4: Input parameters for the model simulations

Full-physics simulator result

Invasion percolation simulator result

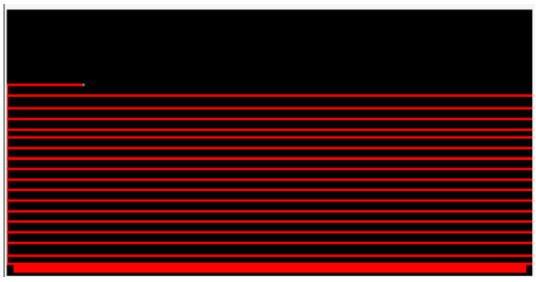

Figure 5-15: Gas saturation plot at 26% CO_2 invasion of homogeneous domain: (Line source of CO_2 introduced at the bottom of the domain)

We see that CO_2 sweeps through the homogeneous medium as expected of invasion percolation (Figure 5-15). The spaces in between the CO_2 path are an artifact of the simulator configuration and do represent a uniformly rising front. The full-physics simulator allows CO_2 to migrate as a uniform front as the amount of variability in capillary entry pressures is nil in a homogeneous medium.

5.4.2 Leak in the seal rock in a homogeneous reservoir

We introduce two different rock types into the homogeneous medium: the seal rock and the reservoir rock. We impose a leak in the seal rock by initializing one cell in the seal rock with a very low P_{th} value at time t=0 and observe CO_2 migration patterns in the full-physics and invasion percolation simulators. Figure 5-16 is the threshold pressure map of the domain. The homogeneous reservoir rock is green in Figure 5-16. The seal rock is one layer thick near the top of the reservoir in red with a leakage spot in it represented by the blue cell.

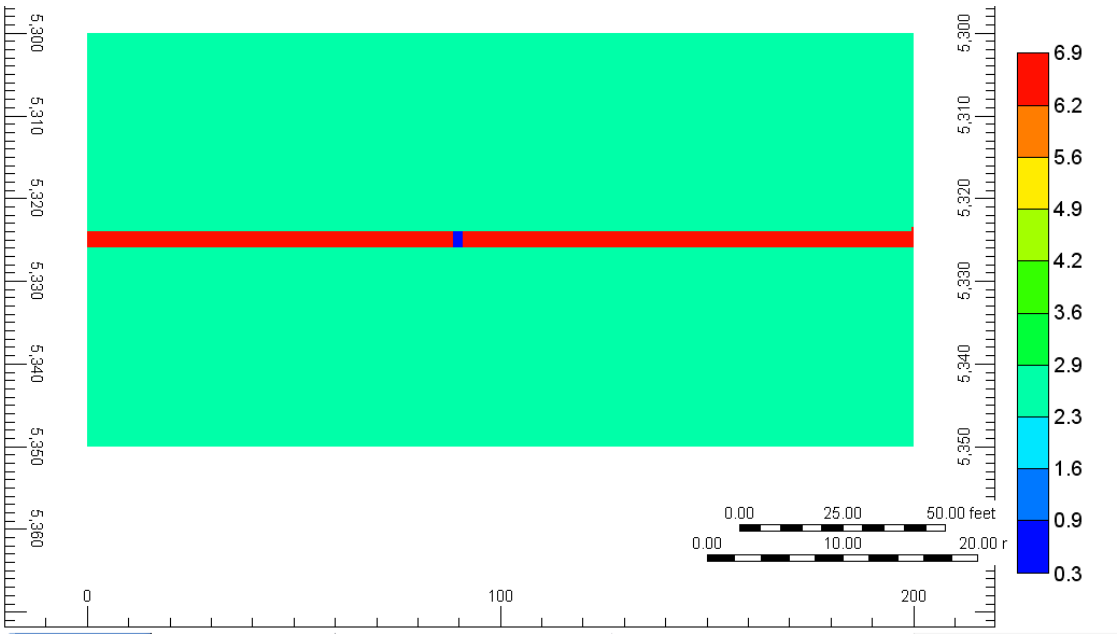

Figure 5-16: Threshold pressure map of the model domain

Parameter	Value
Model dimensions	60.9 m wide × 15.2 m tall (200 ft wide × 50 ft tall)
Grid cell dimensions	0.1524 m × 0.1524 m (0.5 ft × 0.5 ft)
Threshold pressure (reservoir)	16 kPa (2.3 psi); (single value)
Permeability (reservoir)	200 mD
Threshold pressure (seal)	47.4 kPa (6.87 psi)
Threshold pressure (leak point)	1.89 kPa (0.28 psi)
Porosity	47.6%
Connate water saturation, S_{wc}	20%
Critical oil saturation, S_{ocr}	2%
Flow boundary conditions	CLOSED
Density difference between CO_2 and brine	300 kg/m^3

Table 5-5: Input parameters for the model simulation of leakage through a seal rock

The CO_2 is sourced from the bottom center cell (point source) of the domain and allowed to migrate through the medium. Figure 5-17 gives the resulting gas saturation plot from both the simulation models. Figure 5-17 (b) gives the simulation result at percolation while Figure 5-17 (a) shows the gas saturation plot when CO_2 has invaded 4.2% of the model domain.

(a) Gas saturation plot at 4.2% invasion of model by CO_2: (Point source at bottom center cell of the domain)

Full-physics simulator result Invasion percolation simulator result

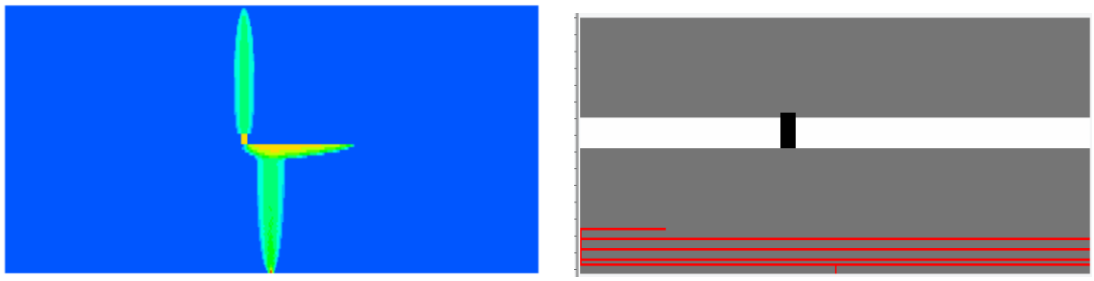

(b) Gas saturation plot at percolation: (Point source at bottom center cell of the domain)

Full-physics simulator result Invasion percolation simulator result

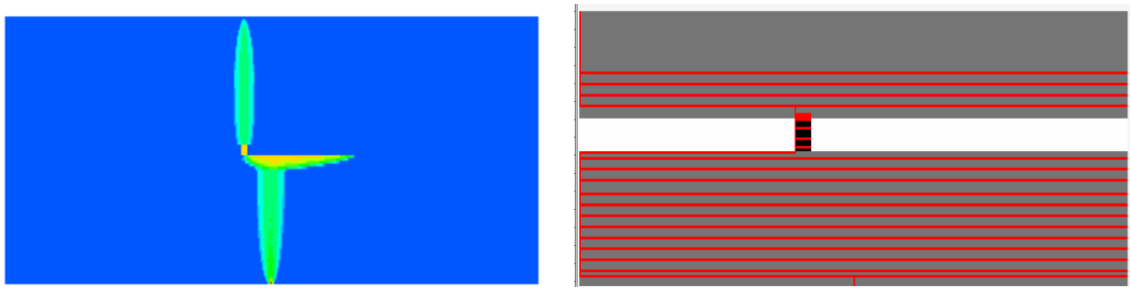

Figure 5-17: Gas saturation plot at 4.2% CO_2 invasion and percolation: (Point source of CO_2 introduced at the bottom center cell of the domain)

The point source case in the invasion percolation model traverses through the homogeneous reservoir uniformly. This is expected of invasion percolation. The full-physics simulator indicates a vertical pathway as CO_2 experiences no variability in capillary entry pressures that divert it laterally in the homogeneous medium. This represents the path of least resistance that CO_2 would pursue under a vertical bias.

5.4.3 Capillary channel flow in heterogeneous medium

This comparison case is for buoyancy-driven CO_2 migration in a heterogeneous medium. For reasonable computational effort, we chose a 40000-cell subsection (400 cells wide × 100 cells tall) randomly from the peel # 1 model as a test case. Table 5-6 gives the input parameters for this model. The permeability and porosity fields for the full-physics model are constant as these parameters are less dominant compared to the threshold pressure field for the capillary channel regime. The simulation models in both simulators were sourced with line source of buoyant CO_2 from the bottom of the domain and the simulation stopped when equal percentage of the domain was saturated by CO_2 (Figures 5-19 and 5-20). For this comparison case all the boundaries of the medium were closed.

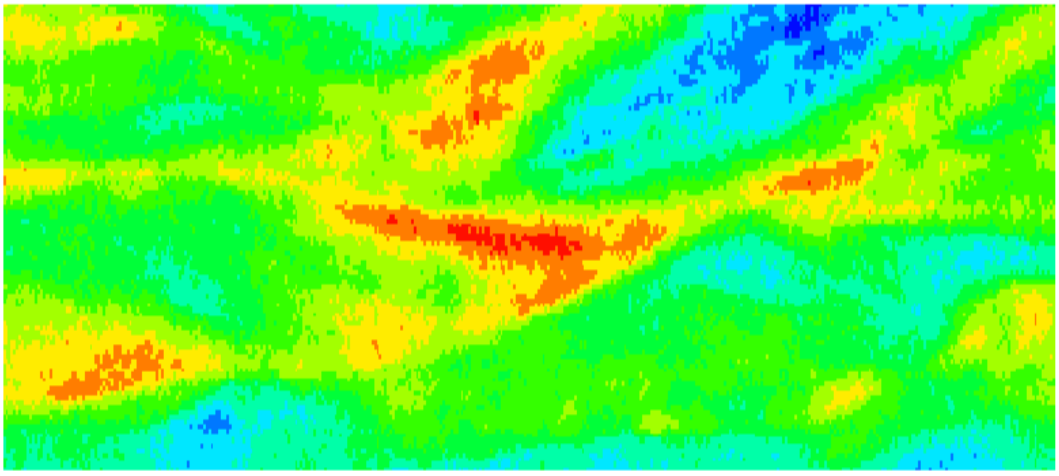

Figure 5-18: Threshold pressure map of the heterogeneous model domain (0.05 m tall × 0.2 m wide). The threshold pressure values increase as we move from cooler to hotter colors in the domain i.e. from 1.9 kPa in the darkest blue areas to 190 kPa in the darkest red areas.

Parameter	Value
Model dimensions	0.05 m × 0.2 m
Grid cell dimensions	5 mm × 5 mm (0.000164 ft × 0.000164 ft)
Threshold pressure	1.9-190 kPa
Permeability	2000 mD
Porosity	20%
Connate water saturation, S_{wc}	20%
Critical oil saturation, S_{ocr}	2%
Flow boundary conditions	CLOSED
Density difference between CO_2 and brine	300 kg/m^3
VOLMOD value for GEM model	2000

Table 5-6: Input parameters for the model simulations

Figure 5-19 gives the point source simulations in both the invasion percolation simulator and the full-physics simulator. Figure 5-20 gives the saturation pathways for the line source simulations.

Full-physics simulator result Invasion percolation simulator result

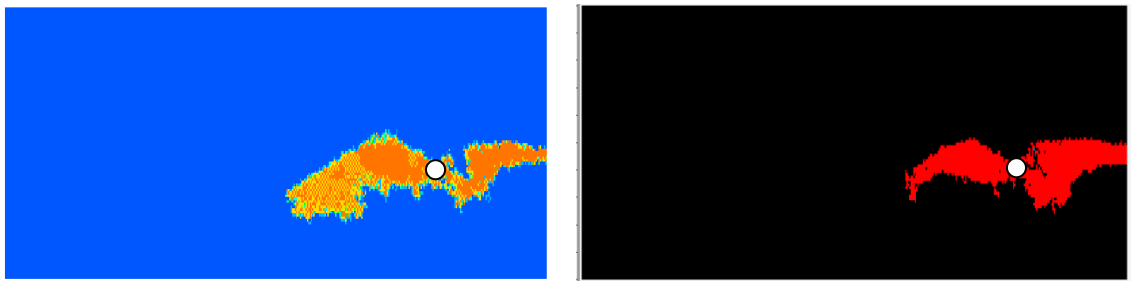

Figure 5-19: Gas saturation plot at 5% invasion of model by CO_2: Point source (white circle) at cell (251, 60) of the 0.05 m tall × 0.2 m wide domain

A 'volmod' value of 2000 is used in the point source simulation. The line source of CO_2, equivalent to the Permedia model, is defined using the 'volmod' keyword option in the

bottom row of cells in the GEM model domain. Figure 5-20 gives the resulting gas saturation plot for the line source scenario simulation. We find that both the simulators gave us qualitatively comparable results.

Full-physics simulator result

Invasion percolation simulator result

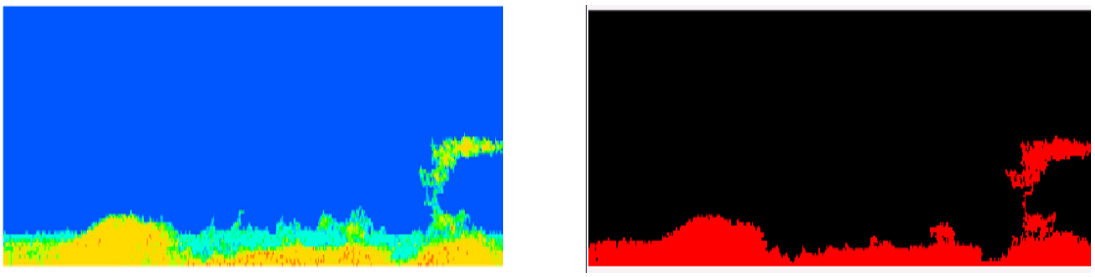

Figure 5-20: Gas saturation plot at 12% invasion of model by CO_2 i.e. both models are filled with 12% CO_2. Line source of CO_2 introduced at the bottom of the 0.05 m tall × 0.2 m wide domain.

The preferential paths that CO_2 follows agree in both the simulations. Hence we confirm that invasion percolation is a satisfactory method for simulating buoyant migration in heterogeneous domains. Hence, invasion percolation explains the physics of fluid migration with sufficient accuracy that we can take advantage of this much faster run time.

5.4.4 Comparison of capillary channel flow in media of varying heterogeneity

We perform the analogous exercise of section 5.1.2 to corroborate results of the invasion percolation models with the full-physics simulation models. For reasonable computational effort and simplistic comparison case, we chose a 64 cells wide × 64 cells tall (2 mm × 2 mm cells) 2D geostatistical model fabric (subsection of Fabric (C) in Figure 4-1). A set of simulation runs for progressively higher values of σ_{Pth} (wider frequency distributions of entry pressure) for threshold pressure distribution with $<P_{th}>$ = 10 kPa is shown in Figure 5-21. The simulation models in both simulators were sourced with line source of buoyant CO_2 from the bottom of the domains and the simulation

stopped when CO_2 percolated through to the top of the model domain. For this comparison case all the boundaries of the medium were closed in both the IP models and the full-physics simulation models.

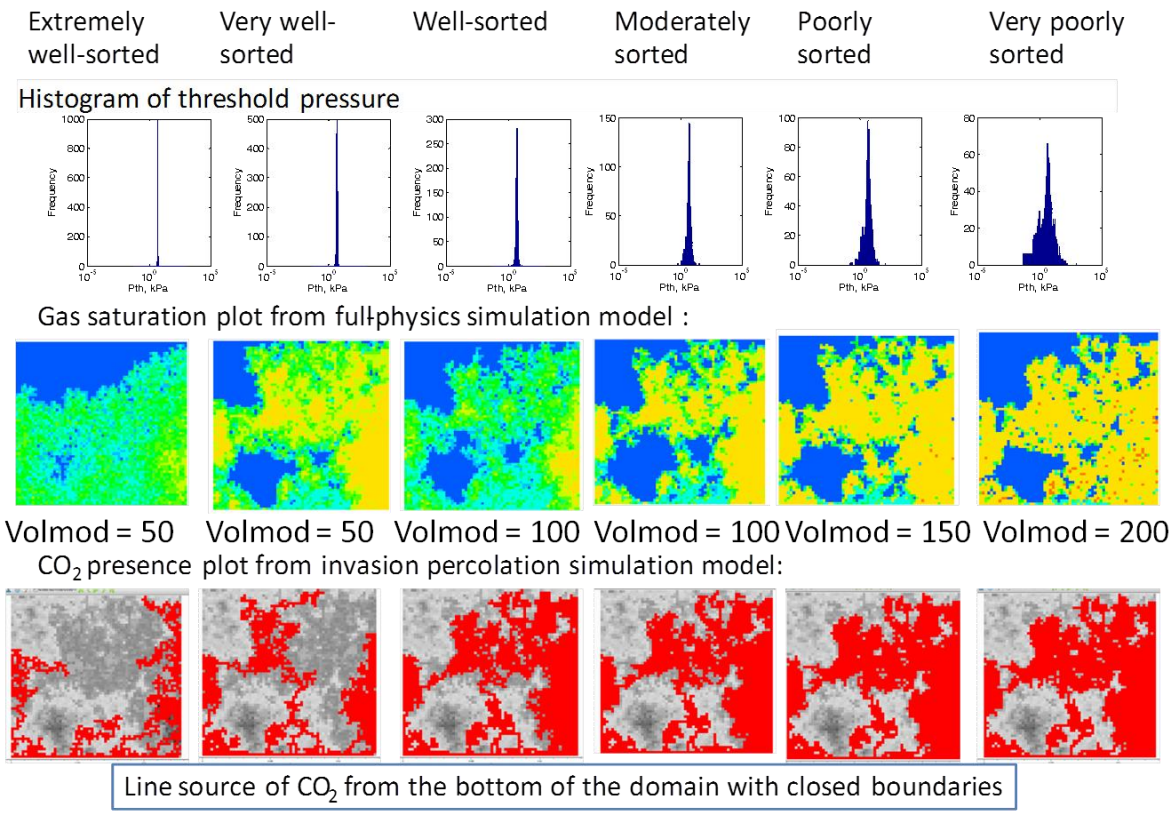

Figure 5-21: Invasion percolation (using Permedia®, bottom row) versus full-physics simulations (using GEM®, middle row) of CO_2 migrating within domains having the same mean entry pressure (= 10 kPa) with progressively wider frequency distributions of entry pressure (left to right). Continuous line source was placed at bottom boundary of model domains and allowed to migrate until percolation; boundaries of the model are closed.

We see that the simulators give qualitatively similar results for the displacement patterns in sufficiently heterogeneous media (moderately sorted or worse). For the relatively homogeneous media (well-sorted or better), the saturation structure in the full-physics

simulation is much more diffuse than in the invasion percolation simulation. Fingering patterns thus observed in the relatively homogeneous invasion percolation models are subject to future study for validating whether they are physically realistic.

The relevant forces acting upon the system are the capillary entry pressure gradients and the saturation gradients. We expect the governing dynamics of the capillary channel flow regime to vary depending on the relative weight of these different forces. For relatively homogeneous media, invasion percolation fails to capture the full physics of buoyancy-driven migration when the displaced phase must move countercurrently (the countercurrent motion is required in the full physics simulations because the domain boundaries are closed). It remains to be seen what happens with open boundaries. For sufficiently heterogeneous media, these governing forces are effectively captured by the IP models. Our IP models however, do not consider saturation gradients which would be overcome by the capillary forces in such media. The difference between the simulation results for relatively homogeneous media can be validated considering native brine moving countercurrently to the rising CO_2. In a relatively homogeneous medium the relative difference in P_{th} values between gridblocks is small and hence invasion percolation simulators vertically bias flow paths to percolation without exploring much rock pore volume. The full-physics simulators on the other hand, result in more diffuse and uniform CO_2 saturation paths as the saturation gradients would dominate over the comparatively weaker capillary forces in the relatively homogeneous rock. The mass of CO_2 is thus split in different directions without any overriding directional bias and moves in a more uniform front. Further study is required to validate results in these domains.

Figure 5-22 gives a summary plot of the simulated versus the IP model predicted values of % invasion of the domain at percolation. The data points are a compilation of Figure 5-21 (GEM versus Permedia results), Figure 5-5, 5-8 and 0.4 m × 0.4 m sub-sections of peels # 1 and # 2.

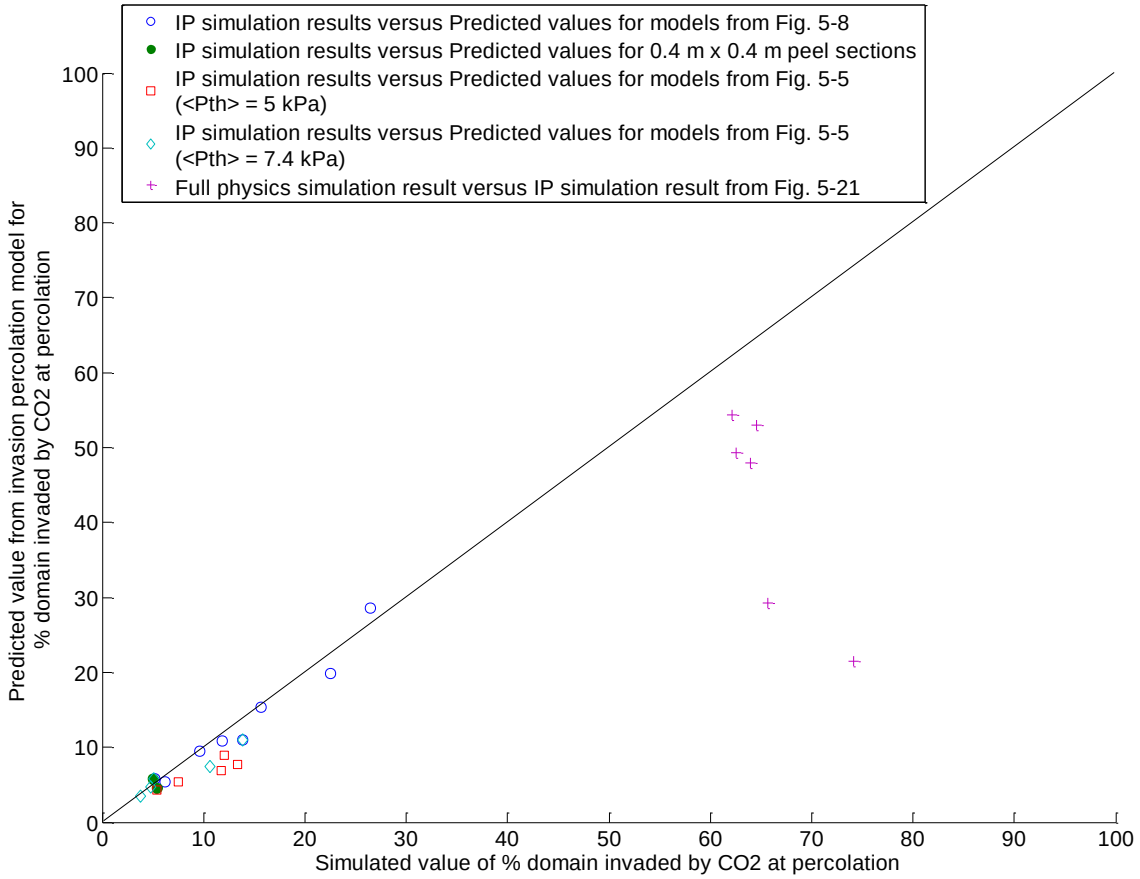

Figure 5-22: Comparison plot of full-physics simulated values of % invasion versus % invasion values of CO_2 at percolation predicted by the IP predictor model in the capillary channel regime. The IP simulations match reasonably with the predicted values for small to moderate extents of invasion (blue and green circles). The predicted % invasion values lie within 1.15 × simulated % invasion values. The full-physics simulation results deviate significantly from the IP model predictions for relatively homogeneous media (magenta cross datapoints). None of the IP predictor range extends to >60% invasion so the lack of agreement for the magenta crosses is not surprising and will require further investigation.

The capillary channels of CO_2 in the natural peel sections are adequately represented by invasion percolation physics. For our sufficiently heterogeneous small-scale domains, the invasion percolation approach captures the relevant physics with much less

computational effort. It is therefore valuable for understanding small-scale migration behaviour of fluids in heterogeneous media.

However, for relatively homogeneous media we find the IP simulations predicting a disperse capillary fingering pattern with minimal rock-fluid contact while the full-physics simulations reveal a very compact CO_2 front. This stark difference needs to be investigated in terms of the governing physics to ensure the saturation patterns reflect realistic behaviour.

6) 3-D MODELS

6.1 Simulating capillary channel flow in 3-D

In the previous sections we analyzed capillary channel flow of carbon dioxide in 2-D porous media. Real geologic media however exist in three dimensions. For more relevance our lessons learnt from the simple observed 2-D capillary channel flow should be tested in 3-D. Extrapolating capillary channel flow behavior in three dimensions is very helpful when we apply it to basin scale analysis for storage effectiveness of reservoirs to be considered for large-scale sequestration. In this chapter, we introduce 3-D invasion percolation models. We compare migration patterns in 3D using CMG and 'mesh' models in Permedia® here.

6.2 3-D model attributes

6.2.1 3-D mesh models in Permedia®

Permedia® has a tool option to include the pressure and temperature profiles in the reservoir, fluid PVT properties with the capillary pressure and relative permeability curves, permeability distribution and other rock properties for each point in the reservoir by converting the domain into a mesh of points. The 'mesh' models are thus more complex but can still be run as percolation models.

We generate mesh models along with the FID-PAR models in three dimensions to examine CO_2 channels. We benefit by using mesh models for the 3-D cases more tools are available to analyze the mesh model output files to help us in detailed quantitative analyses. This facilitates comparison of Permedia fluid saturations to the full-physics GEM models. CO_2 can be sourced into the 3-D Permedia® models as a point source, line source or a planar source (where the entire bottom horizontal plane in the model is sourced with CO_2).

6.2.2 3-D aquifer models exported from Permedia® into GEM

The threshold pressure, permeability, connate water and critical oil saturations, pressure and temperature conditions and other rock and fluid properties can be exported from Permedia® meshes into GEM. Care should be taken to read data from the exported Permedia® dataset into GEM after reorienting the model according to the appropriate co-ordinate directions. The models can be visualized in both the simulators to verify if they are oriented the same.

The sourcing options for the equivalent 3-D GEM models could be for a point, line or the entire plane as well. We enable source cells in GEM using the 'volmod' keyword option or the block of large saturation of CO_2 option to match the Permedia® source type as in the 2-D cases. Sourcing the CO_2 into the model domain using an injection well is to be explored as part of future work.

We simulate a 3D model with the depositional fabric of the peel as an example case. The peel fabric is a realistic representation of natural spatial correlation in porous media. However the peels are quasi-2D specimen. We stack the peel model along the Y-axis as shown in Figure 6-1 to obtain a 3-D domain. This model yields a fair case study of capillary channel flow in 3-D with realistic depositional fabric.

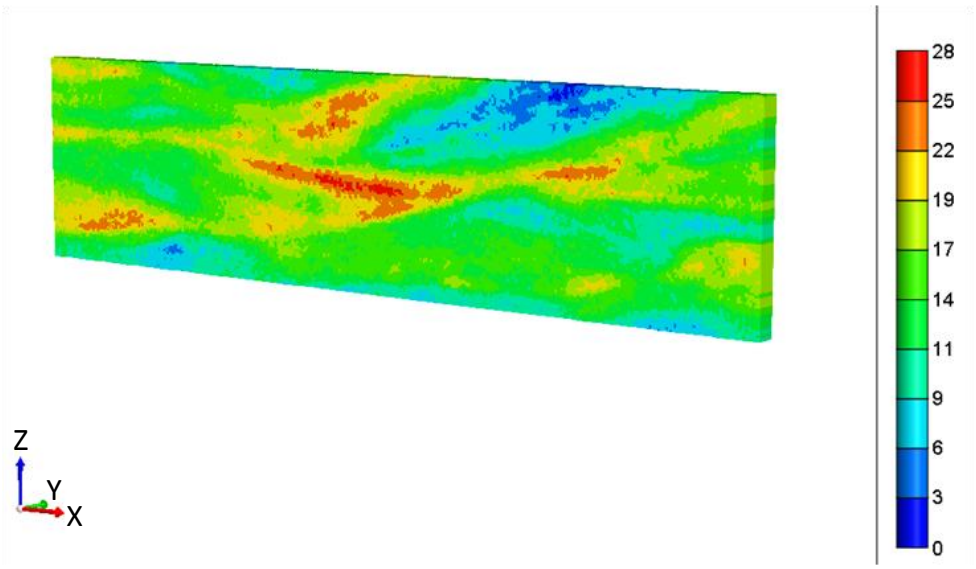

Figure 6-1: Threshold pressure map of the peel replicated 10 times in the direction of the Y-axis to generate a 3-D domain. The domain consists 400 × 10 × 100 cells that are 2 mm × 2 mm × 2 mm each. The colorbar indicates the threshold pressure values in the domain (in psi).

Table 6-1 gives the input data used to define the simulation model. The model simulation uses inputs for other rock and fluid properties (like rock compressibility, PVT properties etc.) from simulation models generated in Saadatpoor (2009).

Parameter	**Value imported from Permedia®**
Grid cell dimensions	2 mm × 2 mm × 2 mm
Threshold pressure	1.9 - 190 kPa
Permeability	2000 mD
Porosity	20%
Connate water saturation, S_{wc}	20%
Critical oil saturation, S_{ocr}	2%
Flow boundary conditions	CLOSED
Depth from datum	1615.44 m

Density difference between CO_2 and brine	300 kg/m^3
GEM model CO_2 source	Bottom 15 rows of domain: large saturation block of CO_2 as a planar source

Table 6-1: Input properties for the 3-D mesh model with peel # 1 depositional fabric

We simulate capillary channel flow of planar source of CO_2 (large saturation block in bottom 15 rows) in the full-physics simulator (GEM model). Capillary channel flow in this domain should theoretically be the equivalent projection of the 2-D invasion patterns of CO_2 along the Y-axis. Figure 6-2 gives the saturation plot of CO_2 in this full-physics simulation. The 3-D saturation distribution is 'disperse' with the evolution of major percolation pathways as seen in Figure 6-2. The saturation distribution in any Y- slice is the projection of any single Y-slice as expected.

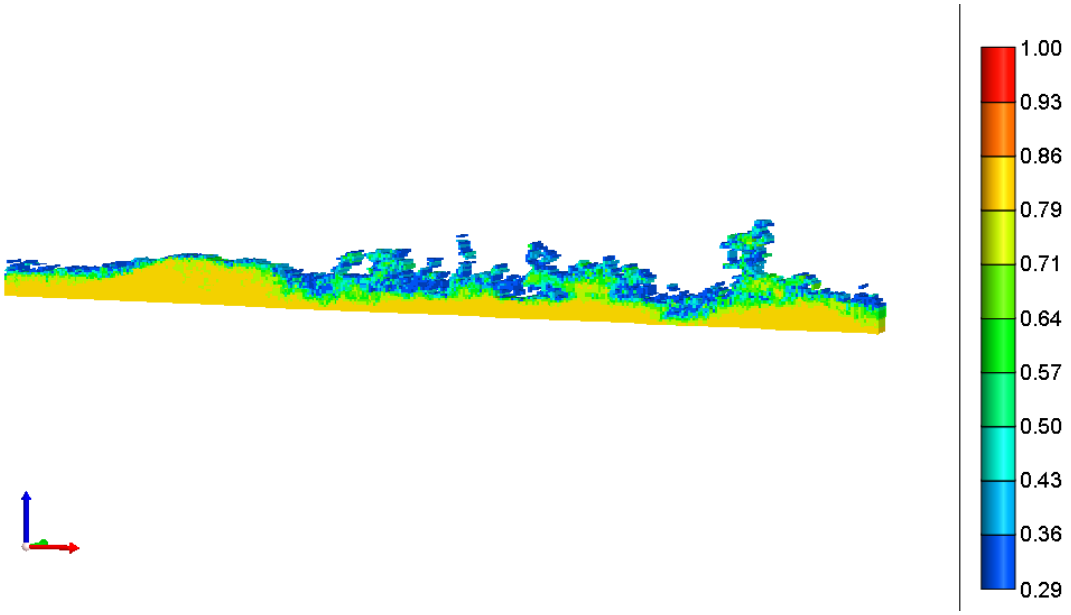

Figure 6-2: Saturation plot of 3-D mesh model in full physics simulator (GEM) with peel # 1 depositional fabric. Planar source of CO_2 is introduced in 15 planes from the bottom of the model domain. The boundaries of the model are closed. The color legend to the right represents the CO_2 saturation values.

6.3 3-D model simulations: comparing capillary channels in IP and full-physics simulation models

6.3.1 Geostatistical 3-D model simulations

We created larger 3-D geostatistical model domains with known correlation length of threshold pressure in the 3 principal directions. Table 6-2 gives the input data for generating the geostatistical model 1 in the 'FFT Simulation' tool. Figure 6-3 depicts the model domain thus obtained.

Parameter	Value
Correlation length in x direction, m	3.048
Correlation length in y direction, m	3.048
Correlation length in z direction, m	3.048
Cell dimension, $dx = dy = dz$, m	0.3048
Mean, $< P_{th} >$, kPa	10
Standard deviation of $\ln(P_{th})$	1.85

Table 6-2: Stochastic input parameters for generating geostatistical 3-D model 1 (as in Saadatpoor et. al, 2009)

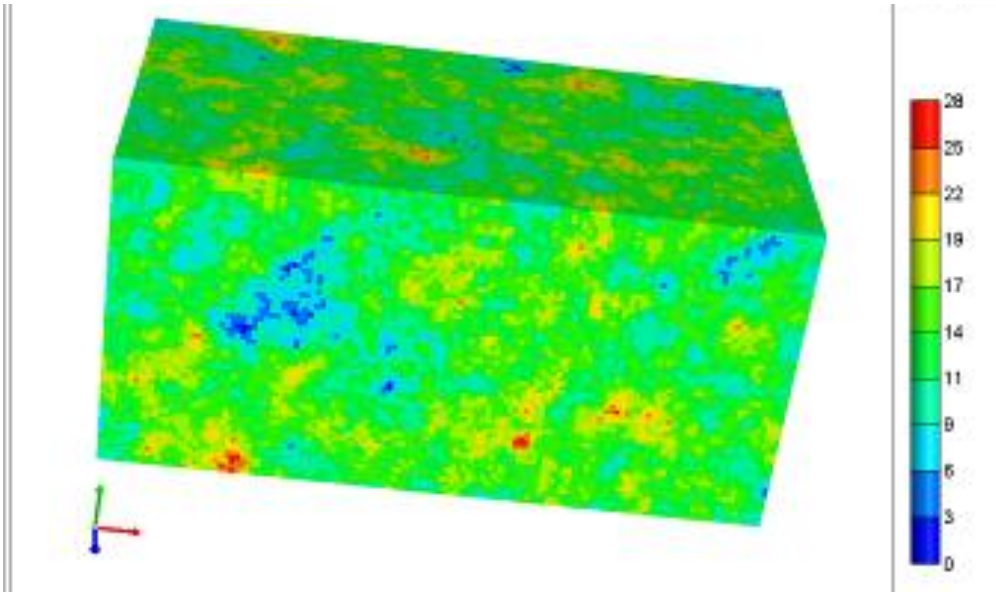

Figure 6-3: Threshold pressure map of 3-D geostatistical model 1. Range of threshold pressure values in the medium, in psi, are shown in the colorbar to the right.

Parameter	**Value imported from Permedia®**
Model dimensions (L × W × H)	39.0144 m × 19.5072 m × 19.5072 m
Grid cell dimensions	0.3048 m × 0.3048 m × 0.3048 m
Threshold pressure	0.19 - 99 kPa (~0.03 -14.5 psi)
Permeability	0.0161 - 161 mD
Porosity	0.1-0.26
Connate water saturation, S_{wc}	20%
Critical oil saturation, S_{ocr}	2%
Flow boundary conditions	CLOSED
Depth from datum	1615.44 m
Density difference between CO_2 and brine	300 kg/m^3
GEM model CO_2 source	Bottom 15 rows of domain: large saturation block of CO_2 as a planar source

Table 6-3: Input properties for the 3-D mesh model 1 (geostatistical simulation)

Planar source of CO_2 is introduced from the bottom plane of the model domain. In both the simulators, the boundaries of the model are closed. Figure 6-4 gives the resulting gas saturation pathways for the simulation models run to percolation.

a) Full-physics simulator result

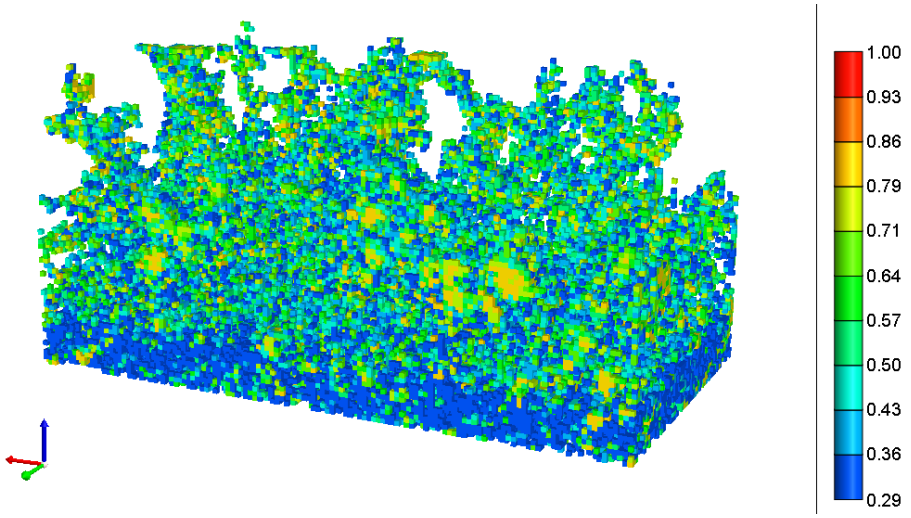

b) Invasion percolation simulator result

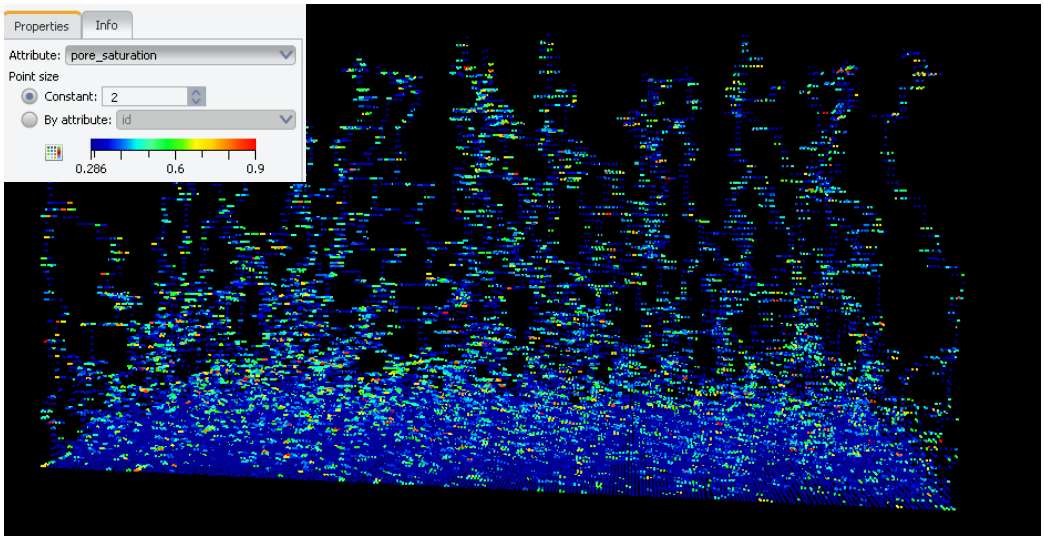

Figure 6-4: Saturation plot of 3-D mesh model 1 in (a) GEM and (b) Permedia with peel # 1 depositional fabric. Planar source of CO_2 is introduced from the bottom 15 plane of

the model domain and allowed to migrate through the domain until percolation. Both the simulators yield qualitatively similar network of fingering structures that percolate through to the top of the domain. Colorbar in (a) and (b) gives the saturation of CO_2.

Both the models give similar dense network of fingers progressing to the top boundary of the model. Thus we establish qualitative similarity of capillary channels in sufficiently heterogeneous 3-D domains.

We perform another comparison case on a more homogeneous domain with more horizontal correlation. Table 6-4 gives the input data for generating the geostatistical model 2 in the 'FFT Simulation' tool. Figure 6-5 depicts the model domain obtained.

Parameter	**Value**
Correlation length in x direction, m	9.7536
Correlation length in y direction, m	3.048
Correlation length in z direction, m	1.524
Cell dimension, $dx = dy = dz$, m	0.3048
Mean, $< P_{th} >$, kPa	10
Standard deviation of $\ln(P_{th})$	1.75

Table 6-4: Stochastic input parameters for generating geostatistical 3-D model 2 (as in Saadatpoor et. al, 2009)

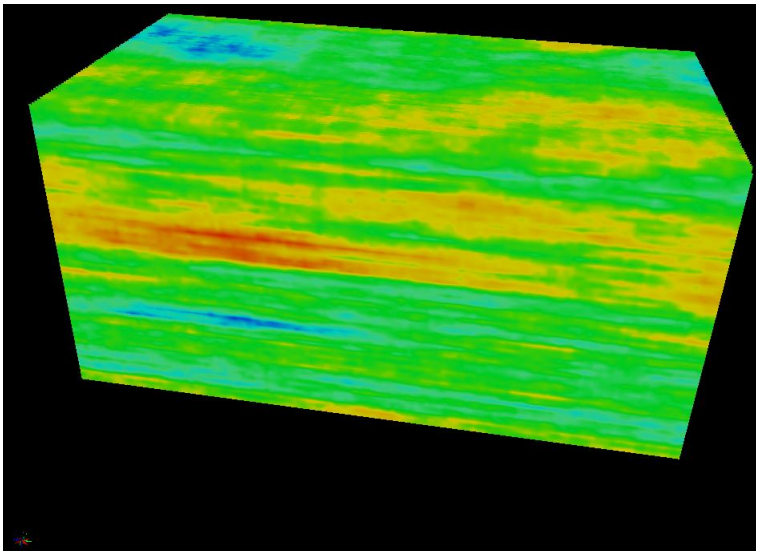

Figure 6-5: Threshold pressure map of the 3-D geostatistical model 2. Model is 39.0144 m × 19.5072 m × 19.5072 m. Threshold pressure values in the medium increase from 4 kPa in the darkest blue regions to 8 k Pa in the darkest red regions.

Parameter	**Value imported from Permedia®**
Model dimensions (L × W × H)	39.0144 m × 19.5072 m × 19.5072 m
Grid cell dimensions	0.3048 m × 0.3048 m × 0.3048 m
Threshold pressure	4 - 8 kPa (0.58 - 1.16 psi)
Permeability	40- 160 mD
Porosity	0.22-0.26
Connate water saturation, S_{wc}	20%
Critical oil saturation, S_{ocr}	2%
Flow boundary conditions	CLOSED
Depth from datum	1615.44 m
Density difference between CO_2 and brine	300 kg/m^3
GEM model CO_2 source	Bottom 2 rows of domain: saturation block of CO_2 as a planar source

Table 6-5: Input properties for the 3-D mesh model 2 (geostatistical simulation).

Planar source of CO_2 is introduced from the bottom plane of the model domain. In both the simulators, the flow boundaries of the model are closed. Figure 6-6 gives the resulting gas saturation pathways for the simulation models run to percolation.

a) Full-physics simulator result (GEM)

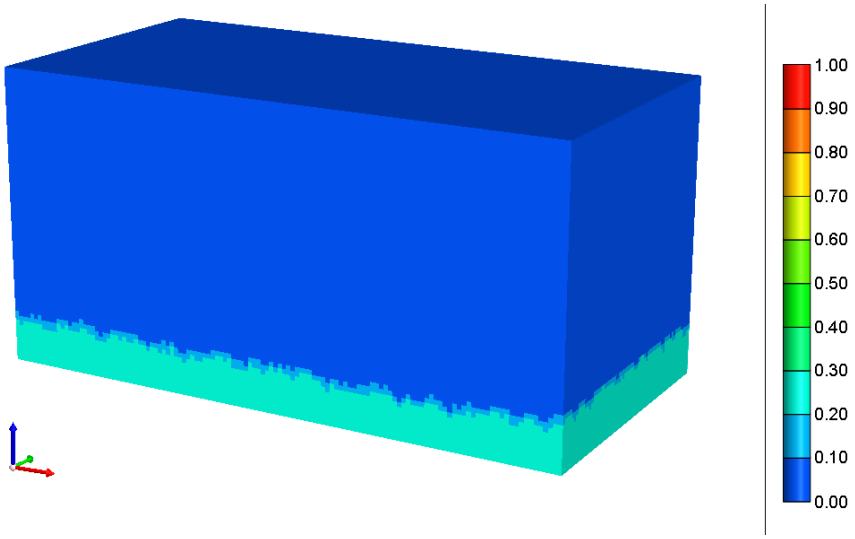

b) Invasion percolation simulator result (Permedia®)

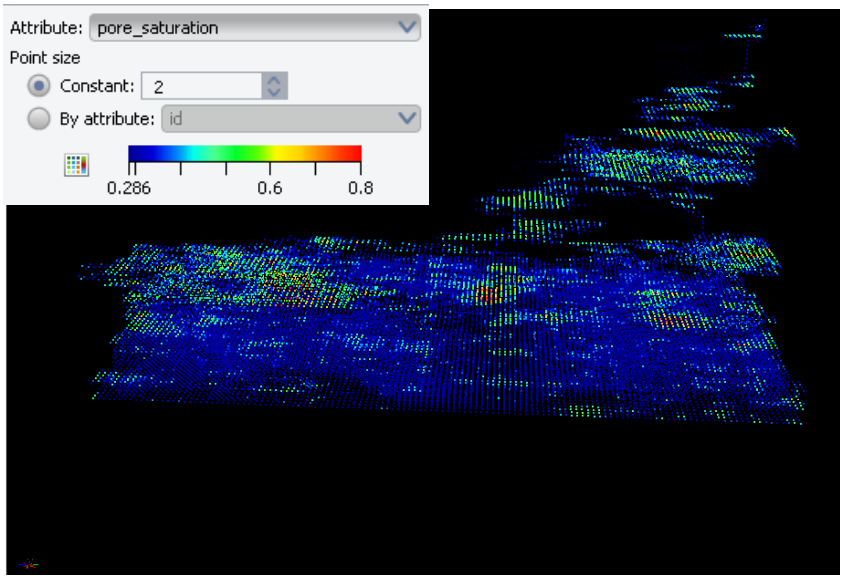

Figure 6-6: Saturation plot of 3-D mesh model 2 in (a) GEM and (b) Permedia. Planar source of CO_2 is introduced from the bottom plane of the model domain and allowed to

migrate through the domain until percolation. GEM simulation shows CO_2 at the end of 100 years at residual saturation (cyan color) invading about 25% of the model domain. The colorbar in (a) gives the CO_2 saturation values. The IP simulation model shows CO_2 invasion patterns at percolation in (b).

This more homogeneous model 2 gives two very different capillary invasion patterns in the two simulators. Invasion percolation fails to capture the full physics in this case. The IP model gives CO_2 migrating through the lower P_{th} regions and accumulating beneath the capillary barriers in the medium. The full-physics simulator on the other hand gives a compact front following the permeability field in the domain. Each of these patterns has diametrically opposite implications on the efficiency of rock-fluid contact after sequestration in the storage reservoir. We need to explore such relatively homogeneous media to better understand which physics is appropriate to consider.

7) CONCLUSIONS

Expected storage efficiency and plume migration behavior in heterogeneous rock differ greatly from pressure gradient driven flow wherever viscous forces are negligible compared to buoyancy forces. This research was performed with the main objective of studying the dynamics of capillary channel flow in CO_2 bulk phase storage. As a valuable starting point, we explore the capillary channel flow regime of buoyant CO_2 in small-scale, high resolution heterogeneous media. Understanding migration behavior at the small-scale can help us approach the problem of upscaling better and hence define the complex plume dynamics at the reservoir scale more realistically. Capillary channel flow is observed only if the simulation accounts explicitly for the heterogeneous distribution of threshold pressures of the rock at a geologically-representative scale (Saadatpoor *et al.*, 2009, Luo *et al.*, 2008 and Hermanrud *et al.*, 2010).

Capillary channel flow regime reduces effective fluid-rock contact compared to compact flow regime. The transition between the two extreme flow patterns of fingering and back-filling in the IP models is a function of the threshold pressure distribution of the rock, correlated with the depositional resolution of the domain and the density contrast between CO_2 and connate water. Barely 1-2% of the domain was invaded by capillary fingers while back-filling structures invaded up to 40% of the small-scale invasion percolation model domains we studied. The more capillary barriers there are for the buoyant fluid, the better the effective rock-fluid contact volume in the rock. Lower density contrast between CO_2 and native brine also aids in more homogeneous and denser CO_2 saturation in the rock.

In sufficiently heterogeneous reservoirs (threshold pressures vary by a factor of 10 or more) with properties conducive to back-filling, namely longer horizontal correlation lengths and wider grain size distributions, rising CO_2 contacts a greater fraction of the reservoir. Invasion percolation simulation models give qualitatively similar results in both 2-D and 3-D compared to full-physics simulators for sufficiently heterogeneous

domains. We observe fingering occurring in relatively homogeneous media in our percolation models. Fingering results in minimal rock-fluid contact volume and is thus undesirable in sequestration. However this regime is contradicted by the full-physics simulation models in which the CO_2 moves as a compact front. Hence these domains (in both 2-D and 3-D) require further study to determine the physics governing this situation.

The threshold pressure frequency distribution (mean and standard deviation of threshold pressures assigned to each element of the domain) and the anisotropy of the medium (ratio of correlation length of threshold pressures in the horizontal and vertical directions) influence the 'efficiency function' that determines the extent of rock-fluid contact and the characteristic saturation pathways in a given geologic environment. Geostatistical depositional fabrics influence capillary channels of CO_2 in a similar fashion to natural sedimentologic fabrics. Our results indicate the possibility of predictive ability for expected flow patterns when the spatial and frequency distribution of the threshold pressures in the medium are known.

8) FUTURE WORK

8.1 Physics of buoyant migration in homogeneous reservoirs

The capillary channels of CO_2 in the natural peel samples are governed by invasion percolation physics. For our sufficiently heterogeneous small-scale domains, the invasion percolation approach captures the relevant physics with much less computational effort. However, for relatively homogeneous media we find the IP simulations predicting a disperse capillary fingering pattern with minimal rock-fluid contact while the full-physics simulations reveal a very compact CO_2 front. This stark difference needs to be investigated in terms of the governing physics to ensure the saturation patterns reflect realistic behaviour. We need this to establish a firm understanding for the entire spectrum of migration behavior in the subsurface.

8.2 Effect of potential gradient on capillary channels of CO_2

Future work involving pressure gradient analysis is also relevant as the external pressure gradient or potential gradient is an important driver influencing CO_2 movement near the wellbore. Rocks of varying degrees of heterogeneity under the buoyancy gradient with negligible viscous forces have been studied in this work. Going forward, we can explore how these same rocks would behave under the influence of different potential gradients as we move closer to the injection wellbore.

Integrating the effect of the potential gradient with the effects of threshold pressure distribution ($<P_{th}>/ \sigma_{Pth}$), and the density difference between CO_2 and native brine established in this work would better define the 'efficiency function' that determines the effective storage capacity of any reservoir. Furthermore, accounting for anisotropy of the rock would be a useful subsequent step.

8.3 3-D Models with injection of CO_2

We can also work on integrating the modeling to investigate the CO_2 plume movement at the reservoir scale from injection till migration at capillary equilibrium. This would help

us visualize the relevance of the observed capillary channel regime for reservoir scale migration.

A sample simulation run in 3-D is shown in Figure 8-1 that depicts the cross-over from the compact flow regime to the capillary channel flow regime.

1. CO_2 Injection phase:

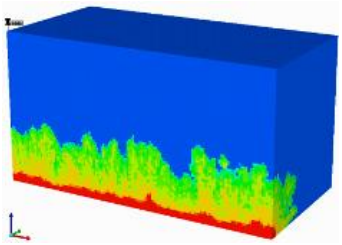

2. CO_2 Migration phase:

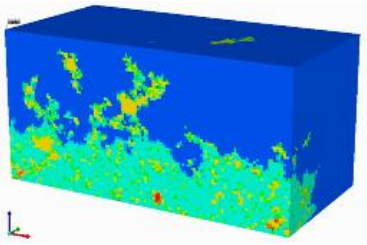

Figure 8-1: GEM simulation showing compact flow regime during injection and capillary channel flow regimes during the migration phase in a heterogeneous formation. The domain is injected with CO_2 at 0.5 bbl/day for one year from a horizontal well along the front-facing edge of the domain as shown. The CO_2 migration pattern is captured at the end of 25 years. The domain is 128 ft × 64 ft × 64 ft with 1 ft × 1 ft × 1 ft gridblocks.

APPENDIX A

Elevation data -> grain size -> threshold pressures:

The ranged elevation measurements are saved in a .mat file (priya_data.mat). These elevation measurements are correlated with grain diameters and hence the topography is converted to the threshold pressure map of the peel # 1 model domain. The grain diameters are linearly associated to the measured topography for our peel specimen. The most imbibition occurs in region with smallest measured grain size and hence the highest elevation measurement and vice-versa. Linear interpolation gives the grain size distribution. The threshold pressure distribution is calculated from the grain diameters using equation 3-2 (Berg, 1975).

```
clear all
close all
%Using priya_data.mat
cd ('C:\Documents and Settings\pr7388\Desktop\Pri_work_data\Work\Data
and calculations')
%priya_data.mat consists of full peel # 1 data points (elevation
measurements X, Y, Z)
load priya_data.mat

d = Z_corrected;
%Maximum elevation measured
dma = max(d);
%Minimum elevation measured
dmi = min(d);
%Maximum grain diameter measured, mm
gma = 0.08;
%Minimum grain diameter measured, mm
gmi = 0.065;

%Plot histogram of elevations measured on the peel # 1
figure()
hist(d);
title ('Histogram of ranged elevation measurements, mm','fontsize',16);
xlabel('Ranged elevation measured, mm','fontsize',16);
ylabel('Frequency','fontsize',16);

dmm = zeros(size(d));

for i = 1: 1 : length(d)
    dmm(i) =(gma*(d(i)-dma)/(dmi-dma))+(gmi*(d(i)-dmi)/(dma-dmi));
```

```
    % Linear interpolation: y2 = y0(x2 - x1)/(x0 - x1) + y1(x2 -
x0)/(x1 - x0)
end

%Plot histogram of grain diameters
figure()
hist(dmm);
title ('Histogram of grain diameters, mm','fontsize',16);
xlabel('Grain diameter, mm','fontsize',16);
ylabel('Frequency','fontsize',16);

%Using Berg, 1975 to evaluate Pth in kPa from grain diameters
pth = 16.3*30e-3./dmm;

%Plot histogram of threshold pressures
figure()
hist(pth);
title ('Histogram of threshold pressures, kPa','fontsize',16);
xlabel('Threshold pressure, kPa','fontsize',16);
ylabel('Frequency','fontsize',16);
```

The histograms generated for peel # 1 are given below:

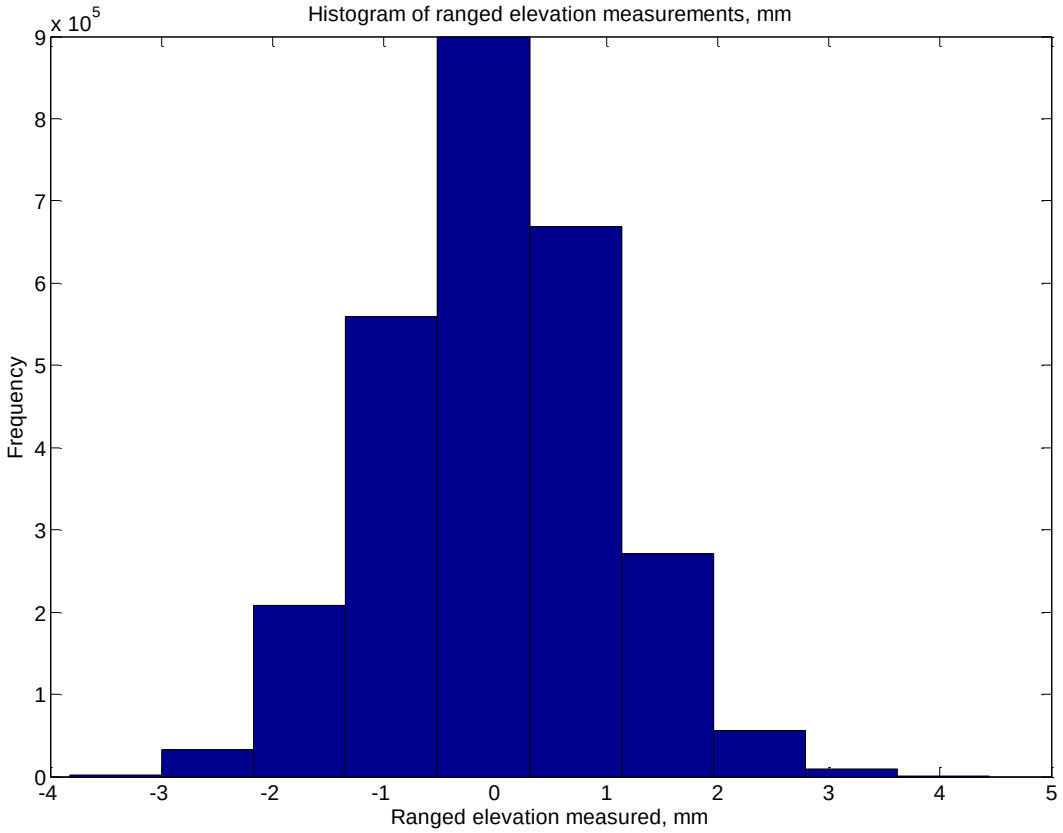

Figure A-1: Normal distribution of ranged elevation measurements on peel # 1

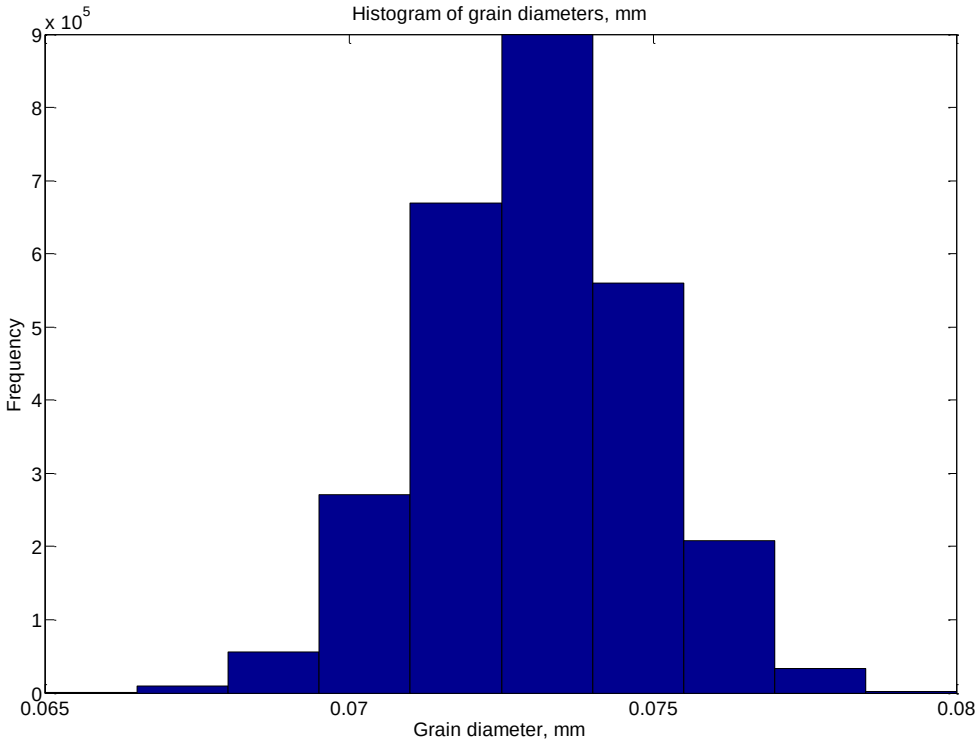

Figure A-2: Normal distribution of grain diameters on peel # 1

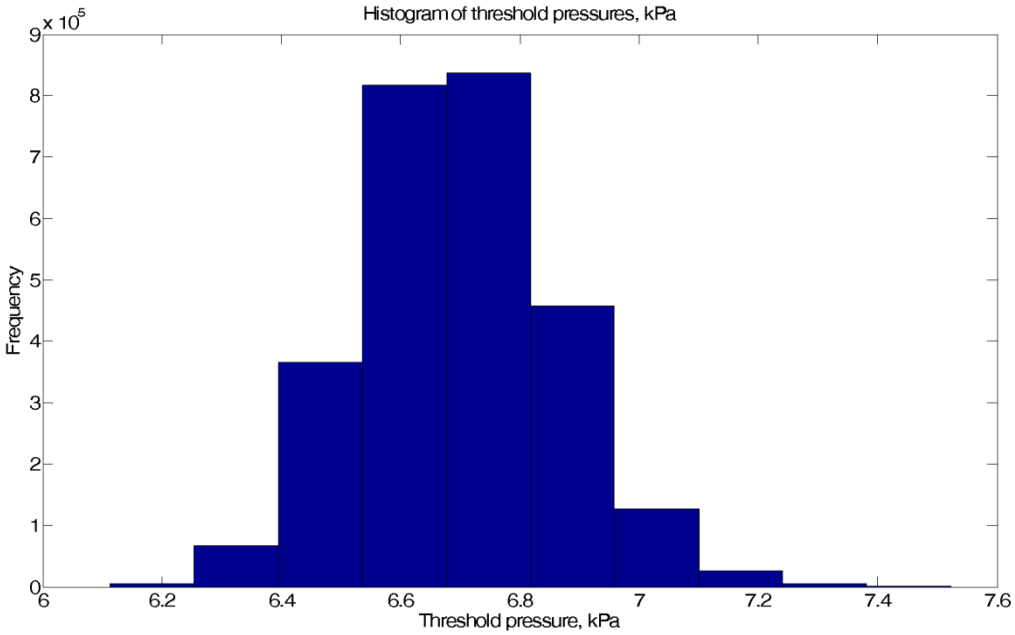

Figure A-3: Lognormal distribution of threshold pressures in peel # 1

Simulation results for Figure 5-10

The data from the simulation results for Figure 5-10 is given below. The input parameters for these cases i.e. threshold pressure field properties and fluid density contrast assumed for the simulation cases are shown in the table below. The effect of threshold pressure range is studied using the 54 different samples from Figure 4-4. The sensitivity analysis is performed on different background depositional fabrics: geostatistical model fabrics (A), (B) and (C). Correlation length of threshold pressure in horizontal and vertical directions in terms of number of cells is known for all fabrics. Line source of CO_2 is allowed to migrate through the model domain with periodic lateral flow boundaries for all cases. The percentage of the model domain invaded by CO_2 is shown for each simulation case.

Table A-1 below gives the data used in the thesis for analysis (Figures 5-10 and 5-11).

Model name	<Pth>, kPa	σPth, kPa	<Pth>/σPth	% model invaded by CO2 at percolation	1/(del rho g), m/ kPa	Vertical correlation length/dz (in terms of # of cells)	Revised vertical correlation length/dz	Horizontal correlation length/dz	Horizontal correlation length/revised vertical correlation length	Comments
EWUCSa	0.582	0.0133	43.7593985	3.163375	0.339789331	0.005	1	100	100	Fabric (A); Extremely well sorted upper coarse sand
VWUCSa	0.582	0.038	15.31578947	5.3937	0.339789331	0.005	1	100	100	Fabric (A); Very well sorted upper coarse sand
WUCSa	0.583	0.074	7.878378378	8.19895	0.339789331	0.005	1	100	100	Fabric (A); Well sorted upper coarse sand
MUCSa	0.594	0.165	3.6	12.585125	0.339789331	0.005	1	100	100	Fabric (A); Moderately sorted upper coarse sand
PUCSa	0.622	0.337	1.845697329	16.4601	0.339789331	0.005	1	100	100	Fabric (A); Poorly sorted upper coarse sand
VPUCSa	0.743	1.406	0.528449502	21.450575	0.339789331	0.005	1	100	100	Fabric (A); Very poorly sorted upper coarse sand
EWLCSa	0.828	0.019	43.57894737	3.76855	0.339789331	0.005	1	100	100	Fabric (A); Extremely well sorted lower coarse sand
VWLCSa	0.828	0.055	15.05454545	6.976725	0.339789331	0.005	1	100	100	Fabric (A); Very well sorted lower coarse sand
WLCSa	0.83	0.105	7.904761905	9.611275	0.339789331	0.005	1	100	100	Fabric (A); Well sorted lower coarse sand
MLCSa	0.845	0.235	3.595744681	15.1183	0.339789331	0.005	1	100	100	Fabric (A); Moderately sorted lower coarse sand
PLCSa	0.886	0.48	1.845833333	19.615875	0.339789331	0.005	1	100	100	Fabric (A); Poorly sorted lower coarse sand
VPLCSa	1.058	2.001	0.528735632	24.8134	0.339789331	0.005	1	100	100	Fabric (A); Very poorly sorted lower coarse sand
EWMUSa	1.163	0.027	43.07407407	4.511125	0.339789331	0.005	1	100	100	Fabric (A); Extremely well sorted upper medium sand
VWMUSa	1.163	0.077	15.1038961	8.1818	0.339789331	0.005	1	100	100	Fabric (A); Very well sorted upper medium sand
WMUSa	1.166	0.148	7.878378378	12.324975	0.339789331	0.005	1	100	100	Fabric (A); Well sorted upper medium sand
MMUSa	1.188	0.33	3.6	17.859475	0.339789331	0.005	1	100	100	Fabric (A); Moderately sorted upper medium sand
PMUSa	1.245	0.674	1.847181009	22.4092	0.339789331	0.005	1	100	100	Fabric (A); Poorly sorted upper medium sand
VPMUSa	1.486	2.811	0.528637496	27.9264	0.339789331	0.005	1	100	100	Fabric (A); Very poorly sorted upper medium sand
EWMLSa	1.645	0.0375	43.86666667	5.52285	0.339789331	0.005	1	100	100	Fabric (A); Extremely well sorted lower medium sand
VWMLSa	1.645	0.1085	15.16129032	10.05695	0.339789331	0.005	1	100	100	Fabric (A); Very well sorted lower medium sand
WMLSa	1.649	0.209	7.889952153	14.76875	0.339789331	0.005	1	100	100	Fabric (A); Well sorted lower medium sand
MMLSa	1.679	0.467	3.595289079	20.622925	0.339789331	0.005	1	100	100	Fabric (A); Moderately sorted lower medium sand
PMLSa	1.76	0.953	1.84679958	25.366125	0.339789331	0.005	1	100	100	Fabric (A); Poorly sorted lower medium sand
VPMLSa	2.101	3.976	0.528420523	30.7213	0.339789331	0.005	1	100	100	Fabric (A); Very poorly sorted lower medium sand
EWFUSa	2.327	0.053	43.90566038	6.91225	0.339789331	0.005	1	100	100	Fabric (A); Extremely well sorted upper fine sand
VWFUSa	2.326	0.154	15.1038961	12.54655	0.339789331	0.005	1	100	100	Fabric (A); Very well sorted upper fine sand
WFUSa	2.332	0.295	7.905084746	16.990175	0.339789331	0.005	1	100	100	Fabric (A); Well sorted upper fine sand
MFUSa	2.375	0.66	3.598484848	24.04475	0.339789331	0.005	1	100	100	Fabric (A); Moderately sorted upper fine sand
PFUSa	2.489	1.348	1.846439169	28.484	0.339789331	0.005	1	100	100	Fabric (A); Poorly sorted upper fine sand
VPFUSa	2.972	5.623	0.528543482	34.298775	0.339789331	0.005	1	100	100	Fabric (A); Very poorly sorted upper fine sand
EWFLSa	3.279	0.075	43.72	8.07415	0.339789331	0.005	1	100	100	Fabric (A); Extremely well sorted lower fine sand
VWFLSa	3.279	0.216	15.18055556	15.006775	0.339789331	0.005	1	100	100	Fabric (A); Very well sorted lower fine sand

										Fabric (A);
WFLSa	3.287	0.416	7.901442308	20.237575	0.339789331	0.005	1	100	100	Well sorted lower fine sand
										Fabric (A);
MFLSa	3.347	0.93	3.598924731	26.314875	0.339789331	0.005	1	100	100	Moderately sorted lower fine sand
										Fabric (A);
PFLSa	3.508	1.9	1.846315789	31.11735	0.339789331	0.005	1	100	100	Poorly sorted lower fine sand
										Fabric (A);
VPFLSa	4.189	7.925	0.528580442	37.50195	0.339789331	0.005	1	100	100	Very poorly sorted lower fine sand
										Fabric (A);
EWVFUSa	4.653	0.106	43.89622642	9.726925	0.339789331	0.005	1	100	100	Extremely well sorted upper very fine sand
										Fabric (A);
VWVFUSa	4.652	0.307	15.15309446	17.99455	0.339789331	0.005	1	100	100	Very well sorted upper very fine sand
										Fabric (A);
WVFUSa	4.665	0.5904	7.901422764	23.075325	0.339789331	0.005	1	100	100	Well sorted upper very fine sand
										Fabric (A);
MVFUSa	4.75	1.32	3.598484848	29.4673	0.339789331	0.005	1	100	100	Moderately sorted upper very fine sand
										Fabric (A);
PVFUSa	4.979	2.696	1.846810089	35.0593	0.339789331	0.005	1	100	100	Poorly sorted upper very fine sand
										Fabric (A);
VPVFUSa	5.944	11.246	0.528543482	41.080075	0.339789331	0.005	1	100	100	Very poorly sorted upper very fine sand
										Fabric (A);
EWVFLSa	6.6025	0.1504	43.89960106	12.36245	0.339789331	0.005	1	100	100	Extremely well sorted lower very fine sand
										Fabric (A);
VWVFLSa	6.601	0.436	15.13990826	20.561325	0.339789331	0.005	1	100	100	Very well sorted lower very fine sand
										Fabric (A);
WVFLSa	6.619	0.838	7.898568019	25.9007	0.339789331	0.005	1	100	100	Well sorted lower very fine sand
										Fabric (A);
MVFLSa	6.74	1.872	3.60042735	32.857875	0.339789331	0.005	1	100	100	Moderately sorted lower very fine sand
										Fabric (A);
PVFLSa	7.064	3.825	1.846797386	37.649725	0.339789331	0.005	1	100	100	Poorly sorted lower very fine sand
										Fabric (A);
VPVFLSa	8.434	15.957	0.528545466	44.263675	0.339789331	0.005	1	100	100	Very poorly sorted lower very fine sand
										Fabric (A);
EWUCSi	9.219	0.21	43.9	14.862125	0.339789331	0.005	1	100	100	Extremely well sorted upper coarse silt
										Fabric (A);
VWUCSi	9.217	0.608	15.15953947	23.79125	0.339789331	0.005	1	100	100	Very well sorted upper coarse silt
										Fabric (A);
WUCSi	9.242	1.17	7.899145299	28.9391	0.339789331	0.005	1	100	100	Well sorted upper coarse silt
										Fabric (A);
MUCSi	9.411	2.614	3.600229533	36.468675	0.339789331	0.005	1	100	100	Moderately sorted upper coarse silt
										Fabric (A);
PUCSi	9.863	5.341	1.846657929	41.4779	0.339789331	0.005	1	100	100	Poorly sorted upper coarse silt
										Fabric (A);
VPUCSi	11.776	22.2793	0.528562388	46.3904	0.339789331	0.005	1	100	100	Very poorly sorted upper coarse silt
										Fabric (B);
EWUCSa	0.582	0.0133	43.7593985	1.577775	0.339789331	10	10	100	10	Extremely well sorted upper coarse sand
										Fabric (B);
VWUCSa	0.582	0.038	15.31578947	2.194325	0.339789331	10	10	100	10	Very well sorted upper coarse sand
										Fabric (B);
WUCSa	0.583	0.074	7.878378378	3.0928	0.339789331	10	10	100	10	Well sorted upper coarse sand
										Fabric (B);
MUCSa	0.594	0.165	3.6	4.312125	0.339789331	10	10	100	10	Moderately sorted upper coarse sand
										Fabric (B);
PUCSa	0.622	0.337	1.845697329	5.9936	0.339789331	10	10	100	10	Poorly sorted upper coarse sand
										Fabric (B);
VPUCSa	0.743	1.406	0.528449502	8.583225	0.339789331	10	10	100	10	Very poorly sorted upper coarse sand
										Fabric (B);
EWLCSa	0.828	0.019	43.57894737	1.6414	0.339789331	10	10	100	10	Extremely well sorted lower coarse sand
										Fabric (B);
VWLCSa	0.828	0.055	15.05454545	2.516275	0.339789331	10	10	100	10	Very well sorted lower coarse sand
										Fabric (B);
WLCSa	0.83	0.105	7.904761905	3.159075	0.339789331	10	10	100	10	Well sorted lower coarse sand
										Fabric (B);
MLCSa	0.845	0.235	3.595744681	6.8107	0.339789331	10	10	100	10	Moderately sorted lower coarse sand
										Fabric (B);
PLCSa	0.886	0.48	1.845833333	7.586725	0.339789331	10	10	100	10	Poorly sorted lower coarse sand
										Fabric (B);
VPLCSa	1.058	2.001	0.528735632	9.763425	0.339789331	10	10	100	10	Very poorly sorted lower coarse sand

										Fabric (B);
EWMUSa	1.163	0.027	43.07407407	1.9241	0.339789331	10	10	100	10	Extremely well sorted upper medium sand Fabric (B);
VWMUSa	1.163	0.077	15.1038961	3.286125	0.339789331	10	10	100	10	Very well sorted upper medium sand Fabric (B);
WMUSa	1.166	0.148	7.878378378	4.2875	0.339789331	10	10	100	10	Well sorted upper medium sand Fabric (B);
MMUSa	1.188	0.33	3.6	6.2594	0.339789331	10	10	100	10	Moderately sorted upper medium sand Fabric (B);
PMUSa	1.245	0.674	1.847181009	9.6213	0.339789331	10	10	100	10	Poorly sorted upper medium sand Fabric (B);
VPMUSa	1.486	2.811	0.528637496	13.2056	0.339789331	10	10	100	10	Very poorly sorted upper medium sand Fabric (B);
EWMLSa	1.645	0.0375	43.86666667	2.173075	0.339789331	10	10	100	10	Extremely well sorted lower medium sand Fabric (B);
VWMLSa	1.645	0.1085	15.16129032	3.31155	0.339789331	10	10	100	10	Very well sorted lower medium sand Fabric (B);
WMLSa	1.649	0.209	7.889952153	6.7912	0.339789331	10	10	100	10	Well sorted lower medium sand Fabric (B);
MMLSa	1.679	0.467	3.595289079	8.599275	0.339789331	10	10	100	10	Moderately sorted lower medium sand Fabric (B);
PMLSa	1.76	0.953	1.84679958	10.9195	0.339789331	10	10	100	10	Poorly sorted lower medium sand Fabric (B);
VPMLSa	2.101	3.976	0.528420523	15.4326	0.339789331	10	10	100	10	Very poorly sorted lower medium sand Fabric (B);
EWFUSa	2.327	0.053	43.90566038	2.4742	0.339789331	10	10	100	10	Extremely well sorted upper fine sand Fabric (B);
VWFUSa	2.326	0.154	15.1038961	4.557525	0.339789331	10	10	100	10	Very well sorted upper fine sand Fabric (B);
WFUSa	2.332	0.295	7.905084746	6.7411	0.339789331	10	10	100	10	Well sorted upper fine sand Fabric (B);
MFUSa	2.375	0.66	3.598484848	10.141125	0.339789331	10	10	100	10	Moderately sorted upper fine sand Fabric (B);
PFUSa	2.489	1.348	1.846439169	14.33435	0.339789331	10	10	100	10	Poorly sorted upper fine sand Fabric (B);
VPFUSa	2.972	5.623	0.528543482	18.064675	0.339789331	10	10	100	10	Very poorly sorted upper fine sand Fabric (B);
EWFLSa	3.279	0.075	43.72	3.235375	0.339789331	10	10	100	10	Extremely well sorted lower fine sand Fabric (B);
VWFLSa	3.279	0.216	15.18055556	7.079775	0.339789331	10	10	100	10	Very well sorted lower fine sand Fabric (B);
WFLSa	3.287	0.416	7.901442308	8.597625	0.339789331	10	10	100	10	Well sorted lower fine sand Fabric (B);
MFLSa	3.347	0.93	3.598924731	13.511	0.339789331	10	10	100	10	Moderately sorted lower fine sand Fabric (B);
PFLSa	3.508	1.9	1.846315789	16.6605	0.339789331	10	10	100	10	Poorly sorted lower fine sand Fabric (B);
VPFLSa	4.189	7.925	0.528580442	23.8625	0.339789331	10	10	100	10	Very poorly sorted lower fine sand Fabric (B);
EWVFUSa	4.653	0.106	43.89622642	3.298275	0.339789331	10	10	100	10	Extremely well sorted upper very fine sand Fabric (B);
VWVFUSa	4.652	0.307	15.15309446	6.5675	0.339789331	10	10	100	10	Very well sorted upper very fine sand Fabric (B);
WVFUSa	4.665	0.5904	7.901422764	11.038875	0.339789331	10	10	100	10	Well sorted upper very fine sand Fabric (B);
MVFUSa	4.75	1.32	3.598484848	15.572925	0.339789331	10	10	100	10	Moderately sorted upper very fine sand Fabric (B);
PVFUSa	4.979	2.696	1.846810089	20.19695	0.339789331	10	10	100	10	Poorly sorted upper very fine sand Fabric (B);
VPVFUSa	5.944	11.246	0.528543482	27.417875	0.339789331	10	10	100	10	Very poorly sorted upper very fine sand Fabric (B);
EWVFLSa	6.6025	0.1504	43.89960106	4.51955	0.339789331	10	10	100	10	Extremely well sorted lower very fine sand Fabric (B);
VWVFLSa	6.601	0.436	15.13990826	9.70025	0.339789331	10	10	100	10	Very well sorted lower very fine sand Fabric (B);
WVFLSa	6.619	0.838	7.898568019	13.498775	0.339789331	10	10	100	10	Well sorted lower very fine sand Fabric (B);
MVFLSa	6.74	1.872	3.60042735	18.181025	0.339789331	10	10	100	10	Moderately sorted lower very fine sand

										Fabric (B);
PVFLSa	7.064	3.825	1.846797386	24.981725	0.339789331	10	10	100	10	Poorly sorted lower very fine sand
										Fabric (B);
VPVFLSa	8.434	15.957	0.528545466	31.823725	0.339789331	10	10	100	10	Very poorly sorted lower very fine sand
										Fabric (B);
EWUCSi	9.219	0.21	43.9	7.016175	0.339789331	10	10	100	10	Extremely well sorted upper coarse silt
										Fabric (B);
VWUCSi	9.217	0.608	15.15953947	11.253425	0.339789331	10	10	100	10	Very well sorted upper coarse silt
										Fabric (B);
WUCSi	9.242	1.17	7.899145299	15.515925	0.339789331	10	10	100	10	Well sorted upper coarse silt
										Fabric (B);
MUCSi	9.411	2.614	3.600229533	22.891425	0.339789331	10	10	100	10	Moderately sorted upper coarse silt
										Fabric (B);
PUCSi	9.863	5.341	1.846657929	28.270225	0.339789331	10	10	100	10	Poorly sorted upper coarse silt
										Fabric (B);
VPUCSi	11.776	22.2793	0.528562388	33.7752	0.339789331	10	10	100	10	Very poorly sorted upper coarse silt
										Fabric (C);
EWUCSa	0.582	0.0133	43.7593985	1.659375	0.339789331	100	100	100	1	Extremely well sorted upper coarse sand
										Fabric (C);
VWUCSa	0.582	0.038	15.31578947	1.6624	0.339789331	100	100	100	1	Very well sorted upper coarse sand
										Fabric (C);
WUCSa	0.583	0.074	7.878378378	1.711225	0.339789331	100	100	100	1	Well sorted upper coarse sand
										Fabric (C);
MUCSa	0.594	0.165	3.6	2.276275	0.339789331	100	100	100	1	Moderately sorted upper coarse sand
										Fabric (C);
PUCSa	0.622	0.337	1.845697329	2.9769	0.339789331	100	100	100	1	Poorly sorted upper coarse sand
										Fabric (C);
VPUCSa	0.743	1.406	0.528449502	4.635	0.339789331	100	100	100	1	Very poorly sorted upper coarse sand
										Fabric (C);
EWLCSa	0.828	0.019	43.57894737	1.659375	0.339789331	100	100	100	1	Extremely well sorted lower coarse sand
										Fabric (C);
VWLCSa	0.828	0.055	15.05454545	1.6919	0.339789331	100	100	100	1	Very well sorted lower coarse sand
										Fabric (C);
WLCSa	0.83	0.105	7.904761905	1.88225	0.339789331	100	100	100	1	Well sorted lower coarse sand
										Fabric (C);
MLCSa	0.845	0.235	3.595744681	2.803275	0.339789331	100	100	100	1	Moderately sorted lower coarse sand
										Fabric (C);
PLCSa	0.886	0.48	1.845833333	4.035725	0.339789331	100	100	100	1	Poorly sorted lower coarse sand
										Fabric (C);
VPLCSa	1.058	2.001	0.528735632	5.368275	0.339789331	100	100	100	1	Very poorly sorted lower coarse sand
										Fabric (C);
EWMUSa	1.163	0.027	43.07407407	1.659775	0.339789331	100	100	100	1	Extremely well sorted upper medium sand
										Fabric (C);
VWMUSa	1.163	0.077	15.1038961	1.755	0.339789331	100	100	100	1	Very well sorted upper medium sand
										Fabric (C);
WMUSa	1.166	0.148	7.878378378	2.13575	0.339789331	100	100	100	1	Well sorted upper medium sand
										Fabric (C);
MMUSa	1.188	0.33	3.6	3.3057	0.339789331	100	100	100	1	Moderately sorted upper medium sand
										Fabric (C);
PMUSa	1.245	0.674	1.847181009	5.87445	0.339789331	100	100	100	1	Poorly sorted upper medium sand
										Fabric (C);
VPMUSa	1.486	2.811	0.528637496	8.670025	0.339789331	100	100	100	1	Very poorly sorted upper medium sand
										Fabric (C);
EWMLSa	1.645	0.0375	43.86666667	1.66195	0.339789331	100	100	100	1	Extremely well sorted lower medium sand
										Fabric (C);
VWMLSa	1.645	0.1085	15.16129032	1.941675	0.339789331	100	100	100	1	Very well sorted lower medium sand
										Fabric (C);
WMLSa	1.649	0.209	7.889952153	2.850675	0.339789331	100	100	100	1	Well sorted lower medium sand
										Fabric (C);
MMLSa	1.679	0.467	3.595289079	5.0172	0.339789331	100	100	100	1	Moderately sorted lower medium sand
										Fabric (C);
PMLSa	1.76	0.953	1.84679958	5.924775	0.339789331	100	100	100	1	Poorly sorted lower medium sand
										Fabric (C);
VPMLSa	2.101	3.976	0.528420523	10.37715	0.339789331	100	100	100	1	Very poorly sorted lower medium sand
										Fabric (C);
EWFUSa	2.327	0.053	43.90566038	1.691	0.339789331	100	100	100	1	Extremely well sorted upper fine sand
										Fabric (C);
VWFUSa	2.326	0.154	15.1038961	2.22735	0.339789331	100	100	100	1	Very well sorted upper fine sand

										Fabric (C):
WFUSa	2.332	0.295	7.905084746	3.48795	0.339789331	100	100	100	1	Well sorted upper fine sand
										Fabric (C):
MFUSa	2.375	0.66	3.598484848	5.2799	0.339789331	100	100	100	1	Moderately sorted upper fine sand
										Fabric (C):
PFUSa	2.489	1.348	1.846439169	9.72225	0.339789331	100	100	100	1	Poorly sorted upper fine sand
										Fabric (C):
VPFUSa	2.972	5.623	0.528543482	10.4592	0.339789331	100	100	100	1	Very poorly sorted upper fine sand
										Fabric (C):
EWFLSa	3.279	0.075	43.72	1.75555	0.339789331	100	100	100	1	Extremely well sorted lower fine sand
										Fabric (C):
VWFLSa	3.279	0.216	15.18055556	2.933875	0.339789331	100	100	100	1	Very well sorted lower fine sand
										Fabric (C):
WFLSa	3.287	0.416	7.901442308	4.869825	0.339789331	100	100	100	1	Well sorted lower fine sand
										Fabric (C):
MFLSa	3.347	0.93	3.598924731	8.083725	0.339789331	100	100	100	1	Moderately sorted lower fine sand
										Fabric (C):
PFLSa	3.508	1.9	1.846315789	11.948125	0.339789331	100	100	100	1	Poorly sorted lower fine sand
										Fabric (C):
VPFLSa	4.189	7.925	0.528580442	12.748575	0.339789331	100	100	100	1	Very poorly sorted lower fine sand
										Fabric (C):
EWVFUSa	4.653	0.106	43.89622642	1.895975	0.339789331	100	100	100	1	Extremely well sorted upper very fine sand
										Fabric (C):
VWVFUSa	4.652	0.307	15.15309446	3.72535	0.339789331	100	100	100	1	Very well sorted upper very fine sand
										Fabric (C):
WVFUSa	4.665	0.5904	7.901422764	5.923825	0.339789331	100	100	100	1	Well sorted upper very fine sand
										Fabric (C):
MVFUSa	4.75	1.32	3.598484848	10.517375	0.339789331	100	100	100	1	Moderately sorted upper very fine sand
										Fabric (C):
PVFUSa	4.979	2.696	1.846810089	12.0156	0.339789331	100	100	100	1	Poorly sorted upper very fine sand
										Fabric (B):
VPVFUSa	5.944	11.246	0.528543482	12.903925	0.339789331	100	100	100	1	Very poorly sorted upper very fine sand
										Fabric (C):
EWVFLSa	6.6025	0.1504	43.89960106	2.185075	0.339789331	100	100	100	1	Extremely well sorted lower very fine sand
										Fabric (C):
VWVFLSa	6.601	0.436	15.13990826	5.142675	0.339789331	100	100	100	1	Very well sorted lower very fine sand
										Fabric (C):
WVFLSa	6.619	0.838	7.898568019	8.080775	0.339789331	100	100	100	1	Well sorted lower very fine sand
										Fabric (C):
MVFLSa	6.74	1.872	3.60042735	11.34865	0.339789331	100	100	100	1	Moderately sorted lower very fine sand
										Fabric (C):
PVFLSa	7.064	3.825	1.846797386	13.9784	0.339789331	100	100	100	1	Poorly sorted lower very fine sand
										Fabric (C):
VPVFLSa	8.434	15.957	0.528545466	20.367575	0.339789331	100	100	100	1	Very poorly sorted lower very fine sand
										Fabric (C):
EWUCSi	9.219	0.21	43.9	2.739075	0.339789331	100	100	100	1	Extremely well sorted upper coarse silt
										Fabric (C):
VWUCSi	9.217	0.608	15.15953947	6.2112	0.339789331	100	100	100	1	Very well sorted upper coarse silt
										Fabric (C):
WUCSi	9.242	1.17	7.899145299	11.084425	0.339789331	100	100	100	1	Well sorted upper coarse silt
										Fabric (C):
MUCSi	9.411	2.614	3.600229533	13.04665	0.339789331	100	100	100	1	Moderately sorted upper coarse silt
										Fabric (C):
PUCSi	9.863	5.341	1.846657929	13.872725	0.339789331	100	100	100	1	Poorly sorted upper coarse silt
										Fabric (C):
VPUCSi	11.776	22.2793	0.528562388	23.139175	0.339789331	100	100	100	1	Very poorly sorted upper coarse silt
										Fabric (C):
	7.406	0.015	493.7333333	1.59185	0.339789331	100	100	100	1	With <Pth> measured from the peel # 1 and varying σPth
										Fabric (C):
	7.4121	0.0659	112.4749621	1.824525	0.339789331	100	100	100	1	With <Pth> measured from the peel # 1 and varying σPth
										Fabric (C):
	7.507	0.1737	43.21819229	2.527925	0.339789331	100	100	100	1	With <Pth> measured from the peel # 1 and varying σPth
										Fabric (C):
	7.4325	0.2497	29.76571886	3.23895	0.339789331	100	100	100	1	With <Pth> measured from the peel # 1 and varying σPth
										Fabric (C):
	7.4496	0.3603	20.67610325	4.125875	0.339789331	100	100	100	1	With <Pth> measured from the peel # 1 and varying σPth
										Fabric (C):
	7.4938	0.4937	15.17885355	6.2062	0.339789331	100	100	100	1	With <Pth> measured from the peel # 1 and varying σPth

									Fabric (C);
	7.578	0.7001	10.82416798	7.767175	0.339789331	100	100	100	1 With <Pth> measured from the peel # 1 and varying σPth Fabric (C);
	7.96134	1.3867	5.741212952	11.844625	0.339789331	100	100	100	1 With <Pth> measured from the peel # 1 and varying σPth Fabric (B);
	7.4062	0.01303	568.3960092	1.6136	0.339789331	10	10	100	10 With <Pth> measured from the peel # 1 and varying σPth Fabric (B);
	7.41203	0.0559	132.5944544	2.34045	0.339789331	10	10	100	10 With <Pth> measured from the peel # 1 and varying σPth Fabric (B);
	7.5072	0.1454	51.63136176	4.645325	0.339789331	10	10	100	10 With <Pth> measured from the peel # 1 and varying σPth Fabric (B);
	7.4319	0.2184	34.02884615	6.414225	0.339789331	10	10	100	10 With <Pth> measured from the peel # 1 and varying σPth Fabric (B);
	7.4484	0.3154	23.61572606	9.37305	0.339789331	10	10	100	10 With <Pth> measured from the peel # 1 and varying σPth Fabric (B);
	7.4863	0.4155	18.01756919	9.605225	0.339789331	10	10	100	10 With <Pth> measured from the peel # 1 and varying σPth Fabric (B);
	7.5767	0.6028	12.56917717	12.058575	0.339789331	10	10	100	10 With <Pth> measured from the peel # 1 and varying σPth Fabric (B);
	7.9562	1.1778	6.755136696	15.7365	0.339789331	10	10	100	10 With <Pth> measured from the peel # 1 and varying σPth Fabric (A);
	7.4082	0.0128	578.765625	3.482925	0.339789331	0.005	1	100	100 With <Pth> measured from the peel # 1 and varying σPth Fabric (A);
	7.4206	0.0552	134.4311594	7.0824	0.339789331	0.005	1	100	100 With <Pth> measured from the peel # 1 and varying σPth Fabric (A);
	7.5293	0.1439	52.32314107	10.4993	0.339789331	0.005	1	100	100 With <Pth> measured from the peel # 1 and varying σPth Fabric (A);
	7.4652	0.2159	34.57711904	18.0132	0.339789331	0.005	1	100	100 With <Pth> measured from the peel # 1 and varying σPth Fabric (A);
	7.4966	0.312	24.0275641	19.9008	0.339789331	0.005	1	100	100 With <Pth> measured from the peel # 1 and varying σPth Fabric (A);
	7.5493	0.4175	18.08215569	22.5952	0.339789331	0.005	1	100	100 With <Pth> measured from the peel # 1 and varying σPth Fabric (A);
	7.6686	0.5955	12.87758186	26.264125	0.339789331	0.005	1	100	100 With <Pth> measured from the peel # 1 and varying σPth Fabric (A);
	8.1351	1.17013	6.952304445	26.485875	0.339789331	0.005	1	100	100 With <Pth> measured from the peel # 1 and varying σPth Fabric (C);
	7.603	0.3572	21.2849944	3.846325	0.291247998	100	100	100	1 With <Pth> measured from the peel # 1 and varying Δp Fabric (C);
	7.603	0.3572	21.2849944	2.53455	0.169894665	100	100	100	1 With <Pth> measured from the peel # 1 and varying Δp Fabric (C);
	7.603	0.3572	21.2849944	2.15605	0.127420999	100	100	100	1 With <Pth> measured from the peel # 1 and varying Δp Fabric (C);
	7.603	0.3572	21.2849944	1.877025	0.107301894	100	100	100	1 With <Pth> measured from the peel # 1 and varying Δp Fabric (B);
	7.6025	0.30798	24.68504448	6.9366	0.291247998	10	10	100	10 With <Pth> measured from the peel # 1 and varying Δp Fabric (B);
	7.6025	0.30798	24.68504448	5.91165	0.169894665	10	10	100	10 With <Pth> measured from the peel # 1 and varying Δp Fabric (B);
	7.6025	0.30798	24.68504448	4.336375	0.127420999	10	10	100	10 With <Pth> measured from the peel # 1 and varying Δp Fabric (B);
	7.6025	0.30798	24.68504448	3.5266	0.107301894	10	10	100	10 With <Pth> measured from the peel # 1 and varying Δp Fabric (A);
	7.6496	0.3045	25.12183908	18.455625	0.291247998	0.005	1	100	100 With <Pth> measured from the peel # 1 and varying Δp Fabric (A);
	7.6496	0.3045	25.12183908	14.13485	0.169894665	0.005	1	100	100 With <Pth> measured from the peel # 1 and varying Δp Fabric (A);
	7.6496	0.3045	25.12183908	12.02315	0.127420999	0.005	1	100	100 With <Pth> measured from the peel # 1 and varying Δp Fabric (A);
	7.6496	0.3045	25.12183908	10.38625	0.107301894	0.005	1	100	100 With <Pth> measured from the peel # 1 and varying Δp
Peel 1	7.47051	0.350287	21.32682629	5.400825	0.339789331				2 Peel # 1 fabric; (0.4 m ◈ 0.4 m model section)
Peel 2	7.47051	0.350287	21.32682629		0.339789331				4.3 Peel # 2 fabric; (0.4 m ◈ 0.4 m model section)

Table A-1: Data table for Figures 5-10 and 5-11

Effect of threshold pressure range plot for different depositional fabrics: data points

Line source of CO_2 is allowed to migrate through the model domain with periodic lateral flow boundaries for all cases. The percentage of the model domain invaded by CO_2 is shown for each simulation case. The depositional fabrics used are: peel # 1 working model, geostatistical model fabrics (A), (B) and (C).

Table A-2 below gives the data used in the thesis for analysis (Figures 5-3 to 5-9).

<Pth>, kPa	σPth, kPa	<Pth>/σPth	% model invaded by CO2 at percolation	1/(del rho g), m/kPa	Vertical correlation length/dz (in terms of # of cells)	Revised vertical correlation length/dz	Horizontal correlation length/dz	Horizontal correlation length/revised vertical correlation length	Comments (0.4 m × 0.4 m models)
7.4004	0.02	474.3846154	1.752125	0.339789331				2	Peel # 1 fabric
7.388	0.07	112.9663609	1.80205	0.339789331				2	
7.444	0.17	43.12862109	3.1976	0.339789331				2	
7.3402	0.25	29.87464387	3.7981	0.339789331				2	
7.316	0.35	20.68419565	4.788725	0.339789331				2	
7.3163	0.48	15.27092465	5.12225	0.339789331				2	
7.3206	0.69	10.64195377	10.615675	0.339789331				2	
7.45475	1.37	5.440946778	13.87095	0.339789331				2	
7.406	0.02	493.7333333	1.59185	0.339789331	100	100	100	1	Fabric C)
7.4121	0.07	112.4749621	1.824525	0.339789331	100	100	100	1	
7.507	0.17	43.21819229	2.527925	0.339789331	100	100	100	1	
7.4325	0.25	29.76571886	3.23895	0.339789331	100	100	100	1	
7.4496	0.36	20.67610325	4.125875	0.339789331	100	100	100	1	
7.4938	0.49	15.17885355	6.2062	0.339789331	100	100	100	1	
7.578	0.70	10.82416798	7.767175	0.339789331	100	100	100	1	
7.96134	1.39	5.741212952	11.844625	0.339789331	100	100	100	1	
7.4062	0.01	568.3960092	1.6136	0.339789331	10	10	100	10	Fabric B)
7.41203	0.06	132.5944544	2.34045	0.339789331	10	10	100	10	
7.5072	0.15	51.63136176	4.645325	0.339789331	10	10	100	10	
7.4319	0.22	34.02884615	6.414225	0.339789331	10	10	100	10	
7.4484	0.32	23.61572606	9.37305	0.339789331	10	10	100	10	
7.4863	0.42	18.01756919	9.605225	0.339789331	10	10	100	10	
7.5767	0.60	12.56917717	12.058575	0.339789331	10	10	100	10	
7.9562	1.18	6.755136696	15.7365	0.339789331	10	10	100	10	
7.4082	0.01	578.765625	3.482925	0.339789331	0.005	1	100	100	Fabric A)
7.4206	0.06	134.4311594	7.0824	0.339789331	0.005	1	100	100	
7.5293	0.14	52.32314107	10.4993	0.339789331	0.005	1	100	100	
7.4652	0.22	34.57711904	18.0132	0.339789331	0.005	1	100	100	
7.4966	0.31	24.0275641	19.9008	0.339789331	0.005	1	100	100	
7.5493	0.42	18.08215569	22.5952	0.339789331	0.005	1	100	100	
7.6686	0.60	12.87758186	26.264125	0.339789331	0.005	1	100	100	
8.1351	1.17	6.952304445	26.485875	0.339789331	0.005	1	100	100	

Table A-2: Data table for sensitivity analysis of threshold pressure ranges on different model fabrics

BIBILIOGRAPHY

Allen, J.R.L., 1971, *A theoretical and experimental study of climbing-ripple cross-lamination, with a field application to the Uppsala Esker*, Geografiska Annaler, Series A, Physical Geography, Vol. 53, No. 3/4, pp. 157-187.

Auradou H; Maloy, Knut Jorgen; Schmittbuhl, Jean; Hansen A; Bideau D., 1999, *Competition between correlated buoyancy and uncorrelatated capillary effects during drainage*, Physical Review E, 60 (6), 7224-34.

Bachu, S., Bonijoly, D., Bradshaw, J., Burruss, R., Holloway, S., Christensen, N.P., Mathiasen O.M., 2007, *CO2 storage capacity estimation: Methodology and gaps*, Int. J. Greenhouse Gas Control, 1(4): 430-443.

Berg, R.R., 1975, *Capillary pressures in stratigraphic traps*, AAPG Bull., 59(6): 939-956.

Bernard, H.A., and Major, C.F., Jr., 1963, *Recent meander belt deposits of the Brazos River: An alluvial "sand" model*, AAPG Bull., 47(2): 350.

Bernard, H.A., Major, C.F., Jr., Parrott, B.S., Le Blanc, R.J., Sr., 1970, *Recent sediments of southeast Texas: A field guide to the Brazos alluvial and deltaic plains and the Galveston barrier island complex*, The University of Texas at Austin, Bureau of Economic Geology, Guidebook 11.

Boden, T.A., Marland, G., Andres, R.J., 2010, *Global, Regional, and National Fossil-Fuel CO_2 Emissions*, Carbon Dioxide Information Analysis Center, Oak Ridge National Laboratory, U.S. Department of Energy, Oak Ridge, Tenn., U.S.A. doi 10.3334/CDIAC/00001_V2010.

Boggs, S Jr. 1994, *Principles of sedimentology and stratigraphy*: Prentice Hall.

Bryant, S. L, Cade, C., Mellor, D., 1993, *Permeability prediction from geologic models*, AAPG Bull., 77(8): 1338-1350.

Bryant, S L., Lakshminarasimhan, S, Pope, G. A., 2008, *Buoyancy-dominated multiphase flow and its effect on geological sequestration of CO_2*. J. 13 (4), 4477-454 SPE-99938-PA.

Carruthers, D. J. F., 1998, *Transport modelling of secondary oil migration using gradient-driven invasion percolation techniques*, Ph.D. Dissertation, Department of petroleum Engineering, Heriot-Watt University, Edinburgh, Scotland UK.

Cavanaugh, A and Ringrose, 2011, *Simulation of CO_2 distribution at the In Salah storage site using high-resolution field-scale models*, Energy Proc, DOI:10.1016/j.egypro.2011.02.306.

Celia, M A and Nordbotten J M, 2009, *Practical modeling approaches for geological storage of carbon* dioxide, Ground Water, Vol. 47, No.5 pg 627-638.

Chadwick, R. A., Williams, G., Delepine, N., Clochard, V., Labat, K., Sturton, S., Buddensiek, M. L., Dillen, M., Nickel, M., Lima, A. L., Arts, R., Neele, F., Rossi, G., 2010, *Quantitative analysis of time-lapse seismic monitoring data at the Sleipner CO2 storage operation*, The Leading Edge, 29, 170-177.

Chandler, R., Koplik, J., Lerman, K., Willemsen, J., 1982, *capillary displacement and percolaton in pporouss mediai*, J. fluid Mech. 119, 249-267.

Cottin, C; Bodiguel, H; Colin, A, 2010, *Drainage in two-dimensional porous media: From capillary fingering to viscous flow*, Physical Review E, 80, 046315, DOI:10.1103/PhyRevE.82.046315.

England, W.A., Mackenzie, A.S., Mann, D.M., Quigley, T.M., 1987, *The movement and entrapment of petroleum fluids in the subsurface*, J. Geol. Soc. London special publication, 144: 327-347.

Ferer, M., Ji, C., Bromhal, G. S., Cook, J. , Ahmadi, G., Smith, D. H., 2004, *Crossover from capillary fingering to viscous fingering for immiscible unstable flow: Experiment ad modeling*, Phys. Rev. E 70, 016303, 2004.

Ferer, M., Anna, S. L, Tortora, P., Kadambi, J. R, Olive, M., Broomhal, G. S., Smith, D. H, 2010, *Two-phase flow in porous media: predicting its dependence on capillary number and viscosity ratio*, Transp. Porous Med, DOI 10.1007/s11242-010-9619-3.

Ferer, M., Bromhal, G S., Smith, D H., 2005, *Two-phase flow in porous media: crossover from capillary fingering to compact invasion for drainage*, Physical review E 71, 026303, doi: 10.1103/PhysRevE.71.026303.

Folk, R.L. and Ward, W.C., 1957, *Brazos River bar, a study in the significance of grain size parameters*, J. Sediment. Petrol.**,** 27: 3-27.

Glass, R. J., Conrad, S. H., Peplinski, W, November 2000, *Gravity-destabilized nonwetting phase invasion in macroheterogeneous porous media: Experimental observations of invasion dynamics and scale analysis*, Water Resources Research, 36(11), Pages 3121-3137.

Hermanrud, C, Teige, G M G, Iding, M, Eiken, O. L, Ostmo, S., 2010, *Differences between flow of injected CO_2 and hydrocarbon migration*, Petroleum Geology Conference series 7, 1183-1188, DOI:10.1144/0071183.

Hesse, M. A. and Woods, A. W., 2010, Buoyant dispersal of CO_2 during geological storage, Geophys. Res. Lett., 37, L01403, doi:10.1029/2009GL041128.

Hirsch, L. M. and Thompson, A. H., 1995, Minimum saturations and buoyancy in secondary migration, AAPG Bulletin, v. 79, no. 5, p. 696–710.

Hou, P., Zhou, B., Luo, X. R., 2005, *Experimental studies on pathway patterns of secondary oil migration*, Science in China Series D, v. 49, no. 2, p. 469–473.

Ide, S.T, Jessen, K., Orr Jr., Franklin M., 2007, *Storage of CO_2 in saline aquifers: Effects of gravity, viscous and capillary forces in amount and timing of trapping*, Int. Journal of Greenhouse Gas Control, 481-491; DOI:10.1016/S1750-5836(07)00091-6.

Chen, J.-D. and Wilkinson, D., 1985, *Pore-scale viscous fingering in porous media*, Phys. Rev. Lett. 55, 1892- 1985.

Kidwell, S.M., Moore, J.A., Moore, J.R., 1985, *Inexpensive field technique for polyester resin peels of structures in unconsolidated sediments*, Marine Geol., 64: 351-359.11.

Krevor, S. C.M., Pini, R., Li, B., Benson, S M., 2011, *Capillary heterogeneity trapping of CO_2 in a sandstone rock at reservoir conditions*, Geophysical Research Letters, 38, L15401; DOI:10.1029/2011GL048239.

Kumar, A., Noh, M., Pope, G., Sepehrnoori, K., Bryant, S.L., Lake, L., 2005, *Reservoir simulation of CO_2 storage in deep saline aquifer*, SPEJ 10 (3): 336-348, SPE 89343-PA.

Kumar, N., 2008, *CO_2 sequestration: Understanding the plume dynamics and estimating the risk*. Master's Thesis, Department of Petroleum Engineering, The University of Texas at Austin.

Law, J., 1944, *A statistical approach to the interstitial heterogeneity of sand reservoirs*, American Institute of Mining, Metallurgical, and Petroleum Engineers, Technical Publication 7 (3): 202- 221.

Lenormand, R., Touboul, E., Zarcone, C., 1988, *Numerical models and experiments on immiscible displacements in porous media*, J. Fluid Mech., vol 189, pp. 165-187, doi:10.1017/s0022112088000953.

Lovoll, G., Meheust, Yves, Maloy, K. J., Ker, E, Schmittbuhl, J, 2005, *Competition of gravity, capillary and viscous forces during drainage in a two-dimensional porous medium, a pore-scale study*, Elsevier Energy, doi:10.1016/j.energy.2004.03.100.

Lovoll, G., Jankov, M., Maloy, K. J., Toussaint, R., Schmittbuhl, J, Schafer, G., Meheust, Y., 2010, *Influence of viscous fingering on dynamic saturation-pressure curves in porous media*, Transp. Porous Med doi:10.1007/s11242-010-9622-8.

Luo,X. R, 2011, *Simulation and characterization of pathway heterogeneity of secondary hydrocarbon migration*, AAPG doi: 10.1036/11191010027.

Luo, X.R., Yan, J.Z, Zhou, B., Hou, P, Wang, W., Vasseur, G., 2008, *Quantitative estimates of oil losses during migration, part II: measurement of the residual oil saturation in migration pathways*, Journal of Petroleum Geology, 31(2), 179-190.

Luo, X.R., Zhou, B., Zhao, S.X., Zhang, F.Q, Vasseur, G., 2007, *Quantitative estimates of oil losses during migration, part I: the saturation of pathways in carrier beds*, Journal of Petroleum Geology, 30(4), 375-387.

McMullen, R.M. and Allen, J.R.L., 1964, *Preservation of sedimentary structures in wet unconsolidated sands using polyester resins*, Marine Geol., 1: 88-97.

Meckel, T.A., 2012, *Digital modeling of a sedimentary-relief peel: implications for clastic facies characterization and fluid migration simulation*, Paper in review.

Noh, M., Lake, L., Bryant, S. L., Araque-Martinez, A., 2007, *Implications of coupling fractional flow and geochemistry for CO_2 injection in aquifers*, SPEREE 10 (4): 406-411, SPE 89341-PA.

Ozah, R., Lakshminarasimhan, S., Pope, G., Sepehrnoori, K., Bryant, S. L., 2005, *Numerical simulation of storage of pure CO_2 and CO_2-H_2S gas mixtures in deep*

saline aquifers, Paper SPE 97255 presented at 2006 SPE Annual Technical Conference and Exhibition, Dallas, Texas, 9-12 October.

Ricciardi, K.L., 2005, *Comparison of the lognormal and beta distribution functions to describe the uncertainty in permeability*, J. Hydrology, 313: 248-256.

Ringrose, P. S.; Corbett, P. W. M., 1994, *Controls on two-phase fluid flow in heterogeneous sandstones. Geofluids: Origin, Migration and Evolution of fluids in Sedimentary Basins*, Geological Society Special Publication, 78, 141-150.

Saadatpoor, E., Bryant, S. L., Sepehrnoori, K., 2009, *New trapping mechanism in carbon sequestration*, Trans. Porous Media, 82, 3-17.

Saadatpoor, E., Bryant, S. L., Sepehrnoori, K., 2010, *CO_2 leakage from heterogeneous storage formations*, Paper 135629 presented at the SPE Annual Technical Conference and Exhibition held in Florence, Italy, 19-22 September 2010.

Salomao, M.C., 1997, *Analysis of flow in spatially correlated systems by applying the percolation theory*, Paper 39039 presented at the fifth Latin American and Caribbean Petroleum Engineering Conference and Exhibition held in Rio de Janeiro, Brazil, 30 August - 3 September 1997.

Singh, V.; Cavanaugh, A, Hansen, H., Nazarian, B., Iding, M., Ringrose, P., 2010, *Reservoir modeling of CO_2 plume behavior calibrated against monitoring data from Sleipner, Norway*, Paper 134891 presented at the SPE Annual Technical Conference and Exhibition held in Florence, Italy, 19-22 September 2010.

Tokunaga, T., Mogi, K., Matsubara, O., 2000, *Buoyancy and interfacial force effects on two-phase displacement patterns: an experimental study*, AAPG Bulletin, 84: 65-74.

van der Meer, L. G. H., 1995, *The CO_2 storage efficiency of aquifers*, Energy Conv. Mgmt., 36: 513-518.

Wilkinson, D., 1986, *Percolation effects in immiscible displacement*, Physical Review A, v. 34, p. 1380–1391.

Wilkinson, D., and Willemsen, J. F., 1983, *Invasion percolation: A new form of percolation theory*, Journal of Physics, v. A16, p. 3365–3376.

Yan, J., Lou, .R., Wang, W., Toussaint, R., Schmittbuhl, J., Vasseur, Chen, F., Yu, A., Zhang, L, 2012, *An experimental study of secondary oil migration in a three-dimensional tilted porous medium*, AAPG Bulletin, V. 96, No. 5, pp: 773-788, doi: 10.1306/09091110140.

Zhang, C, Oostrom, M, Wietsma, T. W., Grate, J. W., Warner, M. G., 2011, *Influence of viscous and capillary forces on immiscible fluid displacement: pore-scale experimental study in a water-wet micromodel demonstrating viscous and capillary fingering*, Energy Fuels, 25, 3493-3505 dx.doi.org/10.1021/ef101732k.